Microscopy of quantum many-body systems out of equilibrium

Sebastian Hild

München 2016

Microscopy of quantum many-body systems out of equilibrium

Dissertation
an der Fakultät für Physik
der Ludwig–Maximilians–Universität
München

vorgelegt von
SEBASTIAN HILD
aus Remscheid

München, Juli 2016

Erstgutachter: Prof. Dr. Immanuel Bloch
Zweitgutachter: Prof. Dr. Michael Knap
Tag der mündlichen Prüfung: 16.09.2016

Zusammenfassung

Quantensimulatoren können die Grenzen von analytischen und numerischen Methoden überwinden und detaillierte Informationen über stark korrelierte Vielteilchensysteme liefern. Für die experimentelle Erforschung komplexer Problemstellungen bieten Quantengase vielfältige Möglichkeiten und profitieren von der herausragenden Isolation von externen Störungen. Diese Promotionsarbeit befasst sich mit dem experimentellen Studium von Quantensystemen, die kontrolliert aus dem Gleichgewicht gebracht werden. Mit Einzelplatz aufgelöster Abbildung von bosonischen Rubidium Atomen in optischen Gittern wird die zeitliche Entwicklung festgehalten.

Quantenmagnetismus ist der erste behandelte Schwerpunkt in dieser Arbeit. Zuerst zeigen wir, dass im Regime von starker Wechselwirkung,in welchem sich ein Mott Isolator bildet, ein zwei komponentiges Gas exzellent das Heisenberg Model simuliert. Hierzu vermessen wir die kohärente Ausbreitung eines Magnons mit der spinselektiven Abbildung nach einer lokalen Anregung eines einzelnen Spins. Spinprojektionen auf die z-Achse und den Äquator der Bloch-Kugel belegen die Entstehung und Propagation von verschränkten Zuständen. Detaillierte Informationen werden in diesem Experiment durch eine neu entwickelte Abbildung gewonnen, welche an Stern-Gerlach Messungen angelehnt ist. Bei der Anregung zweier benachbarter Spins wird des Weiteren die Entstehung gebundener Zustände beobachtet und deren Ausbreitungsgeschwindigkeit sowie Zerfallszeit charakterisiert. In weiterführenden Messungen erzeugen wir hochangeregte Spiralzustände, die in einen homogenen Gleichgewichtszustand zerfallen und keine kohärente Zeitentwicklung aufweisen. Die Geschwindigkeit der beobachteten Zerfälle ist abhängig von der Windungsstärke und weist in eindimensionalen Systemen auf ein diffusives Verhalten hin. Im Gegensatz dazu deuten die Ergebnisse in zweidimensionalen Systemen auf ein sub-diffusive Propagation hin.

Der zweite Schwerpunkt dieser Arbeit behandelt die Thermalisierung von hoch angeregten Systemen. Wir ermitteln wie stark eine zusätzlich eingestrahlte computergenerierte zufällige Potentiallandschaft sein muss, um zu einer Lokalisierung der Atome zu führen. Von diesen entstehenden lokalisierten Vielteilchenzustände wird die Zerfallslänge der Dichteverteilung bestimmt, welche am Phasenübergang eine Divergenz zeigt.

Die in dieser Arbeit beschriebenen Experimente demonstrieren unterschiedliche Realisierungen von Quantensimulationen. Viele weitere Effekte im Bereich der Quantenmechanik können mit der hier dargelegten Technik untersucht werden. Weitere Messungen profitieren insbesondere von der nachgewiesenen präzisen Anfangszustandspräparation, basierend auf der Kontrolle jedes einzelnen Atomes in wechselwirkenden Vielteilchensystemen, und der ortsaufgelösten Erfassung von einzelnen Atomen. Dieses wird in Zukunft einen wesentlichen Beitrag zur Informationsgewinnung über komplexe verschränkte Systeme liefern können.

Abstract

Quantum simulators can overcome the limits of analytical and numerical methods and deliver detailed information about strongly correlated many-body systems. For the experimental exploration of complex problems, quantum gases offer versatile possibilities and profit from the outstanding isolation from external disturbances. This doctoral thesis deals with the experimental study of quantum systems, which are controllably moved out of equilibrium. The temporal evolution is recorded with single-site resolved imaging of bosonic Rubidium atoms in optical lattices.

Quantum magnetism is the first examined main topic of this thesis. At first, we reveal that a two component gas is well suited to simulate the Heisenberg model in the regime of strong interaction and under the formation of a Mott insulating state. Therefore, we survey, after a local excitation of a single spin, the coherent expansion of a magnon with spin selective imaging. Utilizing spin projections on the z-axis and the equator of the Bloch sphere, the creation and propagation of entangled states is observed. In this experiment, detailed information are extracted with the newly developed Stern-Gerlach like imaging. Furthermore, the emergence and expansion velocity of bound states after the excitation of two neighboring spins is surveyed. The experiments are extended to highly excited spiral states, which decay to homogeneous equilibrium states and do not indicate coherent evolution. The determined decay rate depends on the winding strength and manifests a diffusive behavior in one dimensional systems. In contrast, measurements in two dimensional systems point towards a sub-diffusive evolution.

The second main focus of this theses is the thermalization of highly excited states. We investigate how strong an additional computer generated random potential needs to be in order to lead to localization of the atoms. The decay length of the corresponding density distribution of the arising many-body localized states is quantified, which diverges at the phase transition.

The experiments characterized in this thesis demonstrate different realizations of quantum simulation. Several further effects in the field of quantum mechanics can be studied with the here demonstrated techniques. Further research will in particular benefit from the precise initial state manipulation, based on the control of every single atom within the many-body interacting system, and the spin selective spatial resolved detection of single atoms. In the future, this will yield a substantial contribution to the acquisition of information on complex entangled systems.

Contents

1 Introduction

The recently developed outstanding capabilities to control and manipulate well isolated ultracold quantum gases put these systems in the unique position to simulate and verify a variety of aspects of quantum mechanics [1–3]. Following the original idea of quantum simulators by Richard Feynman [4], ultracold quantum gases produce very clean systems. Simulations of many-body systems can explore new parameter regimes of such systems or even reach completely new many-body settings. Nowadays, valuable insights to several different models, especially for condensed matter systems, are obtained from observables only accessible with quantum gas experiments.

Simulations on classical computers struggle with calculating properties of large interacting many-body quantum systems. Computational limits are exceeded already by current ultracold quantum gas experiments. In contrast to solid state physics, the Hamiltonians describing atomic many-body systems are typically well known and the systems' parameters are precisely controlled. With these parameters, the system can be steered to the regime of competing interaction and kinetic energy. In this regime, the ground states are particularly difficult to characterize. Important examples are the Bardeen-Cooper-Schrieffer superfluidity to Bose-Einstein condensate crossover and Mott-insulator to Bose-Einstein condensate quantum phase transition.

Non-equilibrium properties of quantum systems are even harder than the exact prediction of ground states. Local or global quenches can lead to fast build up of entanglement which quickly limits simulations on current computers [5]. Therefore toy models of actual quantum systems are one approach to determine properties otherwise out of reach.

In this thesis, we focus on the dynamics of bosonic atoms in optical lattices and the mapping to the Heisenberg spin model. Heisenberg quantum magnets are examples of strongly-correlated materials, where the pure one-dimensional model is even exactly solvable by the Bethe ansatz [6]. However, with additional defects and in higher dimensions the complexity is drastically increased, limiting exact simulations to small systems. This is an ideal testbed for quantum simulation, because in certain regions the results can be compared to known predictions and further measurements can go beyond fully theoretically solvable models.

The realization of Bose-Einstein condensates, where a macroscopic amount of atoms occupies the ground state, marks a significant milestone for the field of ultracold quantum gases [7, 8]. Remarkable and versatile control of the underlying Hamiltonian of quantum gases was obtained by the addition of optical lattices. This permits to control the kinetic energy of the atoms and allows the observation of the superfluid to Mott insulator quantum phase transition in the Bose-Hubbard model [9]. Mott insulators are an outstanding initial state for quantum simulations of spin systems, because they exhibit a uniform occupation where the atom distribution is well known and is comparable to the initialization of the registers for classical computations. With single atom and single site resolved imaging of an interacting quantum many-body system within an optical lattice, detailed local information about quantum systems is available. This technique was realized in two groups and directly led to observations of the sub-Poissonian on-site atom number fluctuations of Mott Insulator states [10–12]. Moreover, the images allow to extract the spatial correlations of the many-body state which were utilized to locally resolve particle hole pair correlations [13] and to determine the propagation velocity of excitations [14]. The local control of the initial state, an essential requirement for quantum simulators, was demonstrated in the experiments tracking the movement of single atoms [15]. Meanwhile also artificial antiferromagnetic interactions were generated by tilting the lattice [16], strong correlation in a quantum walk of interacting atoms were detected [17] and algorithmic cooling was utilized to reduce the temperature of a quantum gas loaded into a lattice [18]. Furthermore, a method to resolve the spin state and atom number within a single image was implemented [19]. During the process of this thesis, this key technology of single site resolution was demonstrated for bosonic Ytterbium atoms [20, 21] and in-situ imaging was achieved for degenerate Fermi gases [22–26] and first experiments with strongly correlated fermions have been reported [27–30].

A major focus of this thesis is the study of the Heisenberg model, which is of huge interest in the framework of quantum magnetism and was studied in great detail as a key model exploring the quantum spin models emerging frequently in solid state physics [31]. Former experiments have already revealed the controlled effective spin interaction in a double well [32]. Also Ising like interaction of ensembles of up to a dozen spins has been performed with ion systems [33].

Ultracold atoms and in particular the single-site manipulation and detection of one and two dimensional systems permits to expand measurements to single spins out of reach in condensed matter systems. In a series of experiments, we study the quantum evolution of well isolated pseudo spin-1/2 systems realized with a two-component Bose gas in an optical lattice. It was

verified that the Heisenberg model describes the system in the regime where interactions are significantly stronger than tunneling rates. With unrevealed state preparation fidelity down to the single atom level, local excitations are created and their dynamical properties are inferred from extracted correlations and density distributions. Coherent propagation of the single spin excitations is observed even after several spin exchange times and an outward propagating entanglement wave is detected with an in-situ spin resolving imaging method. Furthermore we demonstrate the formation and movement of bound states after exciting two adjacent spins. In contrast to the coherent ballistic evolution following local quenches, global excitations to high energies result in diffusive dynamics.

A second important question investigated during this thesis is the long time evolution of an interacting many-body system. Quantum mechanics predicts a coherent evolution of the system, described by a unitary evolution, which preserves the total information in the system. This raises the question if these systems still thermalize without connection to an external bath [34]. Theoretical concepts, like eigenstate thermalization hypothesis, explain thermalization for most closed quantum systems [5]. Experiments reproduced the predicted thermalization [35–37] and also revealed that thermalization is not guaranteed for integrable systems [38]. A general class of non-ergodic systems which thus do not thermalize are many-body-localized systems [39]. This special behavior is triggered by disorder and the many-body-localized phase is an extension of the perfectly isolating Anderson localized systems to interacting systems [40]. First experiments on First, Anderson localization has been studied with ultracold gases investigating the expansion of non-interacting Bose-Einstein condensates [41, 42]. The topic of localization in interacting systems has been recently tackled in a series of experiments with fermions in 1D [43, 44] and close to the ground state [45–50]. The previous experimental and theoretical research left the question of many-body-localization in higher dimensional bosonic systems unsettled. In this thesis, we study the dynamics of a two-dimensional interacting many-body state in a optical lattice with adjustable on-site disorder. The thermalization behavior after an excitation by particle removal is observed by following the dynamical evolution and we quantify the resulting steady state by local and global observables. Thereby we are able to identify the phase transition of an ergodic system to a many-body localized system for an interacting bosonic gas as a function of the disorder strength. In the localized regime, the final state is characterized with a density decay length, hinting at a divergence at the transition point.

Outline

After this introduction, the thesis starts with an introduction to ultracold quantum gases in optical lattices, which is well described by the Bose-Hubbard model. In this chapter, the mapping of this model to the Heisenberg model is pictured as it is the foundation of the experiments on quantum magnetism.

The experimental setup and the measurement techniques used in this thesis are introduced in the third chapter. The major steps towards a single site resolved detection of a two dimensional quantum gas are described here. Subsequently the manipulation of the quantum gas with single site addressing and magnetic fields is discussed in more detail.

The fourth chapter focuses on the three experiments illustrating the coherent propagation of an impurity after a local quench. Deep in the Mott insulating regime the impurities are identified as Heisenberg spins. We report on measurements showing the associated propagation of spin entanglement and the formation of bound states.

Chapter 5 deals with the time evolution of a globally highly excited spin system. In contrast to the previous chapter, no coherent evolution is seen but a decay to a homogeneous state hints at thermalization. Here, we determine the time scale of the decay process as a function of the imprinted spin torsion in one and two dimensions.

Chapter 6 provides an overview on theoretical aspects of thermalization in quantum mechanical systems. Many-body localization is introduced as a general state of matter which violates ergodicity and hence does not thermalize.

In the next chapter we report how a disorder potential influences the dynamics of an interacting many-body system. With several different observables the transition of a thermalizing, ergodic gas to a many-body localized phase is analyzed.

The thesis ends with a chapter summarizing the results and giving an outlook on existing open question which can be accessed with our experimental setup.

List of publications

The following articles have been published in refereed journals in the context of this thesis. The articles most relevant for this thesis are shown in bold font.

J. Zeiher, R. van Bijnen, P. Schauß, S. Hild, J.-y. Choi, T. Pohl, I. Bloch, C. Gross
Many-body interferometry of a Rydberg-dressed spin lattice
Nature Physics **advance online publication** (2016)

S. Hild, J.-y. Choi, J. Zeiher, P. Schauß, A. Rubio-Abadal, T. Yefsah, V. Khemani, D. A. Huse, T. Bloch, Christian Gross
Exploring the many-body localization transition in two dimensions
Science **352**, 1547–1552 (2016)

J. Zeiher, P. Schauß, S. Hild, T. Macrì, I. Bloch, C. Gross
Microscopy of a scalable superatom
Phys. Rev. X **5**, 031015 (2015)

P. Schauß, J. Zeiher, T. Fukuhara, S. Hild, M. Cheneau, T. Macrì, T. Pohl, I. Bloch, C. Gross
Crystallization in Ising quantum magnets
Science **347**, 1455–1458 (2015)

S. Hild, T. Fukuhara, P. Schauß, J. Zeiher, M. Knap, E. Demler, I. Bloch, C. Gross
Far-from-Equilibrium Spin Transport in Heisenberg Quantum Magnets
Phys. Rev. Lett. **113**, 147205 (2014)

T. Fukuhara, P. Schauß, M. Endres, S. Hild, M. Cheneau, I. Bloch, C. Gross
Microscopic observation of magnon bound states and their dynamics
Nature **502**, 76–79 (2013)

T. Fukuhara, A. Kantian, M. Endres, M. Cheneau, P. Schauß, S. Hild, D. Bellem, U. Schollwöck, T. Giamarchi, C. Gross, I. Bloch, S. Kuhr
Quantum dynamics of a mobile spin impurity
Nature Physics **9**, 235–241 (2013)

P. Schauß, M. Cheneau, M. Endres, T. Fukuhara, S. Hild, A. Omran, T. Pohl, C. Gross, S. Kuhr, I. Bloch
Observation of spatially ordered structures in a two-dimensional Rydberg gas
Nature **491**, 87–91 (2012)

2 Ultracold bosons in optical lattices

In this thesis, the motion of ultracold bosons in optical lattices is studied. Therefore, this chapter will give an overview of the necessary background of the Bose-Hubbard model. The model is introduced for a single component gas and the inherent quantum phase transition necessary to form the initial states utilized in the following chapters is presented. After introducing additional components, the mapping to the Heisenberg model is explained. In one-dimension, this system is also represented by the free fermion model. For additional defects within the Heisenberg model, the $t - J$ model is needed to accurately describe the system. This chapter ends with a short overview of other possible realizable models with ultracold atoms, which can be seen as an outlook for further experiments.

2.1 Bose-Hubbard model

The variety of accessible physics with ultracold atoms was drastically enhanced by the addition of periodic optical potentials [51]. These potentials were used before, but only for non-degenerate gases [52–57]. Interference of two or more laser beams produces versatile spatial structures. A standing wave is one of the simplest possible forms, obtained by two counterpropagating beams, which can be extended to a three-dimensional lattice by combining three standing waves along orthogonal axes. We use this light crystal shape for all our experiments. More complex structures like triangular, honeycomb or Kagome lattices where obtained by interference of more beams from different directions.

Deep optical potentials, especially deep lattices, restrict the motion along a certain direction. The dimensionality seen by the cold atoms is effectively reduced, if the motion along a certain direction is completely frozen out and only the ground state of the thereby formed trap is occupied. Within this thesis, this method is used to create effective one- or two-dimensional systems. Ultracold atoms within these light crystal structures are well described by the Bose-Hubbard model. It is one of the simplest many-body models which is not reducible to single-particle theories [58]. The Hubbard model was devel-

oped to describe electrons in the tight binding limit and it neglects coupling to lattice phonons. While this is only an approximation for condensed matter, it is remarkably fulfilled by rigid optical lattices which do not support phonon excitations.

In second quantization for a single component in the lowest band of a periodic structure, the Bose-Hubbard model is written as

$$\begin{aligned}\hat{H}_{BH} = &- J \sum_{\langle j,k \rangle} \hat{a}_j^\dagger \hat{a}_k + \frac{U}{2} \sum_j \hat{n}_j(\hat{n}_j - 1) \\ &+ \mu \sum_j \hat{n}_j + \sum_j V_j \hat{n}_j \,. \end{aligned} \tag{2.1}$$

Here, the bosonic particle creation (annihilation) operator $\hat{a}_k^\dagger$ ($\hat{a}_k$) acts on site k and the sum $\langle j,k \rangle$ connects positions between which tunneling is possible. We consider only next neighbor tunneling because tunneling between lattice sites further apart is exponentially suppressed. The tunneling energy between neighboring lattice sites is given by J, and U is the on-site interaction strength. The local potential at position j is given by V_j and typically originates from the harmonic confinement induced by the curvature of the lattice beams. This term can also include additional disorder potentials as utilized for the many-body localization experiments in Chapter 7. In the following sections of this theoretical introduction this term is mostly neglected for simplicity.

2.1.1 Superfluid to Mott-insulator phase transition

The existence of the quantum phase transition from a superfluid (SF) to a Mott-insulating (MI) state was first detected with controllable optical lattices [9], soon after the first proposal for ultracold atoms in a 3D optical lattice [59]. Shallow optical lattices do not have a strong effect on the mobility of the atoms, which can still move freely. In this limit of weak lattices, the kinetic energy is much higher than the interaction energy, and the bosonic gas is consequently in the superfluid phase. This bosonic state has global phase coherence, which results in high contrast diffraction peaks. At the same time, the local atom numbers on each lattice position, canonical partner variable of the phase, experiences strong fluctuations following a Poisson distribution [60].

The periodic barriers of the lattice increase with the lattice depth, leading to a suppression of the tunnel coupling between neighboring lattice sites. In the regime, where the tunnel coupling is weak compared to the interaction strength, the total ground state is given by equal filling for all lattice sites in order to minimize the interaction energy. The resulting MI state has

strongly suppressed fluctuations in atom number, and is incompressible. At the same time, the phase coherence in the system is lost. The phase transition between the superfluid and the MI regime is well captured by the Bose-Hubbard model. The homogeneous filling of a MI state with unity filling provides a well defined state and is of notable interest as outstanding initial state in this thesis.

2.1.2 Multicomponent systems

Additional degrees of freedom in the onsite occupation are required to simulate for example the Heisenberg model. This can be realized by utilizing distinguishable species, which can be completely different atoms or atoms in different states. Here, we will focus on different hyperfine states of the same atoms as distinguishable components. In this case, additional terms need to be added to the Hamiltonian above (Equation 2.1) by repeating it for each component α and introducing an additional inter-component interaction strength $U_{\alpha,\alpha'}$

$$\begin{aligned}\hat{H}_{BH} = &- \sum_{\langle j,k\rangle,\alpha} J_\alpha \hat{a}^\dagger_{j,\alpha}\hat{a}_{k,\alpha} + \frac{1}{2}\sum_{j,\alpha} U_\alpha \hat{n}_{j,\alpha}(\hat{n}_{j,\alpha}-1) \\ &+ \frac{1}{2}\sum_{j,\alpha,\alpha'} U_{\alpha,\alpha'}\hat{n}_{j,\alpha}\hat{n}_{j,\alpha'} + \sum_{j,\alpha}\mu_\alpha \hat{n}_{j,\alpha} + \sum_{j,\alpha} V_{j,\alpha}\hat{n}_{j,\alpha}\,. \end{aligned} \tag{2.2}$$

In general, the tunneling rate as well as the interaction strength can be different for all components. Here, we focus on the situation where at least the tunneling rate is the same for all components, $J_\alpha = J$, which is typically the case for far detuned optical lattices and for different hyperfine states of the same atomic species composing the multicomponent system.

2.2 Effective models

The simplest realization of the multicomponent Bose-Hubbard model includes two species which introduce a pseudospin degree of freedom. Naturally, we will call the two components $|\uparrow\rangle$ and $|\downarrow\rangle$. The phase diagram of these systems is versatile [61] and deep in the MI phase it includes ferromagnetic spin ordered states and z-antiferromagnetic Néel states.

2.2.1 Heisenberg model

The density in the Mott-insulating state with unity occupation is not a free parameter anymore and the motional degree of freedom is frozen out. Focusing

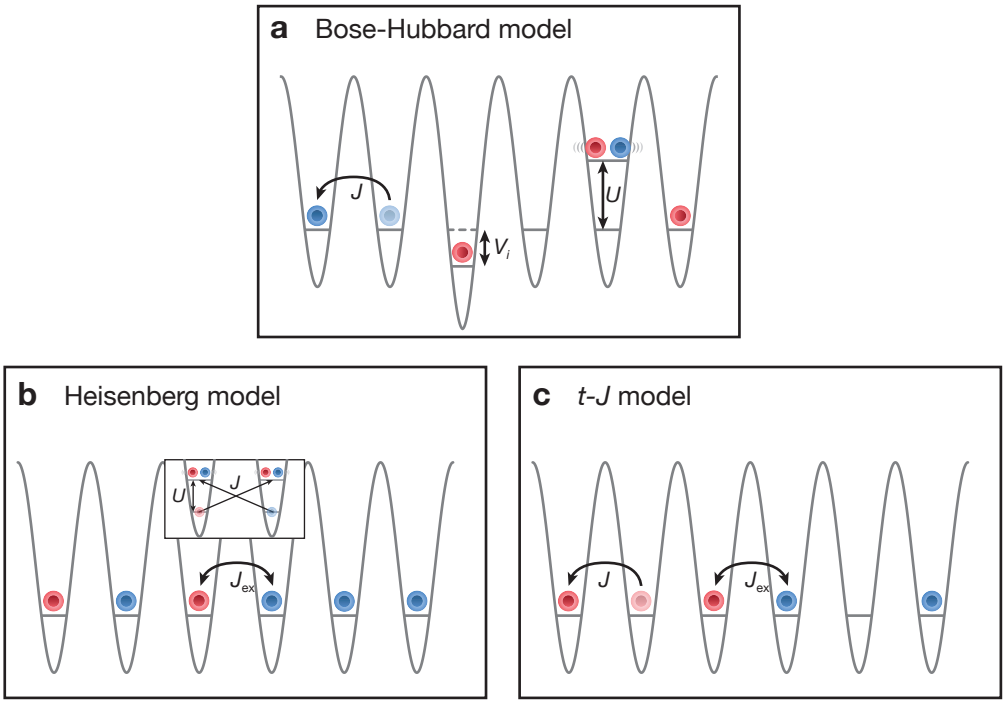

Figure 2.1: Bose-Hubbard model and derived effective models. **a**, Visualization of the Bose-Hubbard model with the tunneling energy J, on-site interaction energy U and the spatially varying potential V_i for two different components illustrated with red and blue color. **b**, For a system with exactly unity filling, the two-component Bose-Hubbard model can be mapped to the Heisenberg model, where spin exchange coupling $J_{ex} = 4J^2/U$ is the only remaining parameter. The inset shows the intermediate states, suppressed by U, which mediate the exchange interaction J_{ex}. **c** The $t - J$ model can be seen as in between the Heisenberg and Bose-Hubbard model. It describes a spin interaction like the one of the Heisenberg model with additional holes which move with a coupling strength of J. Therefore, the on-site density is restricted to one and below.

at this regime, the remaining degree of freedom of the occupation type can be associated with a spin [62, 63]. The next neighbor spin interaction arises from second-order perturbation theory. Two neighboring spins are connected via virtual hopping to states with double occupation which are strongly suppressed by the on-site interaction U. This transforms the local interaction of the Bose-Hubbard model to a next neighbor interaction. Effective spin-1/2 operators are constructed from the creation and annihilation operators and

the corresponding number operators of the two components:

$$\begin{aligned}\hat{S}_j^x =& \frac{1}{2}\left(\hat{a}_{\uparrow,j}^\dagger \hat{a}_{\downarrow,j} + \hat{a}_{\downarrow,j}^\dagger \hat{a}_{\uparrow,j}\right)\\ \hat{S}_j^y =& \frac{1}{2i}\left(\hat{a}_{\uparrow,j}^\dagger \hat{a}_{\downarrow,j} - \hat{a}_{\downarrow,j}^\dagger \hat{a}_{\uparrow,j}\right)\\ \hat{S}_j^z =& \frac{1}{2}\left(\hat{n}_{\uparrow,j} - \hat{n}_{\downarrow,j}\right) .\end{aligned}$$

This leads to the well-known and intensively studied XXZ-Heisenberg model [62, 63], which arises in many condensed matter systems [64]:

$$\hat{H}_H = -J_{\mathrm{ex}} \sum_{\langle j,k\rangle} \Delta \cdot \hat{S}_j^z \hat{S}_k^z + \frac{1}{2}\left(\hat{S}_j^+ \hat{S}_k^- + \hat{S}_j^- \hat{S}_k^+\right) \tag{2.3}$$

$$J_{\mathrm{ex}} = \frac{4J^2}{U} \tag{2.4}$$

$$\Delta = \frac{U_{\uparrow\downarrow}(U_{\uparrow\uparrow} + U_{\downarrow\downarrow}) - U_{\uparrow\uparrow}U_{\downarrow\downarrow}}{U_{\uparrow\uparrow}U_{\downarrow\downarrow}} .$$

The XXZ-Heisenberg Hamiltonian commutes with $S_{\mathrm{tot}}^z = \sum_i S_i^z$ which thus is a conserved quantity. In cold atom experiments, this is often realized by large spatially homogeneous "effective magnetic fields" and a large energy difference between both components prohibits spin changing collisions. For $\Delta > 1$ this model favors a ferromagnetic phase where the ground state is aligned along the z-axis. In the special case where the interactions are all equal $U_{\uparrow\downarrow} = U_{\uparrow\uparrow} = U_{\downarrow\downarrow}$, the isotropic Heisenberg model is realized with $\Delta = 1$. For $\Delta < -1$ the system is anti-ferromagnetic with the Néel state as ground state in the limit of $\Delta \to -\infty$. The ground state at finite Δ is Néel-state like with admixture of quantum fluctuations. At $\Delta = -1$ the overlap of the ground state and the Néel state is still larger than 60 % [65]. When $\Delta \to \infty$, the Néel state is, instead, the highest energy state. For $-1 < \Delta < 1$ the system is in the XY ferromagnetic phase where all spins are aligned in the XY plane.

A harmonic confinement potential, for example, introduces an additional energy offset between neighboring lattice sites, and the coupling strength J_{ex} between two sites is weakly modified. For an offset between these two sites of Δ, the coupling strength is only modified in second order to $J'_{\mathrm{ex}} = J_{\mathrm{ex}} \cdot U^2/(U^2 + \Delta^2) \approx J_{\mathrm{ex}} \cdot (1 - \Delta^2/U^2)$. The spin exchange coupling is much less effected by an energy offset than the tunneling rate J, which is modified in second order as $J' = J\sqrt{1 + \Delta^2/J^2} \approx J(1 + \Delta^2/J^2)$. The systems needs to be in the MI regime with $U > J$ for a valid mapping to the Heisenberg regime. Thus the influence of the offset energy is substantially different for a single impurity than for a spin impurity at the same lattice depth. The unity filling

effectively screens the confinement potential and therefore potential offsets can be often neglected.

Note that the Hamiltonian above (Equation 2.3) is valid for bosonic components only. For fermions the intra-component interaction ($U_{\uparrow\uparrow}$ and $U_{\downarrow\downarrow}$) is infinite due to Pauli blocking. Taking into account the fermionic commutation relations, the parameter Δ is fixed to the anti-ferromagnetic case for $\Delta = -1$ [31].

The spin-1/2 Heisenberg model is one of the foundational models for interacting quantum spins and might be the best studied one as well. This model was solved analytically in one dimension in the early 1930's by H. Bethe using a systematic ansatz for the form of the eigenvectors [6]. It is a very pedagogic model of quantum mechanics, which was numerically solved with several different approaches and served as a toy model for frustration in triangular lattice with anti-ferromagnetic interaction [64]. Nevertheless, calculating transport properties and time correlation for out-of-equilibrium systems is challenging, especially if integrability is broken [66]. In solid state physics, the one dimension Heisenberg model describes for example the propagation of magnetic excitation in spin-chain materials [67].

Superexchange interactions were controlled and studied at first in a double well structure with ultracold bosons [32]. Furthermore it has been shown that the exchange coupling strength can be fully controlled in amplitude and in sign by lattice shaking [68]. Additionally, ions have been suggested to be used to simulate spin system [69–71] and several experiments have simulated Ising models with variable range interaction [33, 72–74]. Higher SU(N) spin Hamiltonians can be realized with alkali and alkaline-earth-like atoms [75, 76]. First demonstrations of SU(N) systems with Ytterbium and Strontium have been performed [77, 78].

Quantum random walk

The release and subsequent tracking of a single initially fully localized impurity is a helpful method to investigate fundamental properties of the underlying Hamiltonian. We present the detection of coherent propagation of spin impurities in a Heisenberg spin chain in Chapter 4. Therefore the general notion of continuous quantum random walks is introduced here. This description applies to the here relevant situation of a spin impurity as well as the motion of a single particle [15].

The propagation within a system, allowing a coherent quantum evolution, is significantly influenced by constructive and destructive interference. The following considerations assume a system with only next neighbor coupling J_{ex}. For a classical random walk, the particle has to choose at each position which direction it takes. The distance to the original position for this process

follows a normal distribution where the width in 1D is given by $\sigma = \sqrt{J_{\mathrm{ex}} t}$. The most probable position after any time for the classical case is the starting point. The linear scaling relation of $\sigma^2 \propto t$ is referred to as normal diffusion. An example of classical random walk is Brownian motion.

A 1D system with pure next neighbor coupling J_{ex} is a simple toy model for a quantum random walk. This can be realized by a Heisenberg system with $\Delta = 0$. Furthermore, Δ does not play a role in the subspace of a single impurity in a spin polarized bath because the number of boundaries between different spin polarizations is fixed to the number of next neighbors. It is interesting to know the probability amplitude $p(|n-m|,t)$ at lattice site n after starting at position m under the time evolution of t:

$$p(|n-m|,t) = \left| \langle n | \, e^{-\frac{1}{\hbar} H t} \, | m \rangle \right|^2 . \tag{2.5}$$

This can be rewritten by expanding the momentum states as $|p\rangle = \sum_m e^{ipm} |m\rangle$, which diagonalize the Hamiltonian $H = J_{\mathrm{ex}} \sum_{\langle j,k \rangle} \hat{a}_j^\dagger \hat{a}_k$, where $|m\rangle$ are the states with the impurity localized at position m. The corresponding eigenenergy of the eigenstate $|p\rangle$ is $2\, J_{\mathrm{ex}} \cos p$. Thus, the above formula can be rewritten as:

$$p(|n-m|,t) = \left| \frac{1}{2\pi} \int_{-\pi}^{\pi} e^{i(p(n-m) - 2J_{\mathrm{ex}} t \cos(p)} dp \right|^2 \tag{2.6}$$

$$p(|n-m|,t) = \left| (-i)^{n-m} J_{n-m}(2J_{\mathrm{ex}} t) \right|^2$$

$$p(|n-m|,t) = \left| J_{n-m}(2J_{\mathrm{ex}} t) \right|^2 . \tag{2.7}$$

Here, the Bessel function $J_\nu(x)$ is exponentially suppressed for $\nu \gg x$ and the wavefronts travel outwards with a velocity of $2J_{\mathrm{ex}} t$ [79]. Hence, the quantum propagation, for example in a Heisenberg spin system, is ballistic as the wavefunction expands linear in time, much faster than the diffusive classical random walk. This has been observed for single atoms in the here discussed continuous case [15] and in the similar discrete case [80]. The coherence of the system can be destroyed for example by projective measurements during the propagation. This loss of coherence leads to a transformation of the probability distribution towards the classical Gaussian distribution [80]. Therefore, The significant two outer peaks of the Bessel function as well as the linear expansion can be seen as signature of coherent propagation.

2.2.2 Spinless fermion model

In one dimension, the XXZ Heisenberg model for spin $1/2$ is mapped to the spinless fermion model via a non-local Jordan-Wigner transformation [31, 64,

81]:

$$\begin{aligned}\hat{S}_j^+ =& \hat{c}_j^\dagger e^{i\pi \sum_{p=1}^{j-1} \hat{c}_p^\dagger \hat{c}_p} \\ \hat{S}_j^z =& \hat{c}_j^\dagger \hat{c}_j - \frac{1}{2}\,. \end{aligned} \tag{2.8}$$

Here, $\hat{c}_j^\dagger$ ($\hat{c}_j$) are fermionic creation (annihilation) operators for a particle on site j, which obey anticommutation relation $\{\hat{c}_j^{(\dagger)}, \hat{c}_j^{(\dagger)}\} = 0$. Following this mapping, a fermion corresponds to $S_j^z = +1/2$ and no fermion accordingly to $S_j^z = -1/2$. The resulting Hamiltonian is given by

$$H_{\text{fermion}} = J_{\text{ex}} \sum_j \frac{1}{2} \left(\hat{c}_j^\dagger \hat{c}_{j+1} + \hat{c}_{j+1}^\dagger \hat{c}_j \right) + \Delta \left(\hat{c}_j^\dagger \hat{c}_j - \frac{1}{2} \right) \left(\hat{c}_{j+1}^\dagger \hat{c}_{j+1} - \frac{1}{2} \right) \tag{2.9}$$

The implication of this mapping becomes visible in the experiment with two spin impurities which behave like free fermions and thus anti-bunch (see Chapter 4.3 for details). So far no similar mapping in higher dimensions was found.

2.2.3 $t - J$ model

The absolute ground state needs to be reached to fulfill the requirement that the underlying Mott-insulating state has perfect unity filling. Otherwise, thermal fluctuations induce holes or double or higher occupancy. In the regime where U is much higher than J and the chemical potential is below U, the first order corrections include only holes. In addition to the spin interaction governed by J_{ex}, the necessary model must include the motion of these holes governed by J. The $t - J$ mode,l which describes the physics of doped Mott insulators [82], is exactly developed for this situation. In our nomenclature, the $t - J$ model would be titled $J - J_{\text{ex}}$ model and the Hamiltonian reads

$$\begin{aligned} H_{t-J} =& - J \sum_{\langle j,k \rangle, \alpha} \hat{a}_{j,\alpha}^\dagger \hat{a}_{k,\alpha} \\ & - J_{\text{ex}} \sum_{\langle j,k \rangle} \Delta \cdot \hat{S}_j^z \hat{S}_k^z + \frac{1}{2} \left(\hat{S}_j^+ \hat{S}_k^- + \hat{S}_j^- \hat{S}_k^+ \right) - \frac{1}{4} \hat{n}_j \hat{n}_k \end{aligned} \tag{2.10}$$

The operators are defined as above and $\hat{n}_j = \hat{n}_{j,\uparrow} + \hat{n}_{j,\downarrow}$ measures the total density on site j. The Hilbert space of this Hamiltonian is much smaller than that of the Bose-Hubbard model and can be numerically exactly solved

for system sizes much bigger than the maximal possible size for the Bose-Hubbard model. The influence of the faster moving holes cannot be neglected as the holes can change the phases of the spins destroying coherence. The effect of these holes was studied in the experiments dealing with the ballistic dynamics of spin impurities (see Chapter 4). It is important to note that the Heisenberg model is integrable but the $t - J$ model is only integrable in certain cases [64, 83, 84].

2.2.4 Additional models

The above mentioned effective models are relevant for the next chapters. Several more effective models can be realized with ultracold atoms [85]. Important for 1D systems similar to ours is the description by The Lieb-Liniger model is another important model describing 1D systems [86]. This model is an academically interesting toy model, because it is analytically solvable. A key property, the two different excitation branches, can be mapped out with Bragg spectroscopy [87]. So far, evidences have only been seen by the shape of the resonance for fixed momentum [88]. In the limit of strong interaction, which can be reached either with lower density or higher scattering length, the bosons become impenetrable and follow the description of the Tonks-Giradeau gas [89]. This has been realized with ultracold Rubidium [90] and in-situ imaging could lead to detection of highly correlated states.

Ultracold atom experiments also began to realize long-range interacting models. This long-range interaction can be realized for example with polar molecules [91–93], magnetic atoms [94, 95] and atoms in Rydberg states [96]. During the emergence of this thesis we also worked on long-range Rydberg experiments where we studied the pulsed and controlled preparation of crystal-like spatially distributed Rydberg states [97, 98], the formation of collective super atoms [99] and the detection of dressed Rydberg interaction via many-body interferometry [96]. In future, the combination of competing long-range and short-range order will provide interesting new physics. These models are not introduced in detail here because they are not covered by the experiments presented in this thesis and detailed information can be found in the citations.

3 Experimental setup and measurement techniques

This chapter gives an overview on the relevant parameters of the experimental system and explains the basic experimental sequence leading to the initial state for the experiment described in the further course of this work. Furthermore we will give an introduction to basic manipulation and measurement techniques that are relevant for our quantum gas microscope. Detailed information about the calibration process of the addressing potential and the magnetic field are also provided.

3.1 Production of ultracold 2D degenerate Bose gas

The experimental sequence was described in detail in the first PhD theses written about the construction and the first measurements of the single atom experiments [100–102]. Here we focus on certain aspects that have been changed or are of high relevance for this thesis.

The experiments start with loading bosonic Rubidium-87 atoms from a background gas at room temperature in a two-dimensional magneto optical trap (MOT). This creates an atom beam which is sent to a 3D MOT, where the atoms are slowed down to the Doppler limit in all three spatial directions. The atoms are further cooled by microwave evaporation in a magnetic trap. In contrast to previous experiments [100, 101] the evaporation speed was optimized for the same final temperature and a total of 5 s were saved. Thereafter, the atomic cloud is optically transported from the MOT chamber to the science chamber and the atoms are captured in a crossed optical dipole trap. The temperature is further reduced by evaporation in this trap, which is stopped right before the phase transition to a Bose-Einstein condensate (BEC). The gas is subsequently loaded into a vertical standing wave along the imaging axis (z-direction). We select a single horizontal plane of the standing wave and remove all the other atoms by combining a strong magnetic field gradient, introducing a z dependent detuning with microwave spin transfers between the $|F = 1, m_F = -1\rangle$ and $|F = 2, m_F = -2\rangle$ hyperfine

states. The two-dimensional gas is cooled down to degeneracy in a following double step evaporation. The effective potential experienced by the atoms is tilted in the horizontal direction with a magnetic field gradient and the cloud is loaded into a strongly focused so called "dimple" beam (diameter of a few micrometers) while the depth of z-lattice is quickly reduced. In a second step, the intensity of the dimple beam is slowly reduced within one second. At the final intensity value only the coldest atoms are trapped and the atom number is limited by three body collisions inside the tight trapping potential of the dimple beam. We remove the tilt of the potential and adiabatically release the cloud back into a single plane of the z-lattice. The further transformation of this two-dimensional degenerate gas is described in the next sections. The total duration of a sequence including all steps above, state preparation, propagation and detection is approximately 20 s. Figure 3.1 gives an overview of the duration of the main blocks of the experimental sequence.

The total duration of the experimental cycle is still dominated by the combination of all evaporation steps. However, newer state of the art quantum gas machines have shown a significantly faster production of BECs. Several of these advanced methods were demonstrated with different atomic species but should be also applicable to Rubidium. These faster sequences make use of more advanced laser cooling techniques in order to accomplish a lower initial temperature [103]. Furthermore, a fast evaporation can be attained by higher collision rates in stronger confining traps. A significant speed-up was demonstrated by evaporation in a high power optical trap generated by a CO_2 laser [104]. An impressive example is the fast pure laser cooling to degeneracy with Strontium on a time scale of 100 ms [105].

3.2 Quantum phase transition to Mott insulator

The degenerate 2D Bose gas in a single anti-node of the z-lattice is exposed to an additional in-plane square lattice. As soon as the lattice depth has reached a certain amplitude, the superfluid state undergoes a quantum phase transition to the Mott-insulating phase as presented in Chapter 2.1.1. The x and y lattices are turned on with a double s-shaped ramp within 150 ms to at least a lattice depth of $20\,E_r$ with the intermediate plateau at $10\,E_r$. We quantify the lattice depth in units of the recoil energy $E_r = h^2/8ma_{lat}$, with the Planck constant h, the Rubidium mass m and the lattice constant a_{lat}. In the case of our lattice ($a_{lat} = 532\,nm$), the recoil energy is given by $E_r \approx h\,2\,kHz$. This procedure was optimized to reduce the number of defects in the final MI. Very importantly, the crossing point of the x- and y-lattices need to fit the center of the z lattice in order to minimizes the necessary mass transport to achieve low temperatures. Higher temperatures lead to an increased number

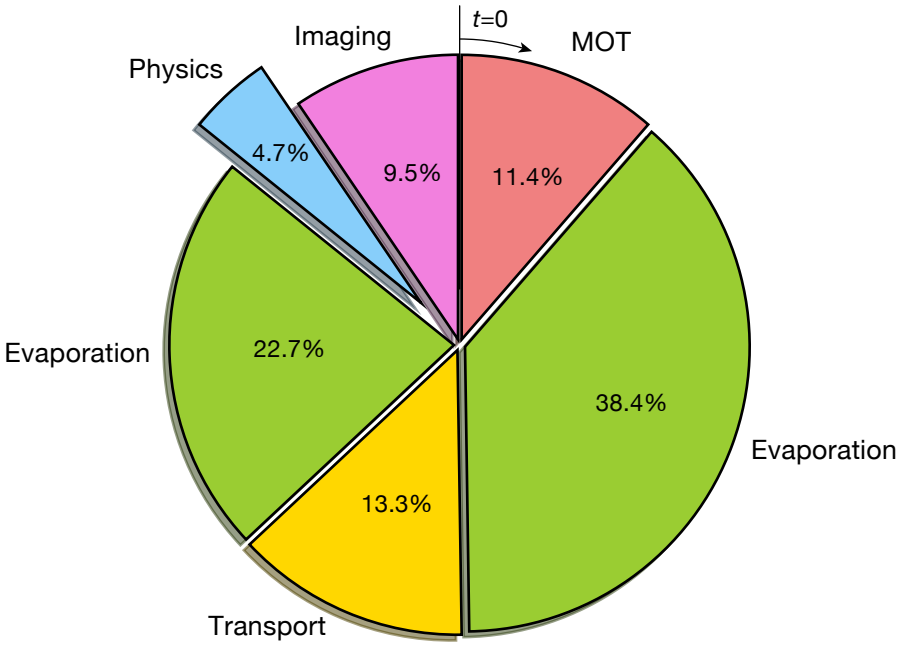

Figure 3.1: Experimental sequence. The sequence starts with a magneto-optical trap (MOT) (2 s), followed by the MW evaporation (6.5 s). The cold gas is optically transported (2.5 s) to the science chamber where a second evaporation to degeneracy follows with the slicing in between (5 s). In a typical sequence for many-body dynamics as described in this section, the state preparation and time evolution lasts approximately 1 s. All sequences end with the imaging process which requires two pictures with 1 s exposure each.

of defects in the MI state which are most likely double occupied and empty lattice sites. The total number of atoms is controlled by the final evaporation depth of the dimple trap and is typically chosen to be close to the maximum possible atom number without leaving the unity filling regime with one atom per lattice site. This state is the starting point for all experiments described in this thesis. The typical atom number for such a MI state is 120 at a lattice depth of 20 E_r for all three axes. Without additional hold time and manipulation the average number of defects in the center can be as low as one defect per realization over several 10 shots (see Figure 3.4 for example fluorescence images).

3.2.1 Optimized lattice ramp for 1D gases

The typical 2D adiabatic preparation of the MI state is done with a slow lattice ramp that tries to avoid to excite the system, but is not optimized with

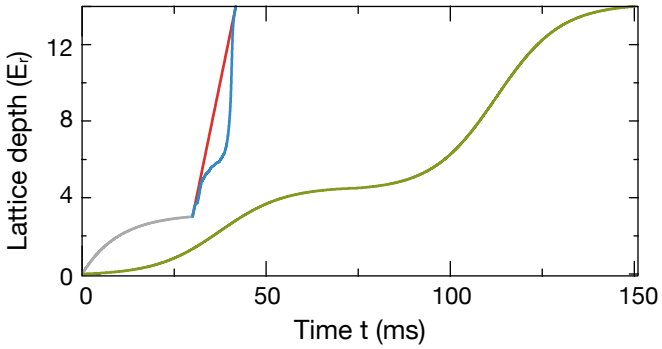

Figure 3.2: Optimized 1D lattice ramp. The chosen adiabatic ramp is plotted in green. The blue ramp, optimized by the CRAB algorithm, leads to MIs with the same amount of excitations and created clearly less excitations than the linear ramp (red). The numerically optimized lattice ramp only starts at a lattice depth of $3\,E_r$ to ensure that the CRAB algorithm for the Bose-Hubbard model is valid.

respect to the total duration. Transformations of quantum systems, like this lattice ramp, can be optimized with the Chopped RAndom Basis (CRAB) algorithm to find the optimal control [106, 107]. The result allows to operate at the quantum speed limited which is the theoretically fastest possible transformation [**van_frank_optimal_2015**]. We have demonstrated that this method performs as expected for a one dimensional Bose gas and the duration of the lattice ramp was reduced to 11.75 ms instead of 120 ms for a slow adiabatic reference ramp. Furthermore, the optimized lattice ramp was compared to a linear ramp with same duration, creating a significant amount of additional excitations. However, the optimized function only starts at $3\,E_r$ to ensure that the single band approximation of the Bose-Hubbard model still applies. To overcome the the not optimized initial low lattice depth, the lattice is initially slowly increased to $3\,E_r$ ensuring that this process does not heat the sample. The three different lattice ramps are plotted in Figure 3.2. Despite this speed up, the average central density did not change indicating that the system did not get more excited [**van_frank_optimal_2015**]. This optimization method could be extended to two-dimensional systems. However, it is not possible to simulate the two-dimensional quantum gas numerically and the algorithm would need to use actual simulations with the quantum gas microscope itself instead of calculations. These optimization methods are typically important for time critical operations. For the present problem of crossing SF-MI phase transition, decoherence processes, like photon scattering and background gas collisions, occur on much longer time scales than the duration of the above described lattice ramp. For our current experiments, an optimization of the

lattice ramp is consequently irrelevant.

3.2.2 Lattice parameters

The tunneling rate and the interaction strength strongly depend on the lattice depth, making the lattice depth one of the most crucial parameters in our experiments. Only exact knowledge about the tunneling rate allows to compare different experimental runs and hence, the lattices need to be calibrated for all experiments utilizing dynamical evolution in the lattice. For Rubidium, the lattice depth is the only possibility to tune the ratio of the interaction strength to the tunneling rate, because no Feshbach resonance at a reachable magnetic field exists.

The lattice depth can be precisely calculated by the fully known from the spectral properties of an atom and the well understood light shift [108]. The lattice depth depends linearly on the optical power which is therefore stabilized with a PID circuit. Fluctuations in the alignment of the two counter propagating laser beams, forming that lattice, change the calibration of the intensity stabilization and day to day differences up to 10 % were observed.

Interaction and hopping rate in optical lattices

The two parameters of the Heisenberg Hamiltonian, J and U, can be calculated from the exponentially localized, real Wannier states of the applied optical lattice. The Wannier state $w(x - x_i)$ localized on position x_i is calculated for a known lattice depth and the coupling strength $J_{i,j}$ between two lattice sites (i and j) is given by the overlap integral of a Wannier state localized on site i with the time evolved state from site j:

$$J_{i,j} = \int d^3x w^*(x_i - x_j) \left(-\frac{\hbar^2}{2m}\nabla^2 + V_0(x) \right) w(x_i - x_j) \tag{3.1}$$

This tunneling rate is the only relevant parameter for single particle tunneling as measured in [15]. From the time evolution of the single particle state the next-neighbor tunneling rate J can be determined by fitting the experimental data with the theoretically expected Bessel function. For the final density distribution, the coupling strength is the only free parameter (see Chapter 2.2.1). The thereby directly obtained tunneling rate agrees within the experimental uncertainties with the ab initio value calculated with Equation 3.1 [15].

The interaction for ultracold ground state atom is determined by s-wave scattering and the interaction potential can be approximated to be δ-like with the scattering length a_s as the only necessary parameter to characterize the

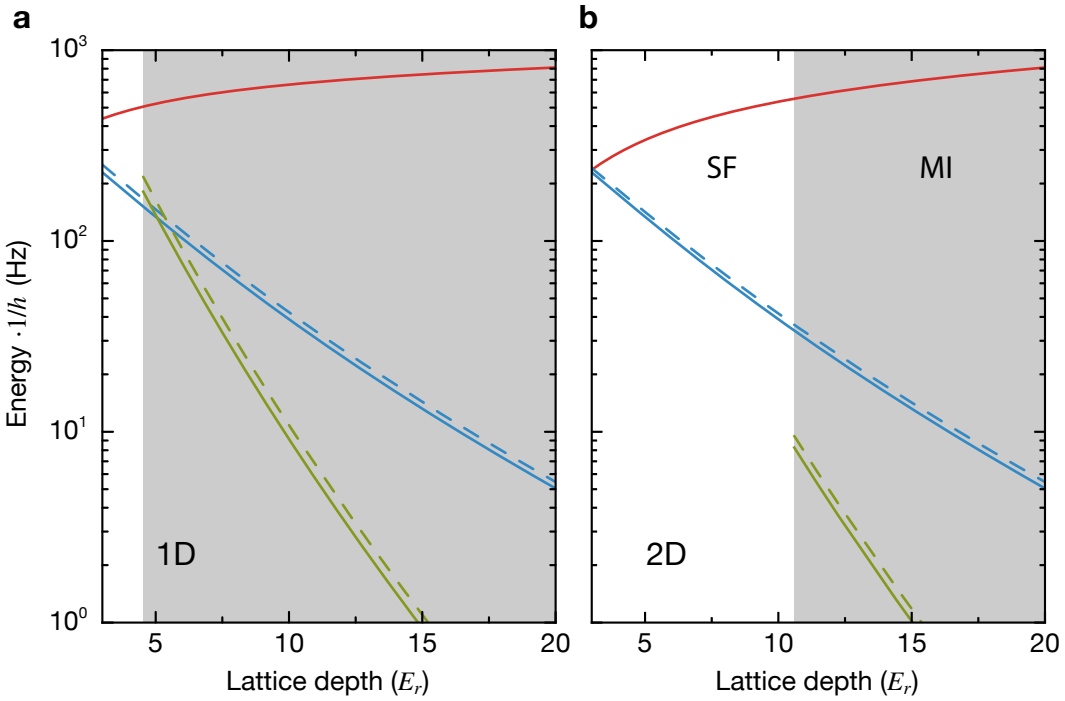

Figure 3.3: Interaction and tunneling energy. Interaction (red), tunneling (blue) and spin exchange energy (green) as a function of the lattice depth for 1D (**a**) and 2D (**b**). The additional (two) lattice depth(s) is (are) fixed to 20 E_r. Spin exchange can only be defined deep in the Mott insulating region (MI), marked in gray and therefore is not plotted in the superfluid (SF) region. The dashed lines include density corrections for unity filling. The grey shaded regions mark the MI regime up to the transition point for the infinite system which is in 1D at $(U/J)_c = 3.4$ and in 2D at $(U/J)_c = 16.4$.

interaction. The interaction strength U in the Bose-Hubbard model depends on the scattering length and the Wannier states as follows:

$$U = \frac{4\pi a_s}{m} \int d^3x \, |w(x)|^4 \, . \tag{3.2}$$

Within our experiments the ratio of the interaction energy to the tunneling energy is important in order to know the lattice depth for the transition point between the superfluid and the Mott-insulating phase. Furthermore both parameters are also crucial to determine the spin interaction strength $J_{ex} = 4J^2/U$ of the Heisenberg model described in Chapter 2.2.1.

Density correction

While the tunneling rate was measured directly, the on-site interaction energy was not independently determined. However, the spin exchange rate J_{ex} as a function of both parameters was determined. This parameter of the Heisenberg model was measured by tracing the coherent evolution of a single spin impurity deep in the Mott-insulating regime (see Chapter 2.1.1 for details). We observed a systematic offset towards higher coupling strength compared to the ab initio calculated values. An experiment studying in detailed Bloch oscillations in tilted lattices revealed density-induced changes of the tunneling rate [109]. The corrected coupling strength between sites i and j includes the tunneling rate as defined in 3.1 and an additional term to include these density effects:

$$\begin{aligned} J_D =& J + (n_i + n_j - 1) a_s \Delta J \\ \Delta J =& -\frac{4\pi\hbar^2}{m} \int d^3x w^*(x - x_i) w^*(x - x_j) \left| w(x - x_j) \right|^2 \end{aligned} \tag{3.3}$$

These corrections explain most of the previously observed systematic offset. Figure 3.3 shows the expected spin exchange coupling strength as well as tunneling rates with and without corrections for unity filling.

State dependent interaction

Above calculations were based on a single scattering length $a_s = 100\, a_0$ characterizing all interactions, with the Bohr radius a_0. This is a good approximation for our setup with Rubidium-87 as the scattering lengths between different spin states only differ by 1 %. There is only one Feshbach resonance at magnetic fields below 100 G which is reachable with our setup [110]. It is between the two hyperfine state $|F = 1, m_F = -1\rangle$ and $|F = 2, m_F = 1\rangle$ at 9.1 G [111, 112]. We do not use these hyperfine states to avoid possible spin changing collisions.

For the two hyperfine states utilized in this thesis ($|\downarrow\rangle \equiv |F = 1, m_F = -1\rangle$ and $|\uparrow\rangle \equiv |F = 2, m_F = -2\rangle$), the relevant scattering lengths are $a_{\downarrow\downarrow} = 100.4\, \mathrm{a}_0$, $a_{\downarrow\uparrow} = 99.0\, \mathrm{a}_0$ and $a_{\uparrow\uparrow} = 99.0\, \mathrm{a}_0$ [113, 114]. The slightly different interaction strengths lead to an XXZ-Heisenberg Hamiltonian with Δ deviating from unity, $\Delta = 0.986$. This follows directly from Equation 2.3 since the interaction strength linearly depends on the scattering length. In experiments beyond this thesis, the above mentioned Feshbach resonance could be useful to tune Δ and realize Heisenberg interactions with Δ above or below 1.

Lattice calibration

Several options to precisely determine the lattice depth exist [115]. Pulsing on a standing light wave creates a diffraction pattern because it imprint multiples of the lattice momentum k_{lat} [116, 117]. The resulting momentum distribution can be measured with a time of flight image where the initial momentum distribution is mapped to position space. By comparing the relative height of the diffraction peaks the lattice depth can be estimated.

A similar method measures Rabi oscillations between the lowest and the second lowest band, initiated after a sudden lattice switch-on and can be detected after interference of both bands in a time of flight image. For this method the standing wave is switched on significantly longer [118].

In addition, atoms can be adiabatically loaded into the lattice which is thereafter switched off suddenly. For this method, the lattice depth is extracted from the relative sidepeak height of the obtained interference pattern [119].

These methods are difficult to implement in an in-situ experiment because it is necessary to study the interference patterns after time of flight. In our system, this imaging technique is limited by the distance of the atom to the vacuum window and no good mapping of the momentum distribution to position space is possible. Instead, we use frequency-modulation spectroscopy for which the lattice amplitude is periodically modulated [120]. At low temperatures the atoms are initially loaded into the lowest band. A transfer to an higher band only occurs, if the modulation frequency matches the band gap. Since the periodic lattice amplitude modulation conserves the parity of the wave function atoms can only be coupled to every second band. After the transfer to higher bands, the atoms quickly spread out at low lattice depth due to their higher mobility. The band structure especially the band gaps can be exactly calculated for non interacting atoms [121], and thus serves as a direct comparison for measuring the lattice depth. This method is especially well suited for quantum gas microscopes as it makes use of the good space-resolved counting ability. The spectroscopically probed resonance acquires a finite width due to the width of each lattice band and the Gaussian spatial intensity modulation of the lattice beams. Within the experiments, the resonance can be located better than 5 % and has proven to be stable over a day within this range.

The lattice depth can be further measured by observing Landau-Zener tunneling in an accelerated lattice [122–124]. Our lattice is retro-reflected from a fixed mirror making it difficult to implement a controlled acceleration.

3.3 Single-site resolved detection

Several experiments [13–16, 27, 28, 97–99, 125], especially those described in this thesis, are based on in-situ single-atom resolved detection. The first fluorescence images of two-dimensional ultracold quantum gases reaching single lattice site resolution were performed by [10, 11]. The implementation of this technique in our setup is described in great detail in [100]. In the following, we will specify the most relevant parameters and technical properties of the single-site detection as well as its further application to extract physical relevant quantities.

3.3.1 Fluorescence imaging

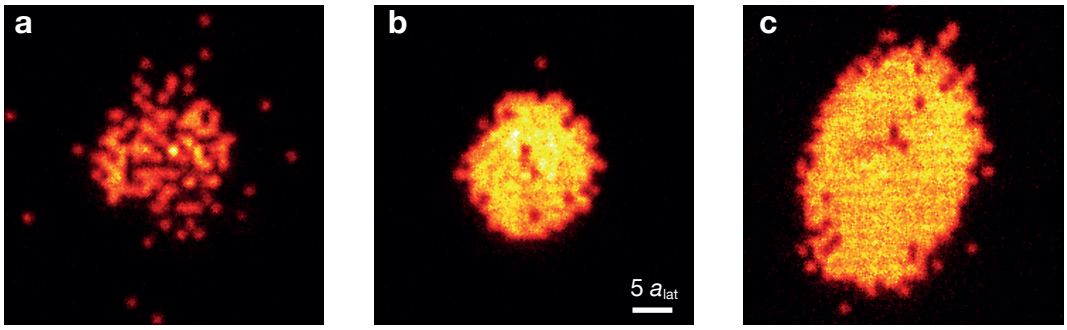

Figure 3.4: Fluorescence images. **a**, mean density of the BEC approaches 0.5 due to the parity projection. **b**, MI with 196 detected atoms, with visible doublon hole defects in the central region. **c**, deconfined MI with 451 detected atoms with a strong asymmetry in the residual confining potential.

The ability to image the in-situ density distribution of a quantum gas localized by a deep optical lattice, is the distinguished feature of a quantum gas microscope. Example image are shown in Figure 3.4. We show typical images of a cloud in a superfluid state as well as in a Mott insulating state with and without deconfinement. During the imaging process, a molasses beam configuration is used to stimulate fluorescence and at the same time laser cool the atoms, while the strong confinement of the optical lattice pins the atoms to fixed positions. The molasses light leads to a photon scattering rate of $\sim$60 kHz of which 5,500 photons per second are detected by the camera through a high resolution objective [10]. During imaging, the temperature of the atoms is immediately drastically increased and saturates at a temperature on the order of 20 µK. The detected distribution is not the original density distribution, because light induced collisions lead to rapid pairwise loss and hence the parity of the density is measured [10, 126]. For the deep lattice

depth of ∼300 µK, the motion of the atoms is strongly suppressed during the duration of imaging of 900 ms even for the relatively high temperatures.

The residual site-to-site-hopping rates are below 1 % per particle. This is measured with MIs imaged twice for only 200 ms at the beginning and the end of the standard illumination period. The built-in custom-made high resolution objective has a numerical aperture of 0.68 and the determined point spread function of single atoms can be well approximated by a Gaussian distribution with a standard deviation of $\sigma = 267(6)$ nm [102]. This leads to overlapping point spread functions of neighboring lattice sites as the spacing is only $a_{\mathrm{lat}} = 532$ nm. The spacing results from the lattice laser operating at a wavelength of 1064 nm. However, using the known underlying periodic lattice structure for a convolution algorithm a reconstruction fidelity of ∼99.5 % is reached.

3.3.2 Mott insulator thermometry

The detected density of a MI is influenced by quantum fluctuations which become smaller as the limit of $J/U \to 0$ is approached and the remaining density fluctuations of the MI state are thermal excitations. Within this limit of very small coupling strength compared to on-site interaction, all lattice sites are decoupled. Before this decoupled regime is approached adiabatically, all lattice sites were in thermal equilibrium. Hence, it is a valid assumption that all lattice sites can be treated as its own physical system described by a single grand canonical ensemble with the same temperature T. Furthermore, within local density approximation the chemical potential $\mu(r)$ is equal for all lattice sites at the same trap potential. This is the only other necessary parameter describing the ensemble. For an isotropic trap, the chemical potential is equal on rings around the center parameterized with radius r. Within this limit the local probability to have n atoms at a radius r, $p(n)$ is given by the Boltzmann factor:

$$\begin{aligned} p(n,r) &= e^{\beta(\mu(r)n - E_n)}/Z\,. \\ Z(r) &= \sum_n e^{\beta(\mu(r)n - E_n)} \end{aligned} \tag{3.4}$$

$Z(r)$ is the grand canonical partition function, $\beta = 1/(k_B T)$ with the Boltzmann constant k_B and $E_n = Un(n-1)/2$ is the interaction energy. Within local density approximation, the local chemical potential $\mu(r)$ is determined by the central chemical potential and the approximately harmonic trapping potential

$$\mu(r) = \mu_0 - m\omega^2 r^2/2 \tag{3.5}$$

This equation assumes a radial symmetric trap but can be easily extended to take into account the existing ellipticity. Consequently, the detected parity signal $n(r)$, taking into account pair-wise loss due to light induced collisions, is given by:

$$\begin{aligned} n(r) &= \sum_n \mathrm{mod}_2(n) p(n,r) \\ &= \frac{1}{Z(r)} \sum_n \mathrm{mod}_2(n) e^{\beta(\mu(r)n - E_n)} . \end{aligned} \tag{3.6}$$

This profile function is fitted to azimuthally averaged density profiles, corrected for the ellipticity. With this fit, we extract the free parameters μ_0, T and sometimes additionally ω if unknown from other independent measurements. The method of MI thermometry is valid for temperatures T (or the corresponding mean thermal energy per particle) and on-site interaction U, both much larger than the tunneling strength J. Simulations in [100] have shown that this method works down to $T = 0.02\,U/k_B$ for large U. The first reported MIs of our experiments observed temperatures as low as $T = 0.074(5)\,U/k_B$, determined with this method [10]. It was confirmed that the entropy per particle is highest at the transition regions between different MI shells and at the edge of the MI. Even lower temperatures of $T = 0.05(1)\,U/k_B$ were measured for the initial states of the experiments observing entanglement propagation described in Chapter 4.2. Furthermore, this method served as a key tool to investigate the Higgs amplitude mode at the 2D superfluid to Mott insulator transition [127]. In Chapter 7, the heating rate of the system was determined with this method although the relevant lattice depth was low and quantum fluctuations were not completely frozen out. Hence, the extracted temperatures can overestimate the mean thermal energy per particle by misleadingly interpreting quantum fluctuations as thermal. In this case thermometry was only possible because the clouds within the reported measurements were clearly hot, satisfying that the mean thermal energy per particle was well above tunneling strength J.

3.3.3 Spin resolved measurements

The experiments studying the ballistic transport in an effective Heisenberg model as well as the experiment on the diffusive dynamics of spin spiral states require to discriminate the two effective spin states represented by two different hyperfine states. The first spin resolved measurements were obtained by Stern and Gerlach by directing a beam of silver atoms through an inhomogeneous magnetic field which leads to spatial separation of the two involved spin states [128–130]. This method has been applied to time of

flight imaging with ultracold atoms to spatially separate different spin components. However, this is not directly possible for in-situ imaging as the spin carrying object needs to be moving. For absorption imaging, typically applied in time of flight detection, it is possible to image a single spin component choosing the laser to be resonant with one of the atomic states but not the other. Also this method is not possible for the utilized molasses fluorescence imaging of Rubidium, because no closed independent cooling cycle for each spin state exists.

Spin resolved fluorescence imaging

All hyperfine states within the $5^2S_{1/2}$ manifold are imaged with the fluorescence method at the same time. Within a few scattering events of the molasses laser light, all spin-information about the initial state is lost as no dark state exists and all states are pumped to the cooling transition. This is undesired if spin resolved data is necessary. The information is partly regained if certain spin states are removed right before imaging. Here a circular polarized laser beam resonant with the transition $5^2S_{1/2}, F = 2$ to $5^2P_{3/2}, F = 3$, which is a closed cycling transition, removes all atoms in the $5^2S_{1/2}, F = 2$ manifold with 99.9 % fidelity. At the same time the population of the $5^2S_{1/2}, F = 1$ state is not significantly changed since multiple photons are scattered before an atom drops out of the closed cycle from $F = 2$ to $F = 1$, due to off-resonant scattering. Photon scattering of atoms in the $F = 1$ state is strongly suppressed by the large detuning of the laser light. Both the effect on atoms in $F = 1$ state and in $F = 2$ can be checked individually with cold Mott insulator states. Prepared in the $F = 1$ hyperfine level, the Mott insulator should not be affected. The Mott insulator is transferred to the $F = 2$ with high fidelity using the repumping transition of the molasses cooling. Subsequently, all atoms should be removed with the hyperfine selective resonant beam. In this thesis the spin states are encoded into states in different hyperfine levels and this method can be applied directly. Otherwise, this method can be combined with spin selective MW transfers to transfer one spin component to a $F = 2$ hyperfine state. An adiabatic passage with the MW over the transition between the $|\downarrow\rangle$ and $|\uparrow\rangle$ inverts the population and thus the removed spin component is chosen. We apply this method for the *negative* and *positive* imaging technique in Chapter 4. *Positive* imaging detects the spin impurity where as *negative* imaging detects the spin bath and the impurity shows up as a hole in the density distribution.

In-situ Stern-Gerlach spin detection

The experiments of quantum magnetism presented in this thesis obtain the key information on the system from the spatial distribution measured with the in-situ single-site resolved imaging technique. With the above described method, however, it is not possible to detect and distinguish both spin states within a single image. A full detection is eligible to provide precise spin-spin and spin-density correlations and is feasible with Stern-Gerlach type spin detection. At first, it is contradictory to combine in-situ detection with Stern-Gerlach type detection because a spatial separation of the different spin states is necessary. In order to preserve the spatial information, the splitting of the two states must be transformed in such a way that a unique mapping to the original position is possible. If this separation is done along an additional direction the density distribution can be fixed along the spatial dimensions of the initial system.

We achieved this detection method within our experiment for the measurements in Chapter 4.2 to uniquely identify both spin states as well as empty lattice sites. Here, we started with an isolated single 1D system by removing all atoms but a single line in the x-direction. Thereafter, the time evolution is performed in exactly the same way as was done for the other experimental runs using the imaging techniques optically removing one of the two spin components. For the Spin-Gerlach type imaging, the dynamical evolution is stopped first by ramping up all lattices and consecutively the spins are spatially separated along the y-direction, orthogonal to the 1D system. For this purpose, the lattice along the y-direction is lowered while a magnetic field gradient is applied along the y-direction as well. The involved hyperfine states feel a force in opposite directions as their magnetic moments have opposite sign. After the magnetic field gradient is increased close to the maximum, the y-lattice is switched on again and the cloud is imaged with the standard fluorescence technique (see Chapter 3.3.1). The total sequence is illustrated in Figure 3.5.

At the end of this protocol, where the image is taken, the position of the spins is encoded in the x-direction while the spin state is encoded in the y-direction. Here, the atoms in the $|\downarrow\rangle$ state are closer to the initial 1D system than the atoms in the $|\uparrow\rangle$ state because the magnitude of the magnetic moment is half as big. Figure 3.6 shows a typical example of a prepared 1D tube and the performed in-situ Stern-Gerlach spin detection. The summed distribution of all measurements along the x-direction clearly shows that both spin states are well separated and can be clearly identified as either $|\downarrow\rangle$ or $|\uparrow\rangle$.

This method can be be extended to several 1D systems in a double well structure along the y-direction where the spin state would be mapped to the two position in the double well [27]. For a 2D system a separation along the z

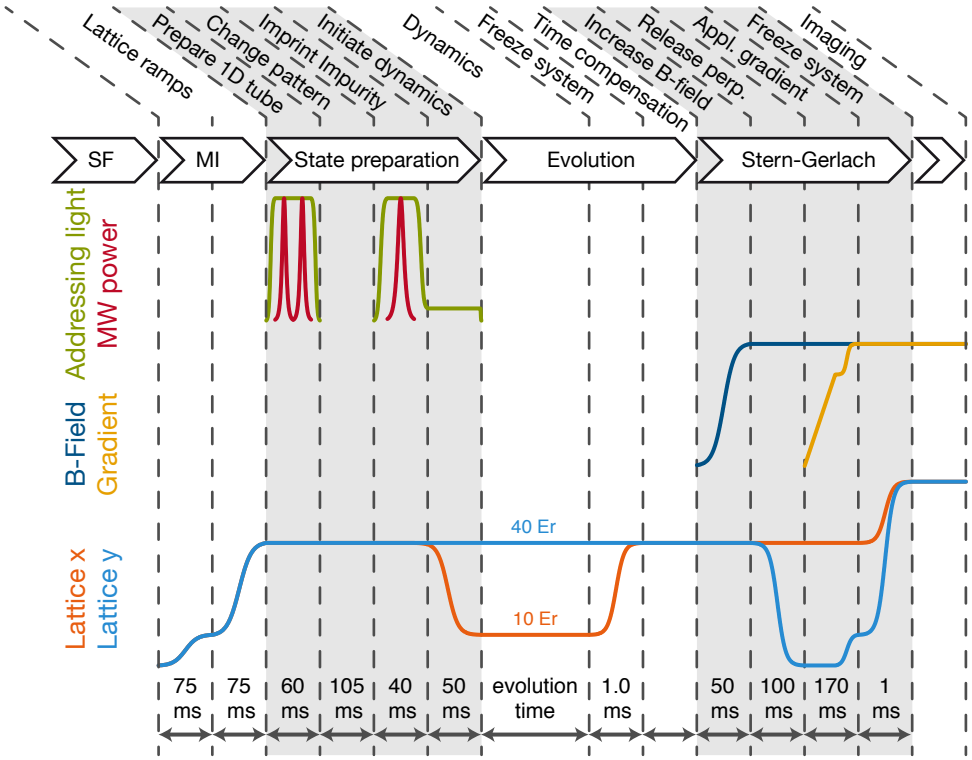

Figure 3.5: Stern-Gerlach sequence. The phase transition between the SF and MI phase is crossed by a double s-shaped lattice ramp. Thereafter a single 1D tube along the x-axis is cut out of the MI and with a second addressing pulse, a spin impurity is imprinted at the center. While the x-lattice is lowered to increase the tunneling rate, the impurity is pinned down with the addressing light, reduced in amplitude. The dynamics start after a sudden ramp down of the addressing light and is stopped after variable hold time by increasing that x-lattice to $40\,E_r$. A second time slot with variable length is used to compensate for the duration of the dynamics to keep the total time of the sequence constant. There after the different spin states are split in a Stern-Gerlach like method in the y-direction. Therefore, the y-lattice is lowered for a short time scale while a magnetic field gradient, creating opposite forces for both spin states, is applied. This sequence is optimized to reach a clear separation between both spin states and allow for the detection of the local occupation of the 1D system. The positions of the atoms is determined with fluorescence imaging at the end of the sequence.

direction is feasible but so far it has been challenging to image the two clouds separated in z-direction with high fidelity.

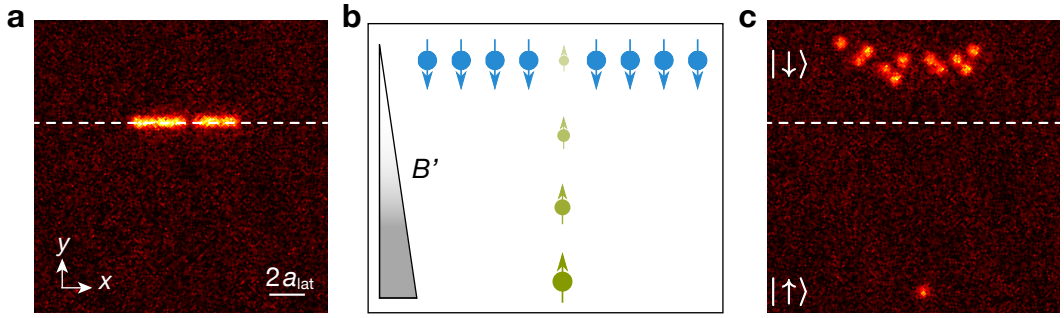

Figure 3.6: in-situ Stern-Gerlach. **a**, single 1D tube. A single atom in the spin-↑ state is removed with the standard spin resolved detections and shows up as a hole. **b**, a magnetic field gradient perpendicular to the orientation of the 1D system separates the two spin components in a Stern-Gerlach like approach **c**, after the spatial separation along the y axis, the spin state is encoded into the position along y while the original position information along x is conserved.

3.3.4 Detection of higher moments

Following the interpretation of Heisenberg [131], a measurement of a quantum mechanical system is a projection of the wave function describing the total system to the measurement basis. The probability p_i to detect an atom on site i is obtained from multiple site resolved measurements of the same quantum state and is the expectation value of the number operator $\langle \hat{n}_i \rangle$ up to parity projection. Here $\langle \cdot \rangle$ represents the ensemble average over different experimental realizations. The amplitude of the wave function amplitude is recovered after repeating this measurement many times.

Correlations

Two site correlations are the first higher order which can be extracted from density measurements. Additionally to the application within this thesis, correlation in single-site experiments led to the detection of the light-cone-like spreading after a quench [14] and the ferromagnetic spin state in fermionic system [27–29]. The collected data of the site resolved images contains as well the joint probability $p_{i,j}$ to detect one atom at site i and j in the same measurement, respectively. Due to the parity projection, the outcome of each measurement on a single site is limited to 1 and 0, which allows us to rewrite $p_{i,j} = \langle \hat{n}_i \hat{n}_j \rangle$. The data contains even joint probabilities involving more lattice sites but here, we focus on point correlators.

The correlation signal can be normalized to the single particle probability

p_i which is for example done by the g_2-function:

$$g_2(i,j) = \frac{p_{j,i}}{p_j p_i} \tag{3.7}$$

This is an experimentally useful observable given that the densities p_j and p_i are not too small. Otherwise very good statistics on the probabilities are necessary, because otherwise the g_2 would have a large relative uncertainty due to the devision. If the correlation signal is expected to depend only on the distance d between both positions and is otherwise equal on the total system, the correlation function can be averaged over N different positions:

$$g_2(d) = N \sum_j \frac{p_j p_{j+d}}{\left(\sum_j p_j\right)^2} . \tag{3.8}$$

This observable was for example measured for the far-from equilibrium spin transport to determine the amplitude of the imprinted spin spiral state which did not have a fixed phase (see Chapter 5). In this case, the g_2 function is evaluated for the local probability to be in the $|\downarrow\rangle$ state.

Alternatively, it is also possible to subtract the uncorrelated part and one gets a different and often used definition of correlation. This is similar to the definition of the covariance and is often called connected correlation function:

$$C_{i,j} = p_{j,i} - \left(p_j p_i\right) . \tag{3.9}$$

This function can also be reduced to use the distance d as the only parameter if the result is expected to have the same correlations everywhere:

$$\begin{aligned} C_d &= \sum_i C_{i,i+d} \\ &= \sum_i p_{i,i+d} - \sum_i p_i p_{i+d} . \end{aligned} \tag{3.10}$$

3.3.5 Entanglement detection

Quantum many-body systems are distinct from their classical counterparts due to entanglement among their constituents [132, 133]. Especially in strongly correlated regimes, such as in the vicinity of quantum phase transitions [132, 134] or far away from equilibrium [135], entanglement is important. The growth of entanglement with time or subsystem size seriously limits numerical simulations of complex quantum systems [133]. Next to its importance on this fundamental level, entanglement is a valuable resource for quantum information and its microscopic control is required for applications going

beyond classical measurements [136]. Experimentally, the measurement of entanglement is difficult given that full quantum state tomography requires extraordinary control. Hence, a direct detection is only feasible in small systems [73, 137, 138]. In larger or more complex many-body systems, the presence of entanglement can be just inferred from macroscopic observables, often relying on entanglement witnesses [132, 139]. Such detection procedures have been applied for susceptibility measurements in solids [140], collective spin systems [141–146] and coupled superconducting qubits [147].

Detection of correlations in a single basis is not sufficient to imply entanglement. This is clear from the Bell inequality as it is only violated by entangled states but not by classical states which have correlations in a single measurement basis. The violation of the Bell inequality has been applied to photons and recently a completely loop hole free measurement was performed [148], also a measurement of entanglement. The amount of entanglement can be calculated from the full density matrix. This has been done for example for atoms coupled to a cavity [149, 150]. Full control over the rotation of each individual spin is needed for this method and the reconstruction of the density matrix for a two site system already needs $2^{2\cot 2}$ measurements. The scalability of this measurement with system size is very bad as already a 8 spin system needs $8^{2\cot 2}$ measurements as shown for an ion chain [151]. Thus extracting entanglement from the full density matrix can be very challenging, but certain better accessible lower bounds for entanglement exist [152]. For bipartite entanglement such a lower bound is given by the concurrence

$$C_{i,j} = 2\max\left(0, p_{\uparrow\uparrow} - \sqrt{p_{\uparrow\downarrow}p_{\downarrow\uparrow}}, p_{\uparrow\downarrow} - \sqrt{p_{\uparrow\uparrow}p_{\downarrow\downarrow}}\right) . \tag{3.11}$$

Following a recent proposal [153], a lower bound for the concurrence is accessible without local spin control, relying only on global spin rotations and measures the right part of the above equation. The concurrence quantifies entanglement on a scale between zero (no entanglement) and one (maximal entanglement). A convenient lower bound is given by

$$\mathcal{C}_{i,j} = 2\left(2\langle \hat{S}_i^{\perp}\hat{S}_j^{\perp}\rangle - \sqrt{P_{i,j}^{\uparrow,\uparrow}P_{i,j}^{\downarrow,\downarrow}}\right) . \tag{3.12}$$

The first term measures transverse ($\perp$) spin correlations as the mean of the correlations along x- and y-direction:

$$\begin{aligned}\langle \hat{S}_i^{\perp}\hat{S}_j^{\perp}\rangle =& \frac{1}{2\pi}\int_0^{2\pi}\left(\cos(\alpha)S_i^x + \sin(\alpha)S_i^y\right)\left(\cos(\alpha)S_j^x + \sin(\alpha)S_j^y\right)d\alpha \\ =& \frac{\langle \hat{S}_i^x\hat{S}_j^x\rangle + \langle \hat{S}_i^y\hat{S}_j^y\rangle}{2} .\end{aligned} \tag{3.13}$$

The second term of Equation 3.12 takes into account longitudinal spin correlations, where $P_{i,j}^{\alpha,\alpha}$ is the joint probability to find atoms at position i and j in the same spin state $\alpha \in (\downarrow, \uparrow)$ measured along the z direction. For an ideally prepared system with initially only a single $|\uparrow\rangle$ impurity, as introduced in Chapter 2.2.1, the second product term is zero as two atoms in the $|\uparrow\rangle$ will not be observed. This measurement is special, because it extracts information about the quantum state which proves that the state has a non classical wave function.

3.4 Magnetic field control

Magnetic fields are an important tool in the control of cold atoms. During the initial cooling with a magneto-optical trap, magnetic fields are essential to get a spatially depended force and in the second step of the experimental sequence, atoms are evaporated in a pure magnetic trap. These are both standard techniques to obtain a degenerate gas. For the preparation of a single two-dimensional layer a strong magnetic field gradient along the z-direction is deployed to selectively remove atoms in all but one anti-node of a standing wave formed by a 1064 nm laser. During the sequence, the orientation of the spin is determined by magnetic fields, hence, the polarization of crucial laser beams, like repumper light and resonant state selective removal light, has to agree with the direction of the magnetic field. At the end of the sequence, the absolute magnetic field should be very close to zero in order for the molasses cooling during imaging to work best.

All processes mentioned above require excellent control of the magnetic field. We create the required magnetic fields at the position of the the three dimensional lattice with three pairs of coils and an additional single coil. The three coil pairs are in good approximation arranged in Helmholtz configuration and thus each pair produces a homogeneous magnetic field along the common coil axis at the position of the atomic cloud. One pair is aligned along the z-axis and the other two pairs are aligned on the diagonals of the x and y lattices to have full control over the magnetic field in all three spatial directions. The unpaired additional single coil is located on top of the chamber and is aligned on the z-axis. It produces the magnetic field gradient along this axis for the single 2D plane preparation (details can be found in [101]).

3.4.1 Energy shift with magnetic fields

Within this thesis, magnetic fields with a maximal amplitude of 60 G were applied. The shift of the energy levels of Rubidium 87 in the $5^2S_{1/2}$ ground state

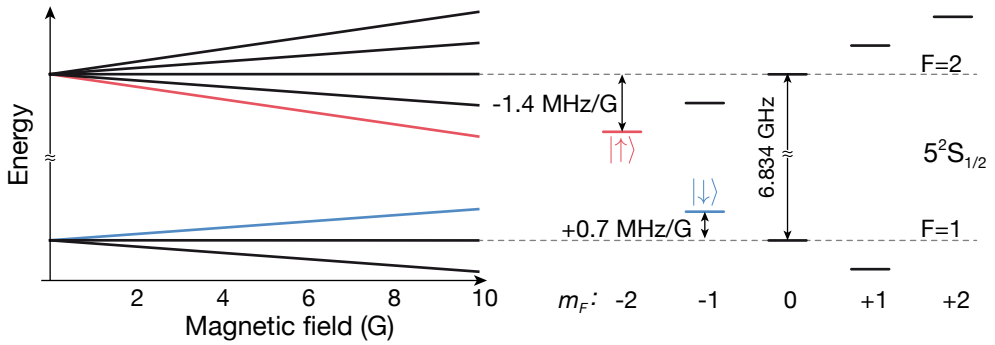

Figure 3.7: Hyperfine level shifts. Shifts as a function of the magnetic field for all Rubidium 87 ground state ($5^2S_{1/2}$) levels. Within this thesis the two hyperfine levels marked in red and green are used and represent a pseudo spin-1/2 system.

is well described by the Breit-Rabi formula which is valid in the low field Zeeman limit as well as in the Paschen-Back limit and thus covers the full necessary range for the experiments. The shift of the three $F = 1$ and the five $F = 2$ states due to a magnetic field are shown in Figure 3.7. Typically, already magnetic fields of a few Gauss are sufficient to split the states strong enough such that individual transitions are resolved with the microwave radiation. For strong magnetic fields the quadratic shift can be detected and the magnetic field amplitude is exactly calibrated by measuring the resonance frequencies of any two transitions. 3.23 G is a special magnetic field strength, because the Zeeman shift of the clock transition $|F = 1, m_F = -1\rangle$ to $|F = 2, m_F = 1\rangle$ has a quadratic minimum [154]. With additional current stabilization circuits, we ensured that the magnetic field stability is in the order of 1 mG. This leads to a fluctuation of approximately 2 kHz for the typical $|\uparrow\rangle \leftrightarrow |\downarrow\rangle$ transition and a coherence time in the order of 1 ms. These residual fluctuations are probably due to fluctuations of the magnetic background field. Further reduction of the magnetic field noise is significantly more difficult and active feedback on the magnetic field or better shielding, for example with mu-metal, is necessary.

3.4.2 Elimination of magnetic field gradients

Global microwave transitions require that the spatial variation of the magnetic field is much smaller than the total magnetic field. Under this condition, all atoms can be transferred with high fidelity employing a single global microwave sweep. This puts only a very weak constrain on the magnetic field gradients since the system size is in the order of 10 µm and the absolute magnetic field can be several Gauss strong. However for the experiments in

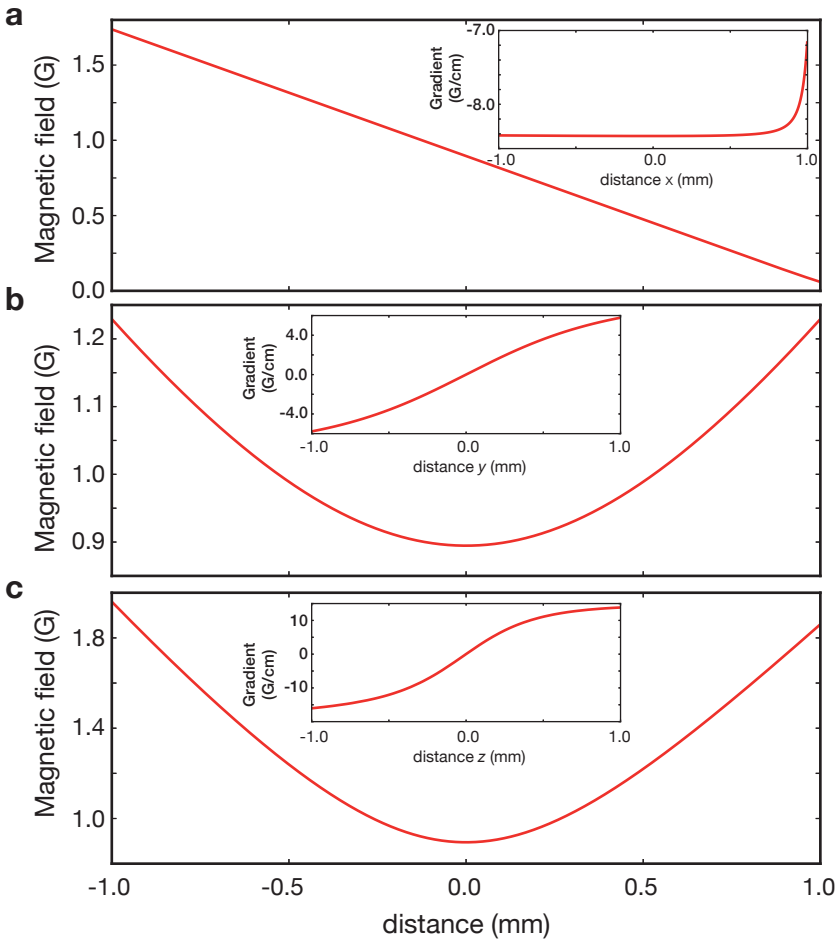

Figure 3.8: Magnetic field configuration. Absolute value of the magnetic field as a function of x, y and z-position and the corresponding derivative in **a**, **b**, and **c** respectively. The magnetic field changes linear along the x-axis around the position of the atoms ($x = y = z = 0$), generating a constant gradient along this axis. The two other axes have a quadratic minimum and thus vanishing gradient at the center. In the given configuration, the gradient increases faster along the z-axis.

Chapter 4.2 and 5 it is crucial that the magnetic field gradients within the xy-plane are much smaller. For these experiments, where the relative in-plane phase of the effective spins is measured, gradients should actually be below the experimental resolution. Gradients can be canceled much better than the stability of the field amplitude because typical noise sources create large scale fluctuations which are common for all atoms within the comparable small total size of the ultracold atom cloud (order of 10 µm). Sources of magnetic field gradients can be imperfect Helmholtz configurations of the coil pairs,

misplaced axis of the coils and external magnetic fields, for example coming from ion getter pumps. The magnetic field gradients are measured with a Ramsey-like sequence in the decoupled MI regime and thus non-interacting atoms. The presence of strong gradients is detected by automatic formation of spin spiral structures, where the final probability to detect an atom in the $|\downarrow\rangle$ state after a Ramsey sequence with hold time t and detuning δ is given by:

$$\begin{aligned} P(\boldsymbol{r}) &= \cos\left((g \cdot B(\boldsymbol{r}) - \delta)t\right) \\ &\approx \cos\left((g \cdot B(\boldsymbol{r}_0) - \delta)t + g \cdot \nabla B(\boldsymbol{r})(\boldsymbol{r} - \boldsymbol{r}_0)t\right) . \end{aligned} \tag{3.14}$$

In this formula, g is the magnetic sensitivity of the transition, which is approximately 2.1 kHz/G for the standard $|\downarrow\rangle \leftrightarrow |\uparrow\rangle$ transition. Note that here $\boldsymbol{r}$ dispalys the direction vector in the xy-plane and $\boldsymbol{r}_0$ is an arbitrarily chosen reference point within this plane. The total magnetic field $B(\boldsymbol{r}_0)$ can be compensated up to fluctuations by the detuning of the microwave pulses and only changes the phase of the global spin spiral. This method provides a measure of the absolute gradient strength as well as the direction but not the sign of the gradient which needs to be tested.

The control of the gradient strength with the available magnetic field coils can be best understood for the ideal case without additional background gradient and an ideal Helmholtz configuration for all coils. With the coil pair along the z-axis and the gradient coil, the magnetic zero point is located on the z axis and can be moved by changing the current in the pairs of coils while the gradient strength is controlled by the gradient coil. In a xy-plane away from the zero point, the magnetic field has a quadratic minimum along the z axis but changes linearly far away from the center. Thus, for the ideal toy configuration, the magnetic zero point should be centered above or below the atomic cloud. As it is difficult to move the position of the atomic cloud, it is necessary to move the zero point, which can be easily done with the two additional coil pairs with their axis in the xy-plane. A typical configuration is shown in Figure 3.8. This method is still applicable if external gradients are present. For the mentioned experiments, the gradient was iteratively compensated to below 2 mG/cm which corresponds to an total phase difference across the cloud of $\phi < 2\pi\, 2\,\mathrm{Hz}\, t/20a_{\mathrm{lat}}$ for the employed hyperfine states. Here t represents the total hold time.

3.5 Single-site addressing

Besides the local detection of density and correlations, the high resolution microscope provides a method to manipulate atomic clouds on the level of a sin-

gle lattice site. This is an essential technique to prepare our well controlled excited initial states. The precise manipulation of our initially homogeneously filled MI states enables us to shape the density [15, 98, 99] or prepare structured spin 1/2 systems [155–157]. The high resolution manipulation is based on local light shifts which are spectroscopically resolved by microwave transfers. The first realization in our experiment was done with a single focused laser beam. Although the full-width at half-maximum (FWHM) beam diameter was 600 nm, a resolution of 300 nm (FWHM) was obtained. The concept of the combined light shift and microwave transfer and its implementation with a single focused beam is described in detail in [100] and it was used to study the expansion of a single atom in a lattice [15]. In this scheme, a σ^--polarized, off-resonant laser beam at 787.65 nm wavelength focused on the selected lattice site results in a negative energy shift (attractive potential) only for the $|\uparrow\rangle$ state while leaving the initial spin $|\downarrow\rangle$ state almost unaffected. A microwave pulse, that is resonant with the shifted atomic transition, then produced the spin-flip from $|\downarrow\rangle$ to $|\uparrow\rangle$.

Here, I will describe a similar method employing a spatial light modulator to create arbitrary light patterns which are imaged onto the atoms to perform a parallel preparation of all atoms instead of the first serial approach. This procedure was used for local state manipulation in all experiments described within this thesis. The setup was implemented during a diploma project [158].

3.5.1 Experimental setup

In order to induce only a local transfer between the two relevant hyperfine levels ($|\downarrow\rangle$ and $|\uparrow\rangle$) a spatial selection has to be made. Previously this selection was realized with a focused beam steered with a piezo-controlled mirror. This method had excellent spatial resolution but the preparation time scaled linearly with the number of necessary spin flips. This can be overcome if a global light pattern is sent at the same time to all desired lattice sites. We chose to create the necessary light patterns with a digital mirror device (DMD), in this specific case: *Texas Instruments DLP Discovery 4100*. This device has 1024×768 mirrors with a pitch of 13.68 µm which can be individually turned to an on or off position. The refresh rate is specified with 32.550 Hz and allows for very fast changes of the displayed patterns. At the same time, a chosen pattern can be displayed for arbitrary long times and does not require any refresh as typically necessary for liquid crystal phase modulators. The liquid crystal phase modulators are an other possible alternative and they have been used in Fourier plane to create controllable potentials [159, 160]. Our DMD is illuminated with a large Gaussian beam to

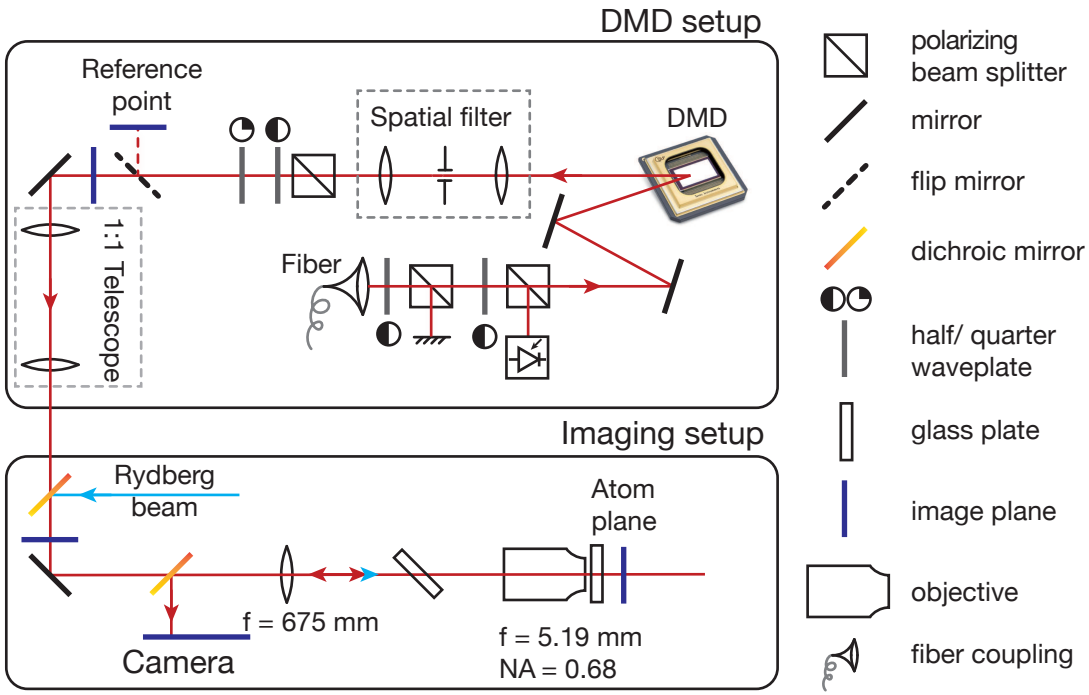

Figure 3.9: Addressing setup. The light is guided to the experimental setup in an optical fiber (center of the upper box). A fixed fraction of the beam is sent to a photo diode for intensity stabilization. The illumination of the digital mirror device (DMD) is followed by a spatial filter within a 150:100 telescope. The light patterns can be analyzed by a CCD camera at a reference point given by an image plane. A second 1:1 telescope images the DMD pattern from the first image plane to the second image plane in the imaging setup section. There the addressing beam is overlapped with a uv laser beam for Rydberg excitations and the imaging light propagating in opposite direction is separated for the camera with two dichroic mirrors. The last imaging step consisting of a two inch lens and the microscope with high numerical aperture (lower box, right). In this step, the image created with the DMD is demagnified and focussed into the atom plane.

map the preferred pattern of the DMD to the light field. Thereafter high spatial Fourier components are filtered out with an effectively 4 f imaging setup and an iris with variable size placed in the Fourier plane between both lenses. The first lens of the 4 f setup has a focal length of 150 mm while the second focal length is 100 mm resulting in a demagnification of the pattern. Two lenses with a focal length of 250 mm each, create a 1:1 telescope producing an image plane at the position of the camera of the high resolution objective. In between, the light from the DMD is overlapped with a blue laser at 480 nm for two photon Rydberg excitations [97–99] with a dichroic mirror. The sep-

aration from the light for the fluorescence imaging is also performed with a dichroic mirror. The last telescope consisting of a $f = 675\,\mathrm{mm}$ lens and the high resolution objective with an effective focal length of $f = 5.19\,\mathrm{mm}$ images the pattern on to the atoms. The total imaging system has a magnification of 130 which results in mapping approximately 7×7 mirrors of the DMD to one lattice site. Figure 3.9 displays a schematic of the DMD setup.

3.5.2 Pattern generation

The DMD cannot directly create gray scales, as the mirrors only allow on-off amplitude control. These gray scale values are necessary to compensate the inhomogeneities of the Gaussian beam illuminating the DMD to create flat potentials and to create controlled locally varying light fields. With a flip mirror a camera is placed on demand at the position of the second image plane to analyze the created light patterns. At this image plane, we measure a reference profile of the incident Gaussian beam with all mirrors of the DMD in the binary *on* position to calibrate the incident light field intensity $I_g(i)$.

The necessary reflectivity $r(i)$ of the DMD to obtain the target light field $I_t(i)$ at mirror position i is calculated with the intensity of this incident light field $I_g(i)$ and is naively given by:

$$r(i) = \frac{I_g(i)}{I_t(i)}\,. \tag{3.15}$$

As the reflectivity is modeled by an error diffusion algorithm and thereafter high spatial frequencies are filtered out, the actual intensity at the image plane is not modified with actual reflectivity but the reflectivity squared.

$$r_{ED}(i) = r(i)^2 = \left(\frac{I_g(i)}{I_t(i)}\right)^2\,. \tag{3.16}$$

This is caused by the non-linear Fourier filtering and assumes that the high spatial frequency scattering peaks generated by the small and equally spaced mirror array are all filtered out and hence leads to intensity loss. This effect is strongest for a reflectivity of 50 % where every second mirror is flipped. Obviously the reflectivity is not changed for both extrema (zero and one) as these require a homogeneous DMD configuration with all mirrors in the same position. The actual dependence can be calculated with Fourier analysis [161].

3.5.3 Calibration

In depth studies of the generated light field patterns were performed by David Bellem [158]. For these experiments, a CCD camera was used to determine the intensity distributions directly after the pinhole cleaning in the

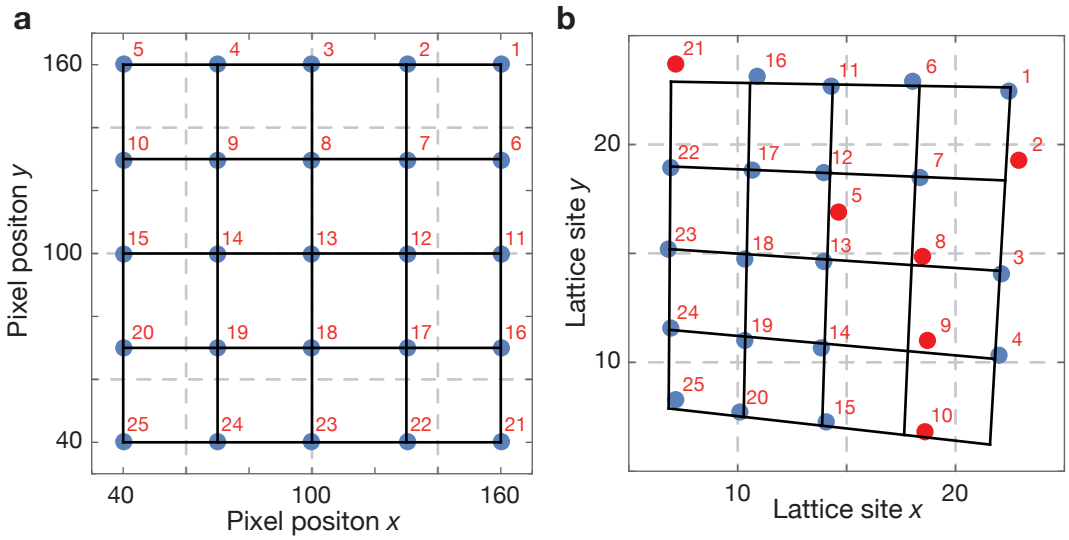

Figure 3.10: Addressing image transformation. 25 points on the DMD where selected on a regular grid (**a**) and their corresponding position on the lattice sites was measured (**b**). All blue points where used to calculate the affine transformation and the red points were disregarded. The black grid was transformed with the obtained transformation function.

second image plane and with an extra test objective. This test showed superior flatness of RMS noise below 2 % and edge sharpness of 56 µm. However, no direct measurement at the position of the atoms after the total optical beam path is possible with a CCD camera as one would need to remove the vacuum chamber. Thus, the pattern was optimized at the monitoring port right after the pinhole cleaning. This method worked fine but caused problems during the first experiments with projected disorder potentials created with the spatial light modulator. During these experiments it was noticed that the created potential were not flat but included large scale gradients. These structures were attributed to several imperfect optical components, especially the dichroic mirrors, which distorted the light patterns. Thus we developed an in-situ amplitude calibration of the desired patterns.

At first we determined the exact mapping between the DMD and the atom plane. This mapping was obtained by loading atoms successively into several small box-shaped light fields created by the addressing light, located in an equally spaced array (Figure 3.10). We averaged the atom distribution over typically 3 repetitions for each box position and extracted the center of the atomic distribution with a two-dimensional Gaussian fit. Knowing the position at the DMD and at the lattice, an affine transformation connecting the initial position with the position at the atomic cloud is obtained. The in-

verse transformation is used to map the deviations from the mean value of the box potential to the coordinate system of the DMD (see Figure 3.10 for the reconstructed transformation).

We started the in-situ potential calibration by preparing spin polarized, preferably large MIs in the $|\downarrow\rangle$ state. The lattice depth was increased above $20\,E_r$ to suppress all dynamics. A very fine stepped microwave resonance scan over the shifted transition to the $|\uparrow\rangle$ state was taken. We increased the power of the desired light pattern to maximum in order to maximize the sensitivity. The resolution of these microwave scans was down to a 1 kHz which is limited by shot to shot magnetic field fluctuations on the order of 1 mG. This resolution is typically enough as the total light shift is up to 60 kHz. The measurement can be performed without cold MIs because the resonance positions are determined by deviations from the mean density.

To improve the addressing pattern, the flatness of a uniform box was measured with the atoms. The initial distribution had deviations of more than 20 % from the mean value. The pattern of deviations is used to correct the reference pattern with the known affine transformation. This transformed pattern was multiplied to the original correction pattern. We repeated the measurement of the box potential and the correction procedure several times and found out that an improvement was obtained for up to 4 repetitions for which residual fluctuations below 5 % were reached (see Figure 3.11 for example images taken before and after correction). It was verified that the improvement remains valid over several weeks, as long as the imaging path is not strongly modified. Nonetheless, it should be noted that the mapping of the coordinate systems is much more fragile and does not remain valid.

In principle, the same method can be applied to directly detect the beam profile for a totally reflecting DMD producing a reference profile. For this procedure, the intensity variation over the DMD due to the Gaussian shaped illuminating beam is so large that a much bigger range of the spectrum needs to be scanned with the MW transition. However this is difficult at the same high resolution, because the previous method already needed ten repetitions with 21 different frequencies each. During the whole calibration measurement (approximately 100 min) drifts of the magnetic field need to be below 1 mG because otherwise the spectrum broadens.

3.5.4 Disorder potential

The single-site addressing technique requires homogeneous light patterns which can be locally turned on or off. This light pattern should be flat to create a homogeneous light shift of the transition between the two hyperfine states. Additionally light patterns can be used to create potentials which are

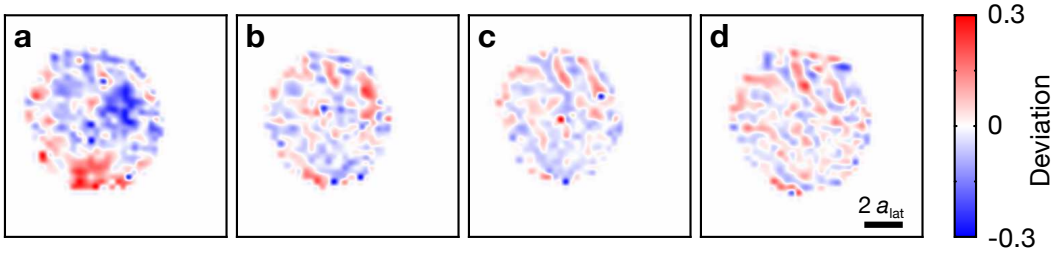

Figure 3.11: Addressing amplitude deviation. a, deviations of the light shift from the mean value with the correction pattern taken from the reference camera. The light shift is calibrated with in-situ microwave spectroscopy. These deviations are used to improve the amplitude correction pattern. **d**, at the fourth round of correction the deviations are much smaller and homogeneously distributed. **b,c** show intermediate images.

applied during dynamical evolutions of the density distribution at a lower lattice depth. The many-body localization experiments required a local on-site disorder potential which we desired to create with the DMD device. Therefore we implemented the ability to create light patterns with random amplitude for each lattice site.

The spectroscopically in-situ imaging of the light field was applied to fixed random disorder potentials to characterize these patterns. We measured the probability distribution of the amplitudes and extracted the two point correlation function. The extracted amplitude distribution has the shape of a normal distribution and correlations decay exponentially with a correlation length of $0.6\,a_{\mathrm{lat}}$. This is compatible with the resolution of the objective which is of the same order of magnitude as the lattice spacing. The point spread function of single atoms in fluorescence imaging is limited by the same objective and has a standard deviation of $0.501(1)\,\mathrm{a_{lat}}$ [102]. Convolution of a random potential and a two-dimensional normal distribution of same width reproduces the measured correlations and the amplitude distribution well. Hence we conclude that resolution for the addressing light is limited by the objective as well.

3.5.5 Further options with high resolution objectives

A clear illustration of the capabilities of a DMD for potential generation was published recently [162] and high precision potentials were created [163]. Beyond that, a high resolution access to the atomic plane opens up many options to control the atoms. For example, recent experiment have utilized a high resolution imaging setup to implement a lattice with flexible periodicity [22]. Here, two beams parallel to the optical axis of the imaging system,

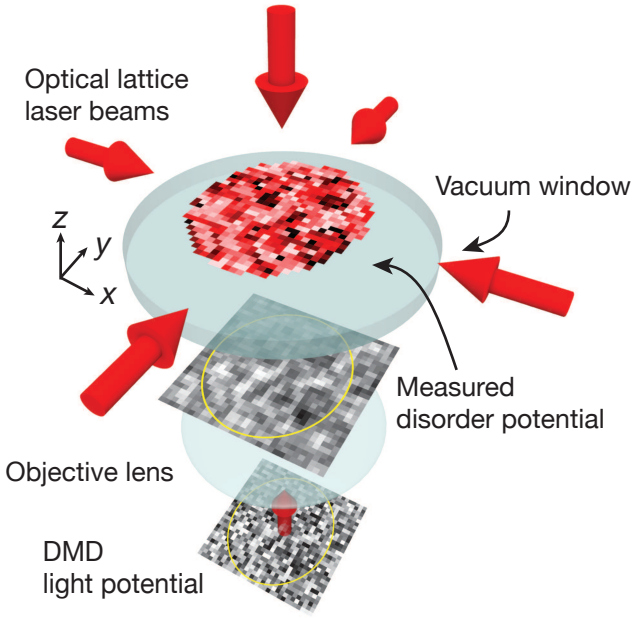

Figure 3.12: Projected disorder potential. A two-dimensional random disorder potential is imaged onto a single atomic plane in an optical lattice. The disorder is controlled by a digital mirror device (DMD), which converts a gaussian laser intensity profile into a two-dimensional random intensity distribution with spatially uniform average light intensity (bottom image). The limited numerical aperture (NA = 0.68) of the microscope objective introduces a finite correlation length and leads to a smoothing of the disorder distribution. The two gray scale images show the calculated original (bottom) and smoothed (middle) light intensity distributions. The top most image displays the local disorder potential determined by in-situ spectroscopy (see Section 3.5.3). The yellow circle on the lower images indicates the spectroscopically calibrated region.

symmetrically arranged around this axis, are focused to the atoms, creating an interference structure in which the spacing depends on the distance between the two beams at the entrance of the high resolution objective. This idea can be extended to build a flexible Bragg spectroscopy setup for which the relative frequency of the two interfering beams needs to be controlled additionally. This can be obtained by two acousto-optic modulators (AOMs) which have a chosen relative frequency difference. Bragg spectroscopy has also been shown with quickly moving patterns on a DMD [164].

4 Dynamics close to equilibrium

In a series of experiments we explored the coherent dynamics of a one-dimensional ultracold quantum gas initialized in a single hyperfine state $|\downarrow\rangle \equiv |F = 1, m_F = -1\rangle$ after a local transfer of a single or two atoms into the $|\uparrow\rangle \equiv |F = 2, m_F = -2\rangle$ state. First, we determined where the mapping to the Heisenberg spin model is valid, by tracking a single-spin impurity. In a second experiment, the entanglement propagation associated with the single-spin impurity dynamics are explored. The last group of experiments focuses on the dynamics of two adjacent impurities and the resulting formation of bound magnons. It should be noted that throughout this thesis the above defined notation for the spin states is used, which differs from the notation in some of the corresponding publications ([155, 156]).

4.1 Quantum dynamics of a mobile spin impurity

We started our experiments on the Heisenberg model with space- and time-resolved observation of a coherently propagating spin wave by tracking the motion of a deterministically created single-spin impurity in a one-dimensional (1D) spin chain. This is done by the preparation of a single mobile boson of type $|\uparrow\rangle$, placed in a 1D lattice with unity filling and a bath of $|\downarrow\rangle$ bosons. By varying the lattice depth, we experimentally validate if the mapping of the two-component single-band Bose-Hubbard model to the Heisenberg model is valid as predicted in Chapter 2.2.1.

4.1.1 Experimental procedure

Initially, the atoms were prepared in a spin-polarized MI state with all approximately 170 atoms in the $|\downarrow\rangle$ state. Already in preparation for the one-dimensional systems, the lattice depth along x was only $V_x = 10.0(3)\, E_\mathrm{r}$ whereas along the orthogonal axis all motion was frozen out with a lattice depth of $V_y = 30(2)\, E_\mathrm{r}$. For this configuration, the tunneling rate inside each 1D system is about 41 times larger than the hopping rate between different 1D systems. With our DMD addressing system, the central line of atoms oriented along the y-lattice was transferred to the $|\uparrow\rangle$ state to introduce a single impurity in each 1D system. Here, a fidelity of $88(5)\,\%$ is achieved for the initial

spin preparation, which was optimized to produce preferably not more than one spin impurity. The σ^--polarized light of the addressing system leaves the $|\downarrow\rangle$-state unaffected but creates an attractive potential for the $|\uparrow\rangle$-state. Thus, the atom in the $|\uparrow\rangle$-state can be pinned to its original position by leaving the addressing light on. These impurity atoms inside the bath of $|\downarrow\rangle$ atoms were released by turning off the addressing laser within a 1 ms ramp. The propagation was stopped after a variable hold time by rapidly increasing the lattice depth of all axis to $80\,E_r$ within 300 µs.

4.1.2 Detection

For detection, we used both spin resolving techniques: positive and negative spin detection as each has different advantages (see Chapter 3.3.3). The positive detection method allows for precise detection of the $|\uparrow\rangle$ impurity, but nothing about the surrounding spin $|\downarrow\rangle$ bath can be extracted. On the other hand, negative imaging reveals the parity distribution of the spin $|\downarrow\rangle$ bath. However it does not distinguish between thermal excitation in the density sector (mostly doublons and holons) and the spin impurity. Post-selecting samples with only one empty site in the central region of the spin chain allowed to filter out a lower-temperature subset of the data. The temperature always corresponds to the temperature of the bath and should not be confused with the spin temperature which cannot be measured for the out-of-equilibrium initail state. The fidelity of preparing at least a single-spin flip is high enough such that this single empty site was with very high likelihood the $|\uparrow\rangle$ spin impurity. Only if no spin impurity was created a single thermal excitation is mistaken as the spin impurity. We reconstruct each probability density distribution at a certain hold time by averaging over several experimental repetitions and averaging over the central 10-14 lattice sites. The second averaging is crucial as only this step permits to take measurements for several different configurations of lattice depth and evolution time due to the massive speedup.

4.1.3 Spin impurity time evolution

The time evolution deep in the MI regime was first studied with negative imaging and postselection on a single impurity. Two outward propagating visible maxima with a minimum in-between reveals the quantum interference only possible for coherent evolution. The relevant time scale for the motion is clearly slower than expected for single particles or non-interacting atoms ($\hbar/J = 4\,\text{ms}$) [10]. The measured probability distribution after 40 ms has two symmetric peaks approximately $1.5\,a_{lat}$ away from the initial cen-

tral position. We made use of the analytical solution of the propagation of a spin impurity in the homogeneous Heisenberg model, which is given by the Bessel function $\mathcal{J}_i$ of first kind as derived in more detail in Chapter 2.2.1. For the coherent propagation, the probability distribution at time t, j sites away from the initial position of the spin impurity, is given by

$$P_j(t) = \left[\mathcal{J}_j\left(\frac{J_{\mathrm{ex}}t}{\hbar}\right)\right]^2 . \tag{4.1}$$

A single fit to all four probability distributions measured at different hold times with the superexchange coupling J_{ex} as the only free parameter yields $J_{\mathrm{ex}}/\hbar = 65(1)$ Hz. The *ab initio* band-structure calculation (see Chapter 3.2.2), using the independently measured lattice depths result in $J_{\mathrm{ex}}/\hbar = 51(^{+11}_{-8})$ Hz, close to the measured superexchange rate. The spin exchange rate increases to $J_{\mathrm{ex}}/\hbar = 61$ Hz, much closer to the measured value, including the density correction mentioned in Chapter 3.2.2. This calculation assumes a density of one in the initial and final lattice site.

4.1.4 Temperature effects deep in the MI regime

Using positive imaging, we directly observed the impurity position but in the finite-temperature bath of $|\downarrow\rangle$ atoms. The distribution of the positive imaging has almost the same width but less contrast compared to the distribution from the post-selected negative images. This suggests that fast moving excitations in the bath decohere the motion of the impurity as they produce random phase slips. This reduces the contrast but does not change the speed significantly as the position of the spin impurity is at most shifted by one lattice site. This effect is quantitatively studied by numerical simulations of the Heisenberg model using the time-dependent density-matrix renormalization group (t-DMRG) algorithm for finite temperature [165–169]. Therefore, the contrast and propagation speed for different temperatures $T = 0 - 0.2\,U/k_B$ are evaluated. The contrast is defined as

$$C = (P_{\mathrm{max}} - P_{\mathrm{min}})/(P_{\mathrm{max}} + P_{\mathrm{min}}), \tag{4.2}$$

where P_{max} is the peak value at a position which is not the initial position and P_{min} denotes the minimum in the center region between the peaks. The contrast is defined as $C = 0$ if there is no other maximum except for the central peak. The contrast for the perfect zero temperature Heisenberg model at a hold time of 40 ms is 0.7 and decreases quickly for higher temperatures reaching a value of 0.06 at $T = 0.2\,U/k_B$. The simulation produces the same contrast as obtained from the positive imaging for a temperature of

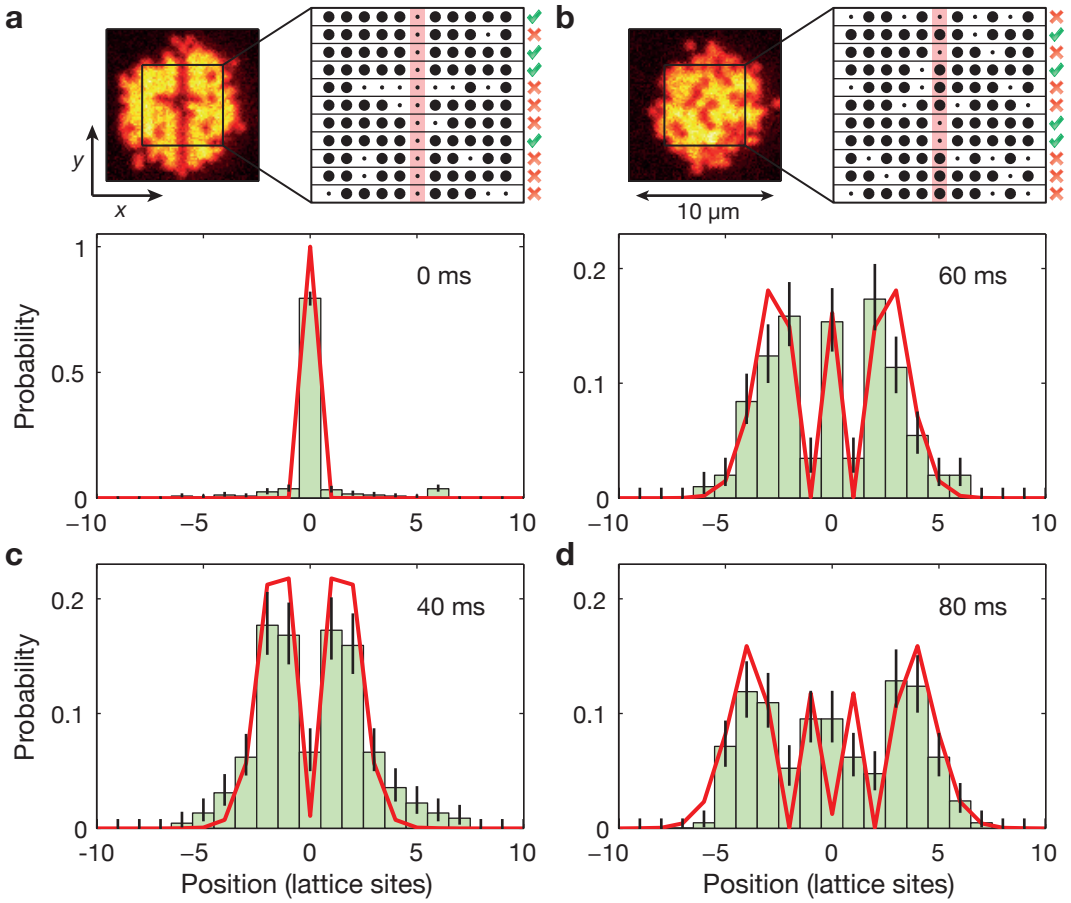

Figure 4.1: Dynamics of a mobile spin impurity. The top panels in **a** and **b** show example fluorescence images of the atoms (left) taken with the *negative* imaging technique together with the reconstructed atom distribution in the central region (right). The 1D systems are oriented horizontally. The red vertical stripe denotes the initial position of the spin impurity (detected as an empty lattice site). For the generation of an effective low-temperature subset, only the samples containing exactly one empty site were kept (green tick marks), while those containing more than one empty site were discarded (red crosses). The histograms in **a**–**d** show the position distribution of the spin impurity after different hold times for $J/U = 0.053$. Each histogram is obtained from an average over 200-250 1D systems. The error bars denote the 1σ statistical uncertainty. The red line is a simultaneous fit to all four distributions with the analytic solution of the Heisenberg model of equation (4.1), yielding $J_{\mathrm{ex}}/\hbar = 65(1)$ Hz.

$T = 0.15\,U/k_B$ for the spin bath. This is consistent with the MI temperature of $T = 0.14(3)\,U/k_B$ measured from the density distributions (see Chapter 3.3.2

for details). The contrast of the negative imaging technique is lower than expected for zero temperature and fits to a temperature of $T = 0.11\,U/k_B$. The simulation does not account for the finite spin preparation fidelity. Hence an empty lattice site in an otherwise filled tube might be accidentally identified as originally $|\uparrow\rangle$ atom although the site was already empty before the selective spin removal.

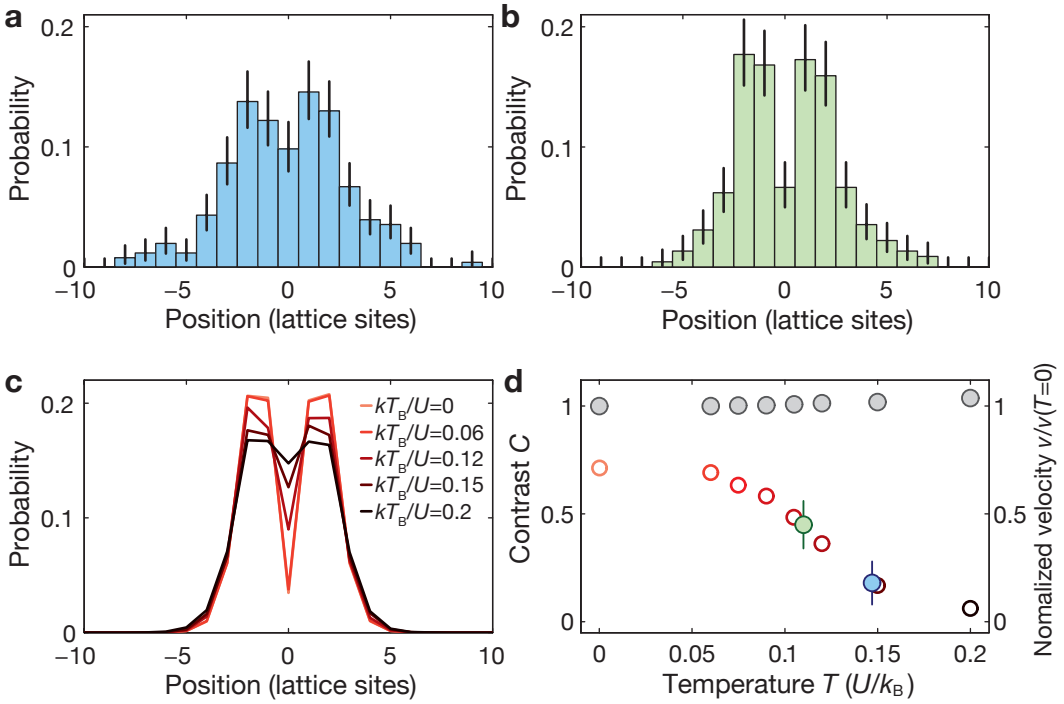

Figure 4.2: Effect of thermal excitations on the coherent spin dynamics. Shown are position distributions of the spin impurity for $J/U = 0.053$ and a hold time of 40 ms, **a** generated from positive images (blue bars) and **b** after post-selection from negative images containing one empty site in the chain (green bars). **c**, Position distributions from t-DMRG simulations for different temperatures of the bath. **d**, Contrast of the simulated distributions (open circles) and propagation velocity (gray filled circles) as a function of the temperature T. The blue and green filled circles show the contrast extracted from the experimental data of **a** and **b**, respectively. Error bars denote the 1σ uncertainty.

4.1.5 Propagation velocity

A natural way to introduce a velocity is to replace $J_{\mathrm{ex}}/\hbar$ by v/a_{lat} in the fit of the Bessel function. Numerical simulations reveal that this velocity is very

robust with respect to temperature of the bath. It is extracted from the corresponding density distribution by a fitting function (see Equation 4.1) to the simulated data and the velocity changes within the simulated temperature range by only 4 %. The experimental data support this observation because the results of both imaging techniques show consistent velocities even though their effective temperature differs.

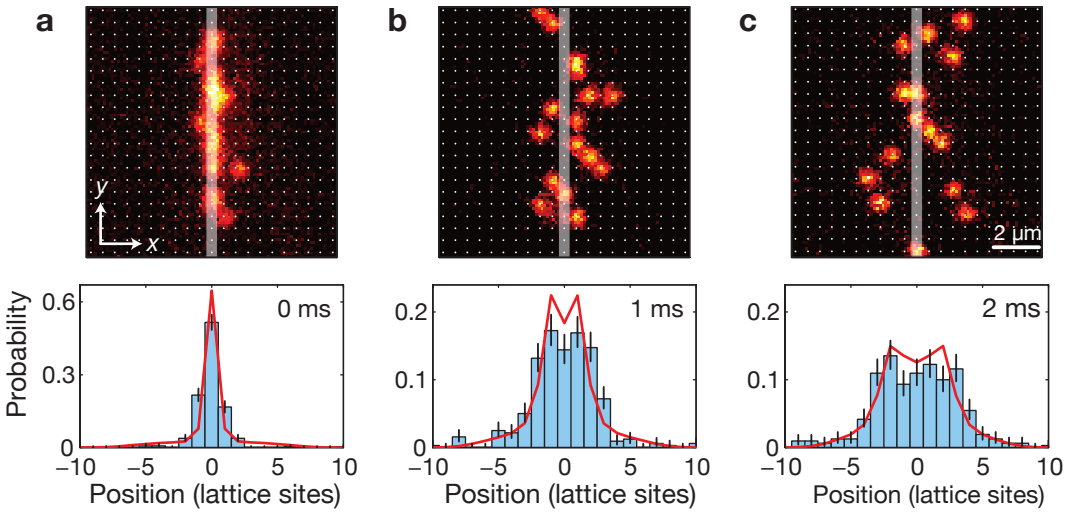

Figure 4.3: Spin impurity dynamics in the SF regime. Density distribution at $(J/U = 0.32)$ close to the critical point $[(J/U)_c \approx 0.3]$ for three different hold times. The upper panels display fluorescence images of the impurity spins after removing the other spin component ('positive image'). The 1D chains containing more than one atom were excluded from the data analysis. The white vertical stripe highlights the initial position of the flipped spin impurity. The lower panels show the position distribution averaged over about 300 chains (blue bars) together with a t-DMRG simulation at $T = 0.11\,U/k_B$ (red line).

The mapping of the two-component Bose gas to the spin-1/2 model is only valid deep in the MI phase with unity filling. In that regime, only thermal fluctuations alter the coherent propagation. Towards the superfluid regime and especially in it, this mapping loses its validity. The $|\downarrow\rangle$ bath has strong quantum fluctuation with low-energy excitations and the interference structure gets washed out as seen in Figure 4.3.

In the superfluid phase, the quantum fluctuations lead to a Fröhlich-type Hamiltonian and it is natural to treat the $|\uparrow\rangle$ impurity together with the deformation of the bath as a polaron. We study the crossover to this regime by lowering the lattice depth during the evolution, which increases the ratio of J/U. In the superfluid regime, only the positive imaging technique

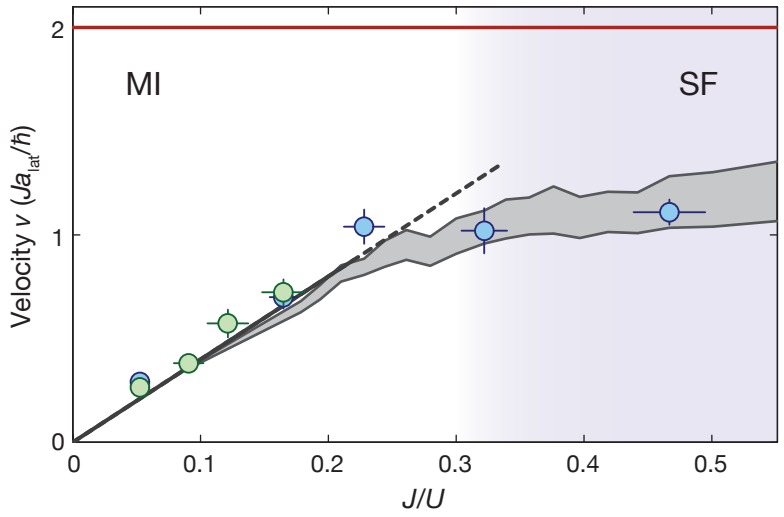

Figure 4.4: Spin dynamics across the superfluid-to-Mott-insulator transition. Measured velocities of the spin impurity for different values of J/U extracted from negative (green circles) and positive images (blue circles); horizontal and vertical error bars indicate the 1σ uncertainties of the lattice depth and the combination of fit error and uncertainties of J, respectively. The dark gray line shows scaling with $4J^2/U$, whereas the brown line indicates the propagation velocity of a single free particle ($J/U = \infty$). The gray shaded region shows results from a t-DMRG simulation at $T = 0$ taking into account varying initial atom numbers. The area denotes the 1σ fit error to the simulated distributions.

can be used, as it is not possible in negative imaging to identify the spin position out of many quantum fluctuations, which show up as holes as well. After preparing the initial state at high lattice depth, the lattice depth is reduced relatively slowly in 50 ms to avoid any heating. The spin $|\uparrow\rangle$ impurity cannot move during this ramp as the addressing beam creates an attractive potential which pins the impurity. Equation 4.1 is the analytical solution for the Heisenberg spin chain. No full analytical solution exists which describes the propagation of the impurity in the Bose-Hubbard model. A fit of $P_j(t)$ with the velocity as the only free parameter still captures the velocity of the edges in the position distribution, which is given by the maximum propagation velocity. We determine the velocity over the full range of J/U, which is accessible in the experiment spanning a full order of magnitude from 0.05 to 0.5. For small J/U the velocity divided by the tunneling rate J increases linearly with a slope of 4, which perfectly agrees with the theoretical expectation for the spin exchange coupling strength of $4J^2/U$. Close to the phase transition point of the superfluid-Mott-insulator transition in a homogeneous

system, the normalized velocity saturates. In the superfluid regime, it is finally significantly smaller than $v/J = 4J/U$. Here, the velocity of the polaron is approximately half the velocity of a free particle moving in the same lattice, given by $v/J = 2a_{\mathrm{lat}}J/\hbar$. This points out that the strong interactions modify the motion of the particle and increase the effective mass of the impurity. Such a behavior is expected and agrees with simulations of the two-species Bose-Hubbard model. Therefore the propagation velocity is extracted from density distributions, calculated with t-DMRG simulations [165–169], with the same method as used for the experimental data. The simulations take into account the harmonic trap as well as atom number fluctuations, which both can influence the propagation significantly. The obtained velocity as well as the numerically determined density distributions agree well with our experimental data.

4.1.6 Polaronic bath deformation

A polaron is a quasiparticle formed by an impurity that has a significant back-action on the bath, which in our case forms a density dip at the position of the impurity. We confirm the connection in our data with density measurements on the bath. The measurements were carried out at $J/U = 0.47(5)$ where quantum fluctuations affect the detected parity signal $n_{\mathrm{det}} = \langle \mathrm{mod}_2(n_\downarrow) \rangle$ [10]. Before releasing the impurity, the distribution shows a prominent density dip at the central lattice site. We verified that this missing density is not caused by the potential of the addressing laser by omitting the MW pulse, which introduces the spin impurity but not changing other parts of the sequence. We found out that the preparation sequence does not influence the bath, as within the reference data no reduction in the central density is visible. The density depression in the datasets with an impurity has a width of only a single lattice site, which indicates that the healing length of the bath is either in the order of or smaller than the lattice spacing. The same experiment is repeated at a short hold time of 0.5 ms and the repulsion of the impurity on the bath is visible as well. Here, the position of the density depression in the bath agrees well with the impurity distribution and the distributions of the bath as well as the impurity agree well with DMRG simulations. The density reduction of the bath and the impurity positions are expected to become correlated within time evolution, which is verified in DMRG simulations in which the spatially averaged correlations are defined as

$$C_{\uparrow\downarrow}(j) = \sum_k \left(\langle \hat{n}_{\uparrow,k} \hat{n}_{\downarrow,k+j} \rangle - \langle \hat{n}_{\uparrow,k} \rangle \langle \hat{n}_{\downarrow,k+j} \rangle \right). \tag{4.3}$$

The second half of the sum ensures that initially the system has no correlations where the position of the impurity is pinned at the center and has no

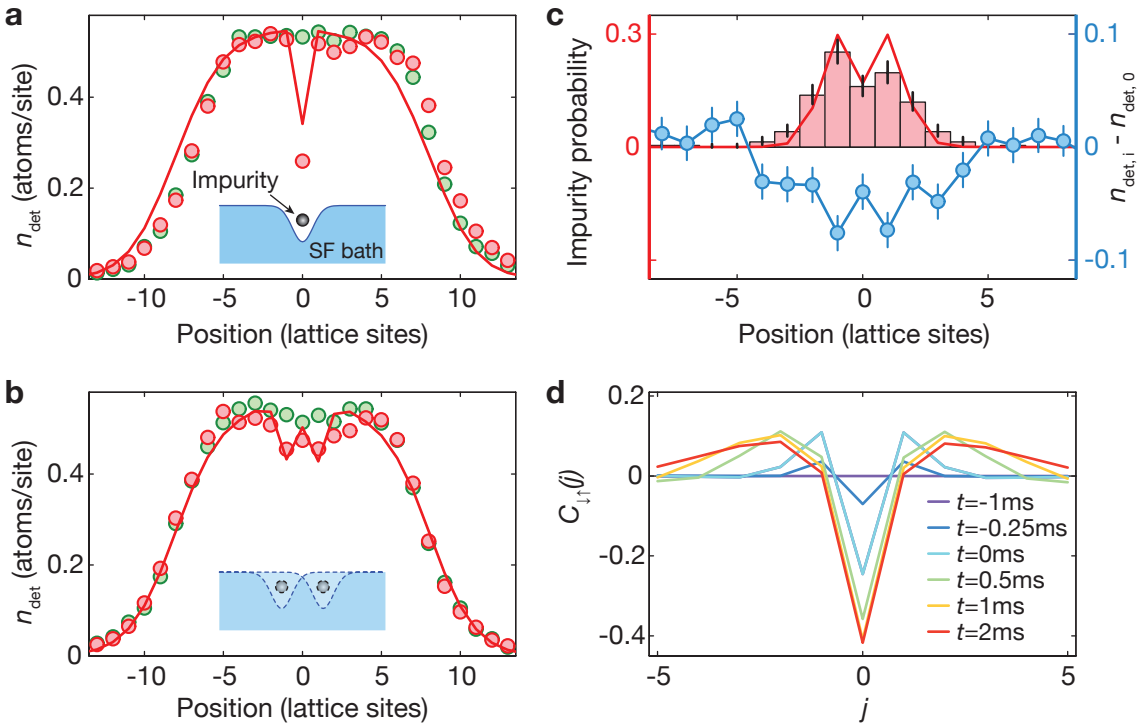

Figure 4.5: Influence of the impurity on the SF bath. Measured distributions n_{det} of the SF bath at $J/U = 0.47(5)$ with ($n_{\mathrm{det},i}$, red circles) and without the impurity ($n_{\mathrm{det},0}$, green circles), **a** before releasing the impurity and **b** after releasing and a subsequent evolution time of 0.5 ms. The data is averaged over more than 1000 chains. Statistical error bars are smaller than the plotted circles. The red lines show the t-DMRG simulation. Insets: schematic picture of a polaron, consisting of the impurity and the density deformation it induces in the bath. **c**, Probability distribution of the impurity after an evolution time of 0.5 ms (red bars, left axis) together with the simulation (red line, left axis). The blue circles (right axis) show the difference between bath distributions with and without impurity, calculated from the data shown in **b**. Error bars denote the 1σ uncertainty. **d**, Correlator $C_{\downarrow\uparrow}(j)$ calculated from simulations for different evolution times, reflecting the development of an anti-correlation at $j = 0$ as the impurity propagates after releasing it.

influence on the bath distribution. As the polaron starts moving, correlations and anti-correlations between the impurity and the bath are established. This was not verified in the experiment as detection of both spin states in the same realization was not possible.

4.2 Entanglement generation in spin propagation

In a second step we want to study in depth the dynamics of a single spin impurity in the regime where the dynamics are accurately described by the Heisenberg model. Hence, we focus on the generated correlation and extract a lower bound of the concurrence (see Chapter 3.3.5) to quantify the build up and propagation of bipartite entanglement. So far, in Hubbard systems realized with ultracold atoms, entanglement in the on-site occupation number degree of freedom has been inferred from the visibility of a far-field interference pattern [170, 171] and by the study of oscillations of coherent Rydberg superatoms [99]. A spatially resolved detection of entanglement has been recently proposed using the Rényi entropy [172, 173] and was measured with two copies of a four and six lattice site system [37, 125]. The extension of the Hubbard model to two-components introduces a spin degree of freedom [62, 63] such that spin-entanglement, in the sense of the concept of entanglement of particles [174, 175], can be present. First experiments with ultracold atoms showed that short-range coherent spin-dynamics can be controlled in bosonic [32, 176, 177] as well as in fermionic systems [178]. Spin exchange collisions in state selective optical lattices have been used to realize collisional gates between neighboring atoms [179], and global measurements indicated entanglement [180, 181]. However, a spatially resolved detection of either spin or occupation number entanglement in Hubbard models has still been an outstanding experimental challenge.

Inspired by measurements in ion chains [73], we report here on the spatially resolved detection of entanglement among spin degrees of freedom in a two-component Bose-Hubbard chain following a recent proposal [153]. Measurements in the longitudinal basis revealed the position of the impurity similar to the results in the previous section, while additional transverse correlation measurements were used to quantify its coherence. Combining both observables yields a lower bound for the concurrence [182, 183] in the spin-degrees of freedom of particles on two lattice sites [153]. We observe an outward propagating entanglement wave, the evolution of which we follow up to a distance of six lattice sites. Importantly, the detected bound is valid despite on-site particle-number fluctuations and proves entanglement of particles [174, 175, 184] in our system [153]. To study the effect of occupation number defects on the entanglement propagation in more detail, we developed a novel in-situ Stern-Gerlach imaging technique that yields information on both the local spin and the occupation number in one image.

4.2.1 Experimental procedure

The experimental procedure follows closely the one used for the single impurity dynamics in the previous section. Additionally, we put in huge effort to optimize the initial state. We were able to decrease the number of defects in the spin chains and increase the addressing fidelity. Within the relevant region of interest, the probability to detect an empty lattice site in the reference image was only $0.032(6)$, which corresponds to a reduction of the temperature by almost a factor of two. The final lattice depth of $10\,\mathrm{E_r}$ resulted in $J_{\mathrm{ex}}/\hbar = 2\pi \times 10\,\mathrm{Hz}$, $J/\hbar = 2\pi \times 39\,\mathrm{Hz}$ and $U/\hbar = 2\pi \times 800\,\mathrm{Hz}$ as the relevant parameters of the ongoing dynamics. Here, J_{ex} was directly extracted from the impurity dynamics as described in the previous section, while J and U were calculated for the calibrated lattice depths. The expected spin exchange coupling for the given lattice depth is 9.0 Hz including density corrections and only 7.3 Hz without these corrections (see Chapter 3.2.2 for details).

The ramp down to this final lattice depth was also slowed down to 50 ms compared to the previous experiments in order to reduce possible excitations.

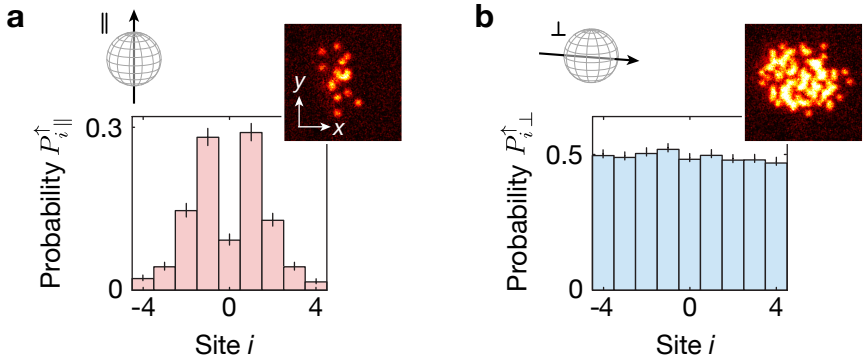

Figure 4.6: Longitudinal and transverse spin distribution. Representative experimental measurements in the longitudinal (left) and transverse basis (right) after $t = 35\,\mathrm{ms}$. The Bloch sphere pictograms indicate the measurement direction. The images show exemplary single shot images. The histograms show the probability at each lattice site to find an atom in the respective spin-resolved measurement.

4.2.2 Longitudinal spin distribution

We started by measuring the spin density distribution along the z-direction (longitudinal). We used the positive detection as well as the negative detection method. The probability $P_{i\,\parallel}^{\uparrow}$ to find one atom at site i after this longitu-

dinal ($\|$) measurement corresponds to the probability for the atom to be in the $|\uparrow\rangle$ state, where all atoms in the $|\downarrow\rangle$ have been removed before. In these measurements, clear interference fringes with high visibility were observed (see Figure 4.6a). The contrast of these measurements was higher than the contrast for the previous data even though no post selection was performed. We attribute this increase to the improved conditions.

4.2.3 Transverse spin distribution and correlation

In order to measure the analogous quantity $P^{\uparrow}_{i\perp}$ in the transverse basis, we added a global $\pi/2$ rotation in the experimental sequence before the spatially-resolved imaging. Spatially homogeneous magnetic field fluctuations randomize the transverse phase within less than 1 ms, resulting in rotational symmetry around the longitudinal spin axis. Consequently, the transverse spin distribution is uniform across the chain with equal probabilities for the $|\uparrow\rangle$ and $|\downarrow\rangle$ states (Figure 4.6b). We ensured that the magnetic field homogeneity was better than 50 mG/cm (0.2 Hz/a_{lat}) (see Chapter 3.4.2) such that transverse spin correlations are preserved over experimental timescales of 100 ms. Each data point presented in this paper is extracted from typically 800 (1000) individual realizations of the spin chain in the longitudinal (transverse) case. An exception is the data shown in Figure 4.10, where these numbers are five times lower because it take much longer to acquire statistics.

The spatially resolved measurement of transverse correlations $C_{i,j}$ is the crucial step towards the detection of entanglement dynamics. Without defects in the spin chain, the operator $\hat{S}^{\perp}_i$ directly relates to our experimental observable $P^{\uparrow}_{i\perp} = \langle \hat{S}^{\perp}_i \rangle + \frac{1}{2}$. Hence, the transverse correlations $C_{i,j} = P^{11}_{i,j\perp} - \frac{1}{4}$ are given by the joint probability $P^{11}_{i,j\alpha}$ to find one atom at site i and one at site j in the transverse ($\alpha = \perp$) measurement. Imperfections will always decrease these detected correlations such that $C_{i,j}$ provides a lower bound for them, even in an environment of on-site atom number fluctuations [153]. Figure 4.7a shows the measured transverse correlations together with the theoretical prediction for the ideal XX-spin chain. A strong positive signal appears between sites $+1$ and -1 after an evolution time of 20 ms ($1.26\hbar/J_{\mathrm{ex}}$) and subsequently these correlations spread further outwards. However, compared to the ideal case, a trend towards negative values is visible even between far separated sites that should be uncorrelated, given the short evolution times. A possible explanation for this lies in the imperfect initial Mott insulators resulting in $P^{1}_{i\perp} < 0.5$, which biases the measured $C_{i,j}$. This bias is removed in the modified transverse correlation $\widetilde{C}_{i,j}$, defined as $\widetilde{C}_{i,j} = P^{11}_{i,j\perp} - P^{1}_{i\perp} P^{1}_{j\perp}$ [153] similar to the definition in Chapter 3.3.4. In Figure 4.7b, we show the mea-

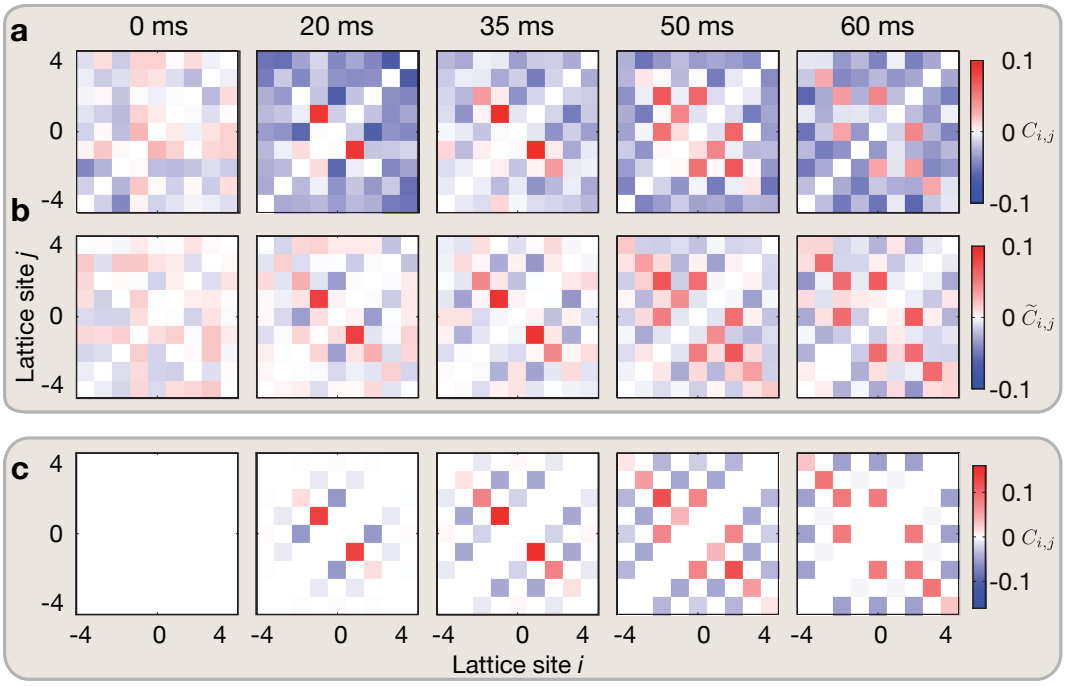

Figure 4.7: Transverse correlations. **a**& **b**, Experimental data of the correlations $C_{i,j}$ and $\widetilde{C}_{i,j}$ for different evolution times. The strongest signal corresponds to the outward propagating correlations between the sites $\pm i$ symmetrically located around the initial position (on the upper left to lower right diagonal). **c**, Theoretical prediction for an ideal spin chain. Remarkable qualitative agreement between theory and experiment is visible in the spatial structure of the correlations, but the amplitude of the experimental signal is reduced (different color scales).

sured $\widetilde{C}_{i,j}$, now in remarkable agreement with the theoretical prediction, except for the smaller amplitude of the measured correlation signal.

4.2.4 Quantifying entanglement by concurrence

We now combine longitudinal and transverse correlation measurements to detect spin-entanglement in the system. For the entanglement detection, we use a lower bound for the concurrence in the spin-1/2 degree of freedom which can be also used to prove entanglement of particles [174, 175, 184]:

$$\mathcal{C}_{i,j} = 2(2C_{i,j} - \sqrt{P^{11}_{i,j\parallel} P^{00}_{i,j\parallel}}) \,. \tag{4.4}$$

Here, $P^{00}_{i,j\parallel}$ is the joint probability of finding no atoms on sites i and j in the longitudinal measurement. It has been shown in Ref. [153] that $\mathcal{C}_{i,j}$ is a valid

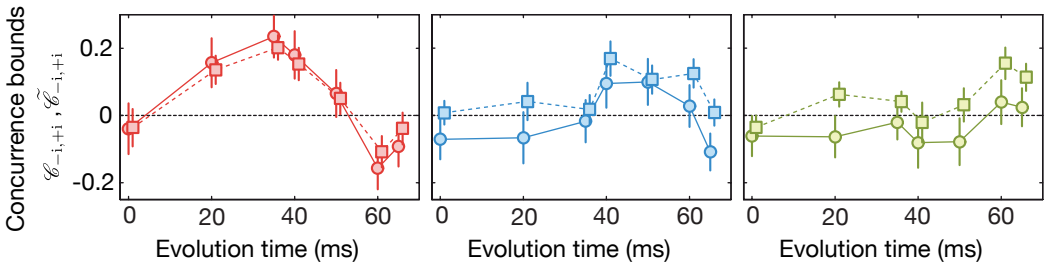

Figure 4.8: Propagation of entanglement wave. Lower experimental bounds for the concurrence $\mathcal{C}_{-i,+i}$ (circles with solid line) and the more efficient bound $\widetilde{\mathcal{C}}_{-i,+i}$ (squares with dashed line) between the sites $\pm i$ versus time. From left to right $i = 1$ (red), 2 (blue), 3 (green).

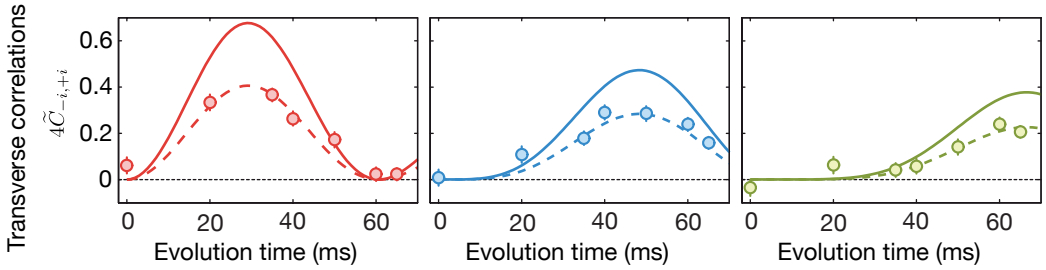

Figure 4.9: Propagation of transverse correlations. Transverse spin correlations $4\widetilde{C}_{-i,+i}$ for the same sites as in Figure 4.8. Circles are the experimental data and the solid lines show the predictions for the defect-free ideal case, where $4\widetilde{C}_{-i,+i} = \widetilde{\mathcal{C}}_{-i,+i} = \mathcal{C}_{-i,+i}$. The dashed lines are the ideal predictions scaled by 0.6.

lower bound for the concurrence even in the case of fluctuating particle numbers, as long as the maximum on-site occupation number does not exceed two. This requirement is fulfilled in our experiments where the total atom number is tuned to yield a unity filled Mott insulator in the center of the trap. Assuming the worst-case scenario, that the observed hole probability of $0.032(6)$ is only due to doubly occupied sites and an exponentially decreasing occupation of higher excited states, we expect a probability for triply occupied states of 10^{-3}. With the weak additional assumptions of vanishing correlations between the site occupation numbers and between all degrees of freedom in the doubly occupied sector, a more efficient bound $\widetilde{\mathcal{C}}_{i,j}$ on the concurrence can be obtained by replacing $C_{i,j}$ by the modified transverse correlations $\widetilde{C}_{i,j}$ in Equation 4.4 [153]. It is reasonable to assume that these conditions are fulfilled in the experiment for non nearest-neighbor sites, given the very low probability for double occupation.

The results of the concurrence measurements are shown in Figure 4.8 for pairs of sites symmetric around the initial impurity position. They reveal a buildup of entanglement in the spin chain leading to a peaking concurrence $\mathcal{C}_{-1,+1} = 0.24(6)$ between the sites $\pm 1\, a_{\mathrm{lat}}$ away from the center after 35 ms. For longer times, the concurrence peaks at larger distances and shows a ballistic outward propagating entanglement wavefront. Using the bound $\widetilde{\mathcal{C}}_{i,j}$, we find finite entanglement up to distances of six lattice sites. Note that the bound for the concurrence is expected to be especially efficient for pairs of sites located symmetrically around the initial position, which is consistent with our observations (compare to Figure 4.7). The observed concurrence closely resembles the transverse correlations that are shown in Figure 4.9 for comparison. Its amplitude is only slightly decreased due to our finite fidelity in the preparation of the initial spin-impurity. Comparing the measured transverse correlations $\widetilde{C}_{i,j}$ quantitatively to the expectation for a perfect chain, we find good agreement after a constant down scaling of the theoretical correlation amplitude by 0.6. Such an effect has indeed been predicted in an environment of holes and doubly occupied sites [153]. A decreasing entanglement signal with increasing site separation is also expected in the ideal case due to the dispersion of the single-spin-impurity.

4.2.5 Impact of defects on spin-entanglement

The results for the concurrence extracted from the spin-resolved measurements are shown in Figure 4.10c. For the analysis, we discarded all pictures with more than one atom per y-tube (approx. 25 %), as those were predominantly caused by imperfect preparation of the single 1D system. After this, the concurrence signal $\widetilde{\mathcal{C}}_{-1,+1}$ agrees with the previously measured one within experimental uncertainty – an indication that double occupancies had little impact on the measurements reported above. Next, we further postselected the data to a fixed number of holes (between zero and three) within the central nine sites. For the zero-hole data set, our measured concurrence indeed matches the expectation for an ideal XX-spin chain while it rapidly decreases for increasing hole number. For three holes, i.e. a hole density of 30 %, no entanglement is detected any more showing that defects critically affect the coherence in the spin sector.

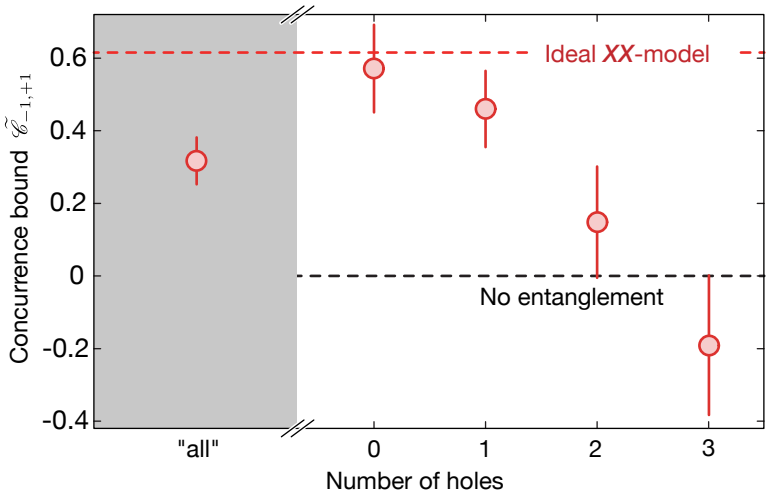

Figure 4.10: Impact of defects on spin-entanglement. Lower concurrence bound $\widetilde{\mathcal{C}}_{-1,+1}$ after 35 ms evolution for the full dataset (point in the left gray part) and for subsamples postselected to 0, 1, 2 and 3 holes in the chain. The red dashed line indicates the value expected for the perfect XX-spin chain, the black dashed line is the boundary for the presence of entanglement. Error bars indicate one standard deviation of the mean.

4.3 Dynamics of bound magnon states

More features of the Heisenberg model are accessible with additional excitations, whereof the excitation of two adjacent spins is the natural extension of the previous sections. Already the full solution of the Heisenberg spin-1/2-model [6] revealed that the elementary spin waves (magnons) in one-dimensional quantum magnets can form bound states. Here, we probe the dynamical properties of two magnon states and are able to distinguish the propagation of free and bound states. The increased effective mass of the compound magnon state results in a slower expansion compared to the free magnon. Magnon bound states are essential, even at low energy, as they exist for all center of mass momenta in 1D and 2D [185, 186]. Due to the ferromagnetic interaction, two spin excitations can remain bound together, forming a so-called two-magnon bound state [6, 185, 187]. In one and two dimensions, bound states exist for all center-of-mass momenta, which prohibits the description of low-energy properties in terms of free magnon states [185]. In the classical limit, magnon bound states can be regarded as the basic building blocks of magnetic solitons [188, 189].

Next to these fundamental aspects, the study of non-equilibrium dynamics in quantum spin chains is also important for a variety of applications. The evolution of two localized spin excitations realizes an interacting quan-

tum walk [190, 191] in the spin domain, which can be a versatile tool for the study of complex many-body systems [192]. It is also of importance in the context of quantum information [193], where the information transport in a one-dimensional chain of qubits can be strongly influenced by magnon bound states.

Experimentally, spectroscopic studies of solid-state materials provided first evidence for the existence of such states [194–196]. For ultracold atoms in optical lattices, high-energy bound states have been observed in the density sector in the form of repulsively bound atom pairs [197, 198].

4.3.1 Experimental procedure and initial state

The initial-state preparation followed closely the previously described sequence of the single impurity experiments. First, a spin-polarized ($|\downarrow\rangle$) MI was created, which was locally manipulated with the single-site approach in the strongly localized regime to flip two atoms next to each other to the second spin state ($|\uparrow\rangle$). After the preparation, the lattice depth along the 1D chains was reduced to $V = 10\,\mathrm{E_r}$ while the addressing light was used to pin the spin impurities at their initial positions. After the system had evolved for a variable evolution time of up to 120 ms, the motion was frozen out by rapidly ramping up all lattices to $80\,\mathrm{E_r}$.

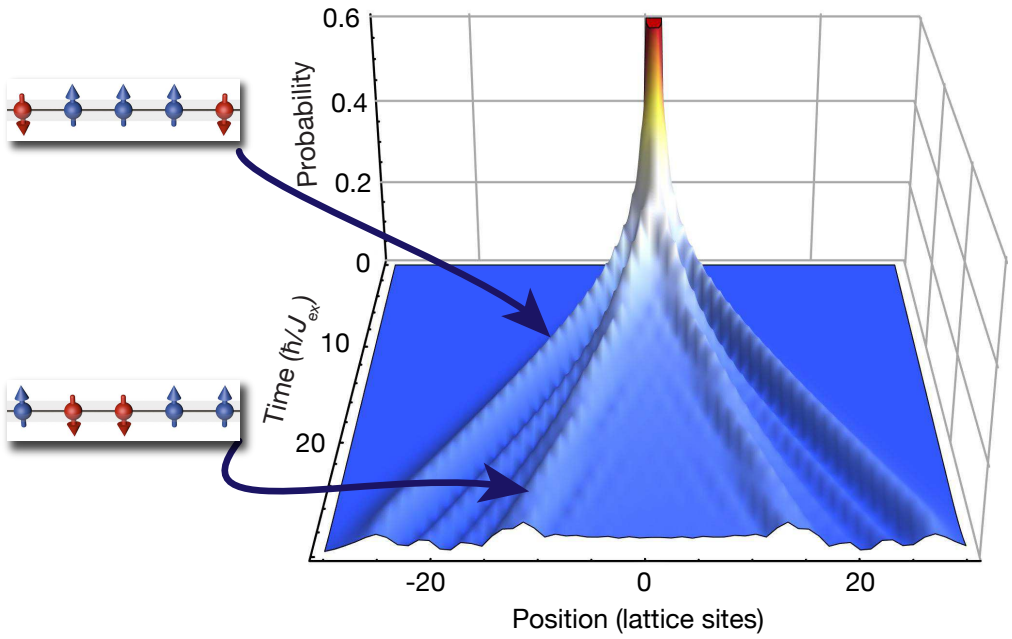

Figure 4.11: Bound magnon time evolution. Numerical results obtained from exact diagonalization showing the probability to find a flipped spin at a given lattice site following the initial state preparation. Two different wavefronts corresponding to bound and free magnons can be identified (see insets). Note that the maximum probability was clipped in the graph at 0.6 for better visibly of the smaller probabilities.

4.3.2 Physical system

The experiments are performed at a relatively large lattice depth of $10\,E_r$, which implies that the interaction strength is much larger than the tunneling rate. Thus, as validated in Chapter 4.1, the Mott insulating state at unity filling is mapped to an effective spin-1/2 chain described by the XXZ Heisenberg Hamiltonian where J_{ex}, the superexchange coupling, and Δ, the anisotropy between the transversal and longitudinal spin coupling, are the relevant parameters describing the system.

At the chosen lattice depth, the coupling strength J_{ex} is large enough such that the dynamics are sufficiently fast ($J_{ex}/\hbar = 2\pi \times 8.6\,\text{Hz}$) compared to typical heating time scales, and several coherent spin exchanges are visible. The longitudinal coupling, which is responsible for the next-neighbor interaction between the spins, favors a ferromagnetic order for $J_{ex}\,\Delta > 0$. Due to this interaction, two flipped spins have a lower energy if they are located next to each other and hence form bound states. For the utilized atomic Rubidium states, the Heisenberg interaction is nearly isotropic, that is $\Delta \approx 1$ (see Chap-

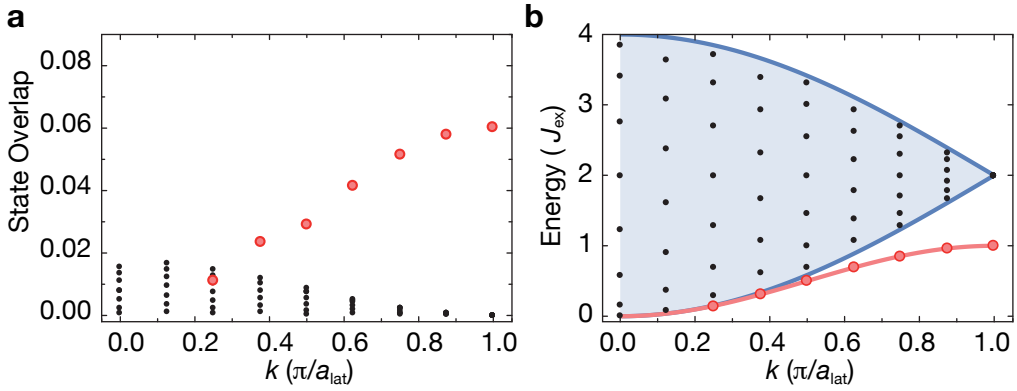

Figure 4.12: Quantum state analysis. **a**, Overlap of the initial state with the bound (red circles) and free (black dots) magnon states calculated for $N = 16$ lattice sites [199]. The total sum is normalized to 1. For illustration we show only the states with wave-vectors within the interval $k \in [0, \pi/a_{\mathrm{lat}}]$. The inset **b** shows the corresponding energy spectrum. Within the blue shaded region the free magnons are located while the red line shows the dispersion relation for the bound states.

ter 2.2.1 for details). We used the Bethe ansatz to obtain the full spectrum of the ideal one-dimensional spin system and compared this with analytical calculations for infinite systems [65] (see Figure 4.12). This analysis reveals that our initial state has a large overlap of 50 % with two-magnon bound states, while the rest is an overlap with free magnon states. Figure 4.11 shows the density propagation obtained from exact diagonalization.

4.3.3 Detection and tracking of magnon states

For the observations of the bound magnon, we focused on the positive imaging technique which allows to uniquely identify the position of the $|\uparrow\rangle$ spins. We followed the time evolution of our initial state by extracting the joint probability distribution $P_{i,j}$ from the atoms positions (see Chapter 3.3.4 for details on the joint probability distribution). Here we postselect on the data sets which had exactly two atoms per tube after the spin-selective imaging to limit the total magnetization to two $|\uparrow\rangle$ spins. Approximately half of the data sets were discarded, due to this filter criterion. The ratio of selected data is primarily limited by the finite spin preparation fidelity and the probability of holes at the addressed positions. The obtained joint-probability distribution $P_{i,j}$ is shown as two-dimensional plot in Figure 4.13. Bound states are located along the diagonal from the lower left to the upper right with $j = i \pm 1$. The bound-state population spreads along this direction with increasing evolu-

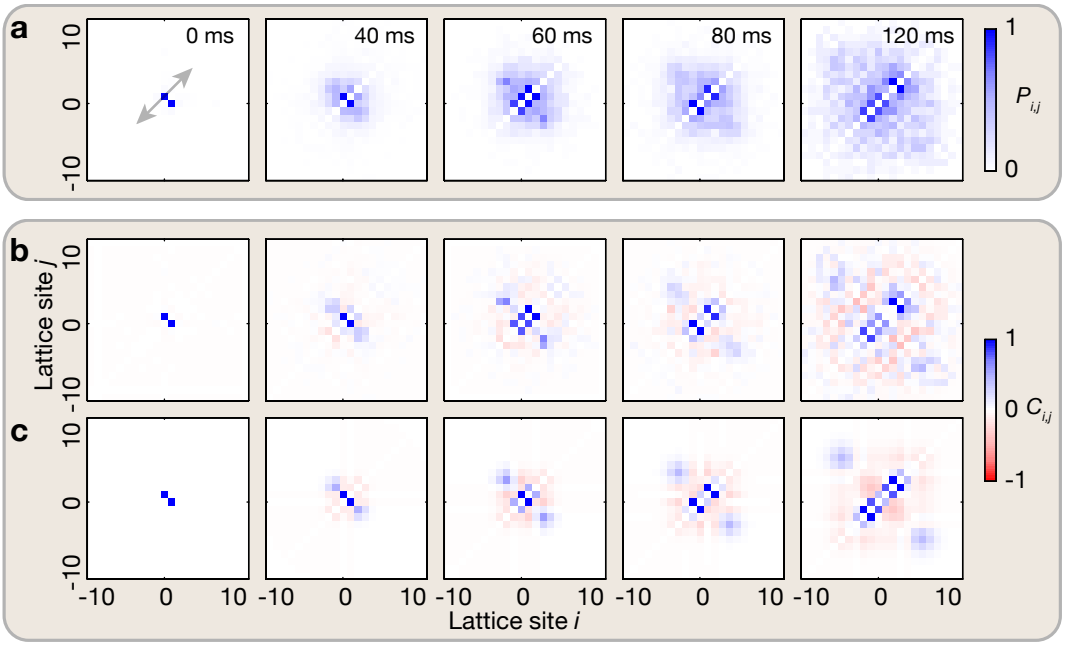

Figure 4.13: Spatial correlations after dynamical evolution. **a**, Measured joint probability distributions $P_{i,j}$ of the position of the two spins for different evolution times as indicated. The bound magnon signal and its spreading is visible on the diagonals $j = i \pm 1$ (arrow). Color scales are normalized for each image to the measured peak value. **b**, Corresponding correlation functions $C_{i,j} = P_{i,j} - P_i P_j$ of the measured data. The subtraction of uncorrelated detection events caused by finite-temperature effects and finite preparation fidelity gives better access to the correlation signal of the zero-temperature two-magnon evolution. For example, anti-bunching for the free magnons becomes visible, which is reflected in the outward propagating signal along the orthogonal diagonal. **c**, Numerical results for the correlations using exact diagonalization. Color scales are normalized analogous to **a**. Note that the mirror symmetry around the $j = i$ diagonal in all plots is given by indistinguishability of the two spins.

tion time. This motion is a signature of the correlation within the formed bound spin pair. The correlation function $C_{i,j}$ is an improved method to obtain information on the magnon propagation as it subtracts the uncorrelated events $P_i = \sum_j P_{i,j}$ due to finite temperature. In addition to the correlation signal of the bound magnon, a correlation signal along the orthogonal diagonal is visible. This signal is generated by the free magnon states and spreads at the predicted velocity of single magnons $J_{\mathrm{ex}} a_{\mathrm{lat}}/\hbar$. The two free magnons anti-bunch and are maximally seperated, which is expected from the possible mapping of the Heisenberg model to an effective spinless Fermion model

(see Chapter 2.2.2). Numerical results calculated with exact diagonalization of the defect-free Heisenberg model are in remarkable agreement with the experimental results (see Figure 4.13).

Velocity of the bound and free magnon

Further investigation focuses on the velocity of the bound magnon as well as the free magnon. The propagation of the bound magnon can be traced looking at the normalized probability to detect both magnons next to each other: $P_i^{\uparrow\uparrow} = P_{i,i+1} / \sum_j P_{j,j+1}$. This bound pair is expected to propagate almost freely. Hence, we use the same method as in Chapter 4.1.3 for the single impurity. The distribution is fitted with Equation 4.1 and we extract the width of the distributions. Additionally, we look at the added correlation signal for a given distance d between both magnons: $\tilde{C}_d = \sum_i C_{i,i+d}$. After time evolution, this correlation measure has two distinct maxima. The permanent maximum at $d = 1$ is due to the bound magnon pair and the second maximum is due to the unbound anti-bunching magnons whose position increases with hold time. The position of the propagating wavefront is determined by Gaussian fits ($A \exp[-(d-c)^2/s^2]$) and is defined as the center position plus one $1/e$-width taking into account the dispersion: $c + s$. Here we exclude the first maximum at $d = 1$ and all negative values from the fit.

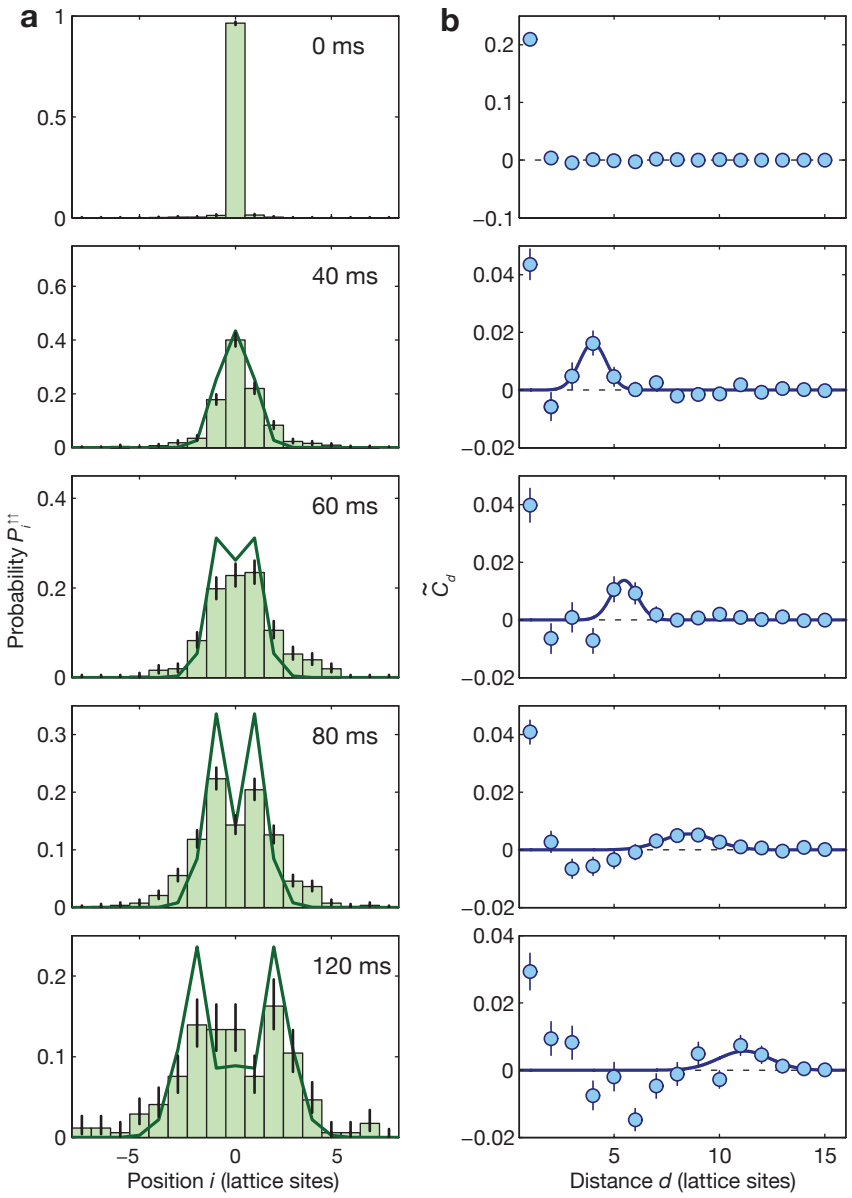

Figure 4.14: Spreading wavefront velocity of bound and free magnons. **a**, Bound state probability distributions $P_i^{\uparrow\uparrow}$ for different evolution times. The green bars show the experimental data. We extract the widths via Bessel function fits to the data (solid green lines). **b**, Propagation of the free magnons. The extracted correlation functions $\tilde{C}_d$ versus distance d are plotted for the same evolution times as used in **a** (blue circles). The signal at $d = 1$ is due to the bound states while the outwards moving peak stems from free magnons. The position and width of these peaks are captured by Gaussian fits (dark blue lines).

Figure 4.14 shows the wavefront position versus time for both signals. We fit a linear slope to the wavefront propagation in both cases to extract the velocity. The bound pair has a velocity of $v_b = 26(^{+2+6}_{-2})\,\mathrm{s}^{-1}$ and the free magnon propagates with a velocity of $v_f = 60(3)\,\mathrm{s}^{-1}$, which is $v_f/v_b = 2.3(^{+7}_{-2})$ faster (see Figure 4.15). This agrees well with the theoretically predicted value $v_f/v_b = 2\Delta = 2$. Here the error for the velocities are due to the fit. Additionally, the error of the bound state velocity includes an systematic underestimation. We validated our method on extracting the propagation velocity of the bound state by fitting equation 4.1 to numerical results obtained from exact diagonalization. These simulations demonstrate that the Bessel function does not exactly describe the distribution but the extracted velocity in the long time limit agrees with theoretical prediction of $J_{\mathrm{ex}} a_{\mathrm{lat}}/2\hbar$. However, for the short experimentally accessible times, the fit can underestimate the velocity by up to 20 %. In contrast, the same simulation points out that the systematic error on the fit of the velocity of the free magnon is only 3 %.

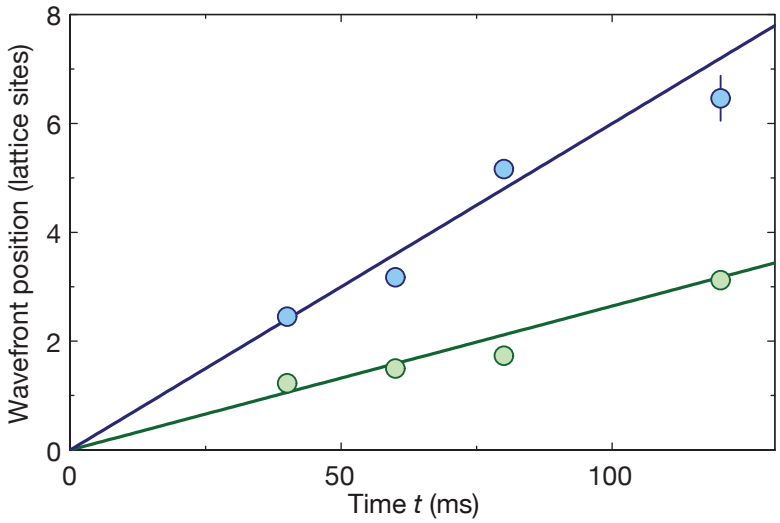

Figure 4.15: Comparing the propagation velocities of bound and free magnons. Linear regression of the extracted widths for the bound states (green) yields a velocity of $26(^{+2+6}_{-2})$ sites/s compared to $60(3)$ sites/s for the wavefront of the free magnons (blue).

Breakup of bound magnons

The extracted velocities for the free and bound magnons are consistent with the prediction by the isotropic Heisenberg model. The actual experiment was done only close to unity filling, where the Bose-Hubbard model is perfectly mapped to the Heisenberg model. Here, the initial Mott insulating state had

a residual probability of a doublon or hole excitation in the atomic chain of approximately 10 % due to the finite temperature and quantum fluctuations. We conjecture that these thermal excitations can break bound magnons which leads to a finite lifetime. This will affect the probability to detect both impurities next to each other ($\sum_i P_{i,i+1}$). Here, we compare the measured probability with numerical results for the zero temperature Heisenberg model for the isotropic interaction ($\Delta = 1$) as well as the non-interacting case ($\Delta = 0$) and take into account the finite initial preparation fidelity ($87(1)$ %). The non-interacting case does not favor the formation of bound state and hence the probability to detect both impurities on adjacent lattice sites approaches zero. For the isotropic model, a persistent value of 38 % is computed. This value is below the initial state overlap with the bound state because bound states extent over more than two lattice sites and both impurities do not need to be next to each other after the projective detection measurement. In the analyzed time interval, the probability of two adjacent impurities is in between both theoretical predictions. We fit a heuristic model, the numerical results of the isotropic model multiplied with an exponential decay, to our data (See Figure 4.16). The measured lifetime is $\tau = 210(20)$ ms, where the uncertainty includes the uncertainty of the fit and the numerical calculation. We believe that the bound states are predominantly limited in lifetime due to the initially present defects in the spin chains and additional heating during the experimental sequence.

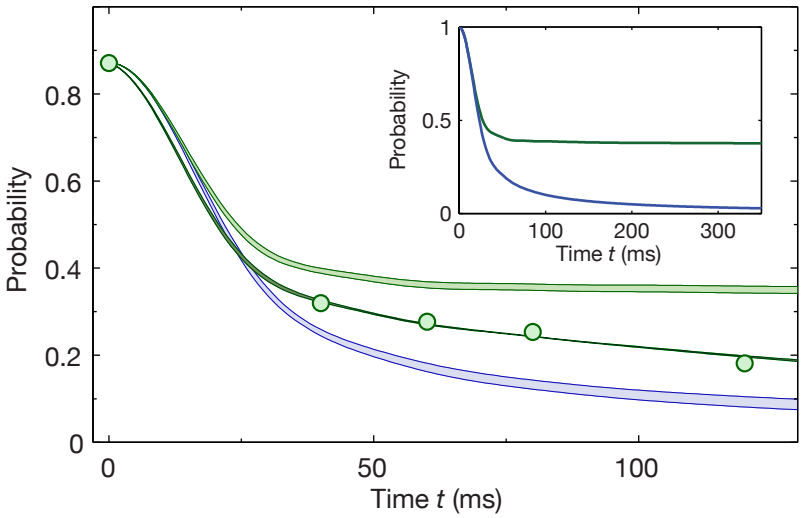

Figure 4.16: Stability of the bound state. Probability to find two spins at neighboring sites as a function of the evolution time. The green circles are the experimental data and statistical error bars are smaller than the circles. We show numerical calculations (exact diagonalization) for the isotropic $\Delta = 1$ case (green shaded area) and for $\Delta = 0$ (blue shaded area), taking the preparation fidelity of 87% and the resulting uncertainty into account. The darker green line is a fit based on the isotropic numerical result multiplied by an exponential decay. Inset: Numerical prediction for longer evolution time and without correcting for the preparation fidelity. The nearest-neighbor probability approaches zero in the $\Delta = 0$ case (blue line) while it converges to a finite value of 38% for $\Delta = 1$ (green line).

4.4 Summary

These first experimental results on the dynamics of a deterministically created spin impurity in a 1D lattice across the SF-MI transition demonstrate that indeed a mapping to the Heisenberg model in the MI regime is possible. Even though the density distribution is altered by propagating holes, a coherent propagation leads to a large contrast of the observed interference pattern. This demonstrates that our cold atom experiment is well isolated from its environment and is suitable for the quantitative study of quantum magnetism described by the Heisenberg model [200]. Additionally, we were able to spatially resolve the polaronic deformation of the bath by an impurity and its increased mass due to the back-action.

In a second step, we have experimentally measured the propagation of bipartite entanglement in the spin degree in a Heisenberg model realized with an optical lattice filled with ultracold atoms. Using a novel detection method,

we have shown that atom number defects are critical for the transverse coherence and hence for entanglement in the spin sector. This method also gives access to inter-spin correlations, an important quantity to characterize two-component bosons in the superfluid regime [155]. Our measurements pave the way toward in-depth studies of entanglement in quantum many-body entangled systems [132] and mark the first steps toward controlled entanglement transfer across spin wires [193, 201, 202]. Furthermore, we deterministically created a local excitation consisting of two magnons in a Heisenberg spin chain, which we microscopically tracked during its dynamical evolution. We determined the bound fraction by the correlation signal and studied the first realization of an interacting quantum walk in a magnetic spin chain.

These experiments pave the way for a further in depth study of coherent quantum magnetism. In particular, a predicted and new universality class of single-particle excitations in 1D systems could be tested in the future by measurement of spin-flip response and Green's functions [203]. Other natural extensions of this work would be the investigation of the correlated propagation of several flipped spins due to the ferromagnetic spin-spin coupling in the Heisenberg model [204] or the quantum simulation of the impurity dynamics in 2D, where numerical simulations and analytical studies are much more difficult. Our multiple-site addressing technique could also be used to prepare further non-equilibrium states of quantum many-body systems such as spin domain walls [205] and study their evolution. Experiments could probe the fractionalization of excitations that naturally occurs in one dimension, either when magnons decay into two spinons, or when spin and charge excitations separate [206]. In all theses system entanglement entropy plays a crucial role to understand thermalization which needs to be determined with suitable measures. Future studies might address the question of the stability of magnon bound states in an environment containing thermal as well as stronger quantum fluctuations or even the binding of two impurities in a superfluid environment, where one expects a "bi-polaron" to form. Here the newly developed detection of both spin states and density will be especially useful. Other interesting extensions would be the study of universal Efimov physics using three magnons [207]. The reported results also pave the way towards the deterministic microscopic engineering of complex magnetic many-body states and the study of magnetic correlations in non-equilibrium situations.

5 Far-from-equilibrium spin dynamics

The Heisenberg spin model has posed fundamental challenges for the understanding of non-equilibrium dynamics in quantum magnets. The concept of spin diffusion was introduced more than 60 years ago on a very basic phenomenolgical level [208–210]. It has been commonly applied to interpret nuclear magnetic resonance spin lattice relaxation and electron spin resonance experiments [211–215]. However, up to now it has never been justified *ab-initio* from a microscopic model. Moreover, many analytical and numerical studies suggested the existence of anomalous diffusion in Heisenberg models at infinite temperature, because of non-trivial commutation relations between spin operators leading to a failure of usual hydrodynamics [216–219]. The strongest evidence for anomalous diffusion resulted from the memory function approach [216, 217] and classical numerical simulations at infinite temperature [218, 219]. In one dimension, Heisenberg models have the additional property of being integrable [6]. As a result, at zero temperature the linear spin response is ballistic in the gapless phase [220] while at finite temperature no definite conclusion could be reached so far [221–233]. It has been argued that the regular, non-ballistic contribution to spin transport can indeed be of diffusive character at finite temperature [227, 228].

Whereas the focus in Chapter 4 was on this ballistic propagation of spin impurities close to the ground state, we probe here the high energy regime by preparing far-from equilibrium initial states to study the high temperature spin transport behavior. This research is also motivated by recent experiments on spin diffusion in ultracold fermions [234–236], which found an exceptionally low transverse spin diffusion constant in two dimensions [235], very different from three dimensional results [236]. These so far unexplained results motivate studies in alternative systems to check the generality of the observation. In our experiment and numerical simulations, we find that spin dynamics at high-energy-density in one-dimensional Heisenberg systems exhibits diffusive character. An intuitive way to understand the emergence of such a classical-like transport is given through interaction-induced dephasing between the many-body eigenstates spanning the initial spin spiral state. In contrast, the 2D system is shown to exhibit anomalous super-diffusion for the observed intermediate timescales, in agreement with earlier predic-

tions [217]. We find in both cases that the closed quantum evolution at high-energy-density is in strong contrast to the one of a few excited magnons, which propagate ballistically [155, 156, 204].

5.1 High energy regime of a Heisenberg spin system

We focused our research to systems deep in the MI regime with close to unity filling. In this strong coupling regime, our atomic lattice system can be mapped to the ferromagnetic Heisenberg model [62, 63] which is slightly modified in our case due to a small number of mobile particle-hole defects (See Chapter 2.2.1 and 2.2.3). Here $J_{\mathrm{ex}} \approx 4J^2/U$, superexchange coupling, and Δ are the remaining characteristic parameters describing the system. We note that for the spin states employed in the experiment, the interaction energies for different spin channels vary only on the level of 1 % resulting in an almost isotropic model with $\Delta \approx 1$ [114] (see Chapter 3.2.2 for detailed values). Thus the system is rotationally invariant and does not prefer any distinguished axis. We restrict the discussion to the dominating effect of holes in the Mott insulator as the probability of doubly occupied sites is assumed to be lower and thus can be neglected. This is the same regime as in Chapter 4 but the initial state is very different.

We follow the concept of spin-grating spectroscopy [237–239] and prepare initial large amplitude transverse spin spirals

$$|\chi(\mathbf{Q})\rangle = \prod_j \left(|\uparrow\rangle_j + e^{-i\mathbf{Q}\cdot\mathbf{x}_j}\,|\downarrow\rangle_j\right) \tag{5.1}$$

with a controlled wave vector $\mathbf{Q}$, where $\mathbf{x}_j$ is the position of the lattice sites. The name comes from the fact that the Bloch-vector of the local spin 1/2 system spirals around the x-axis going along the wave vector $\mathbf{Q}$. These states are similar to previously studied Skyrmion states in 3D Bose-Einstein condensates but do not have a topological defect [240]. In contrast to Chapter 4, these states are not localized but have a better defined momentum state. Whereas the total magnetization for this state is zero, the previous initial state had all spins but one or two spins initially polarized in either the $|\downarrow\rangle$ or $|\uparrow\rangle$ state.

5.2 State preparation and detection

The experiment started with a Mott insulating state in the atomic limit at 20 E_{r} where all spins were polarized to the $|\downarrow\rangle$ state and each spin could be treated

as independent. Instead of using our site resolved addressing technique as in the previous chapter, we apply a well controlled magnetic field gradient in a similar approach as for the gradient calibration, described in Chapter 3.4.2. This is advantageous for the initialization of the required states as the fidelity of the addressing technique decreases with the complexity of the patterns and so far is only optimized for full spin rotations.

A global $\pi/2$-pulse (10 µs MW pulse duration) brought each spin in a symmetric superposition of $|\downarrow\rangle$ and $|\uparrow\rangle$ spin states. The applied magnetic field gradient $B'(\mathbf{x}) = 0.2\,\mathrm{G/cm}$ introduced a location-dependent Zeeman shift ($20\,\mathrm{Hz}/\mathrm{a_{lat}}$) leading to a locally varying Larmor precession. This results in a given wave vector $|\mathbf{Q}| \propto t/B'(\mathbf{x})$, as the precession led to a linear growth of the relative phase. Thereafter, the gradient was canceled to below 2 mG/cm. This is negligible during further time evolution, as the resulting change in the wave vector is below the resolution. The created state corresponds to the proposed transverse spin spiral state. Lowering the depth of either one or both horizontal lattices within 5 ms to the desired value between 8-16 $\mathrm{E_r}$ initiated the evolution of the strongly-interacting spins. The experiments in 1D were carried out in weaker lattices, as the transition point towards the superfluid region occurs at lower lattice depth. For the ramp-down, we chose a timescale that both minimizes heating, while still being short compared to the ensuing spin dynamics. The evolution was stopped suddenly after variable times by rapidly increasing the lattice depth to 40 $\mathrm{E_r}$ within 1 ms. A second $\pi/2$-pulse closed the global Ramsey interferometer by rotating the transverse spins to the measurement basis along the σ_z-axis. At the end, the local distributions of $|\downarrow\rangle$ spins n_i was measured using the spin selective imaging technique (Chapter 3.3.3).

5.3 Data analysis

The initial spin spiral state is visible in single shot of the $|\downarrow\rangle_i$ distribution but as the global phase of the spin spiral states $|\chi(\mathbf{Q})\rangle$ is uncontrolled, the structure is not evident in averaged data (see Figure 5.1). The main source of the unknown phase is the uniform magnetic field fluctuation as described in Chapter 3.4. The information is recovered through a second order correlation function $g_2(j,k) = \langle n_j n_k\rangle / \left(\langle n_j\rangle\langle n_k\rangle\right)$ (See Chapter 3.3.4). Neglecting defects in the spin chains, the averaged value is even equivalent to measuring $\mathrm{Re}\,\langle \hat{S}_j^+ \hat{S}_k^-\rangle$. The signal-to-noise ratio is increased by averaging over all positions for fixed distance d resulting in $g_2(d) = N\sum_j \langle n_j n_{j+d}\rangle / (\sum_j \langle n_j\rangle)^2$. Here $\langle\cdot\rangle$ represents the ensemble average over different experimental realizations, whereas the sum describes the spatial average over N different positions.

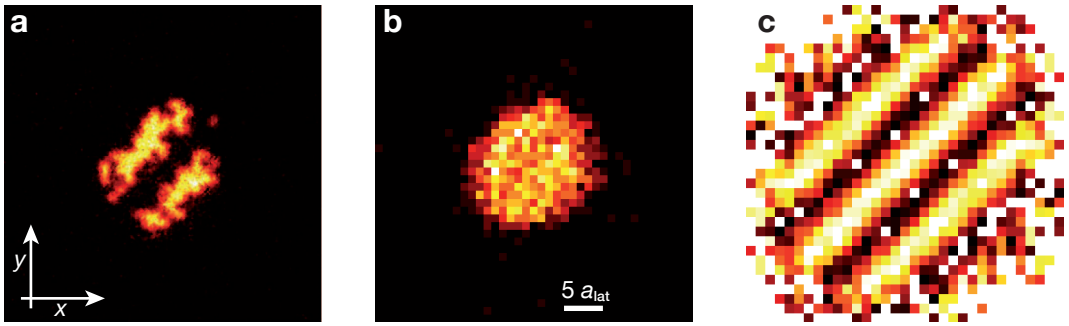

Figure 5.1: Spin spiral image. **a**, Single raw image of an initial spin spiral state. The phase of the spiral changes from shot to shot and the mean density is flat (**b**). Amplitude and periodicity of the spin spiral is recovered with the two dimensional correlation function (**b**). This example has a wavelength of $7.3(2)\, a_{\mathrm{lat}}$.

5.4 Dynamical evolution

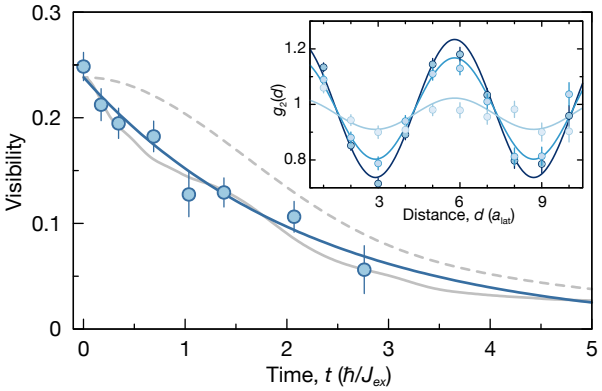

Figure 5.2: Decay of a 1D spin spiral. Measured decay of an exemplary 1D spin spiral with wavelength $\lambda = 5.7\, a_{\mathrm{lat}}$ at $10\, E_r$ lattice depth. The solid blue line is an exponential fit used to extract the lifetime. We also show theoretical predictions of the Heisenberg model (gray, dashed line) and the t-J model for 0.08 hole probability (gray, solid line). The inset shows three measured correlations $g_2(d)$ at $t_1 = 0$, $t_2 = 0.7\,\hbar/J_{\mathrm{ex}}$, $t_3 = 2.8\,\hbar/J_{\mathrm{ex}}$ (dark to bright blue), from which the visibility is extracted via sinusoidal fits.

We observe that the visibility of the spiral pattern decays with increasing times t_{hold}, while its period remains unchanged. An exemplary dataset for such a dynamics in 1D for an initial spiral with wavelength $\lambda = 5.7(1) a_{\mathrm{lat}}$ is shown in Figure 5.2. We determine a lifetime of $\tau = 30(3)$ ms corresponding to $2.1(3)\,\hbar/J_{\mathrm{ex}}$ from an exponential fit to the observed amplitude of the corre-

lation signal. A simple mean-field treatment of the relaxation dynamics in the Heisenberg model based on a Landau-Lifshitz type evolution equation does not exhibit any dynamical evolution because quantum fluctuations beyond linear order are responsible for the decay of the spin spiral. The nonlinearities are taken fully into account by exact diagonalization and we compare the experimentally observed decay to simulations of the Heisenberg as well as the t-J model. Both models predict an initial quadratic decay due to dephasing that happens on the fastest timescale of the model which is $\hbar/J_{\mathrm{ex}}$ for the Heisenberg model and the much faster $\hbar/J$ time scale for the t-J model. Experimentally, we only sample the decay on the superexchange timescale $\hbar/J_{\mathrm{ex}}$ and hence cannot resolve the fast initial dynamics in the t-J model. While the overall shape of the decay is model independent and is in good agreement with the experimental data, the t-J model simulation with an independently characterized hole probability of $\simeq 0.08(1)$ also reproduces the observations quantitatively.

5.5 Spin transport

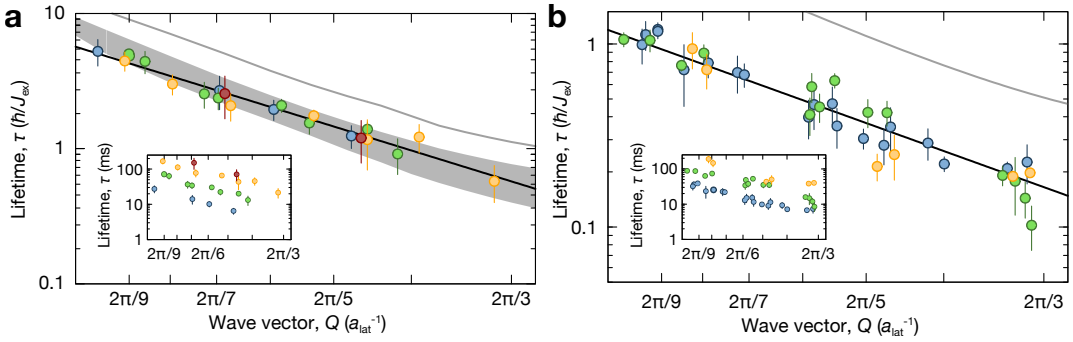

Figure 5.3: Wave vector dependence of the spin spiral lifetimes. We plot the data for 1D (**a**) and 2D (**b**) spirals double logarithmically and extract the exponents via power law fits (black lines). The lifetime is scaled with the superexchange rate $\hbar/J_{\mathrm{ex}}$, which results in a collapse of the measurements at different lattice heights [in 1D: 8 E_r (blue), 10 E_r (green), 12 E_r (yellow), 13 E_r (red) and in 2D: 12 E_r (blue), 14 E_r (green), 16 E_r (yellow)]. Additionally, predictions of the Heisenberg model (numerically solved in 1D, spin wave calculations in 2D) are shown as gray solid lines. The gray band in **a** is obtained numerically from the t-J model with hole probabilities between 0.04 and 0.12. The insets show the experimental data without scaling of the lifetimes.

We measure the lifetime τ for different wave vectors $\mathbf{Q}$, both in 1D and 2D, to learn more about the spin transport properties. In 2D we focused on spiral

wave vectors oriented diagonally to the lattice $\mathbf{Q} = (Q,Q)/\sqrt{2}$. The resulting data are shown in Figure 5.3 for both dimensionalities, different lattice depths and different initial wave vectors. The different initial wavelength range between $\lambda = 3a_{\mathrm{lat}}$ and $\lambda = 10a_{\mathrm{lat}}$, which is limited for the long wavelength by the system size and short wavelength limit is given by the discreteness of the lattice. We verify that the relevant time scale of the system is given by the exchange coupling J_{ex} as we find that the datasets for different lattice depths by scaling with this quantity. This probes the mapping of the Bose-Hubbard model to the Heisenberg model at much higher energy than the previous experiments (See Chapter 4.1). In order to gain further insight into the wave vector dependence of the spiral lifetime, we plot the data in a double-logarithmic plot and fit a power law with variable exponent α to the data $\tau \propto Q^{-\alpha}$. For our 1D data we find an exponent of $\alpha = 1.9(1)$ in good agreement with diffusive spin transport for which an exponent of 2 is expected. In contrast, the fitted exponent for the 2D system yields $\alpha = 1.6(1)$, significantly different and hinting at anomalous super-diffusion. For the analysis of the data, the exchange coupling J_{ex} was extracted independently from single magnon propagation measurements following our earlier results in Reference [155] and Chapter 4.1. In these measurements, we consistently find that the measured J_{ex} is $\simeq 20(10)\%$ larger than the one calculated from *ab-initio* single-band calculations without density corrections (See Chapter 3.2.2 for details).

5.6 Spiral decay

The observed diffusion-like behavior can be understood microscopically in the one-dimensional case, where the numerical simulations based on the Heisenberg model also point to an approximately quadratic dependence of the decay rate on the wave vector in the experimentally accessible region. As the spiral state is not an eigenstate of the Heisenberg model, it shows overlap with several many-body eigenstates.

The initial spin spiral evolves in time with the unitary quantum-mechanical time evolution operator

$$|\chi(\mathbf{Q})\rangle(t) = e^{-i\hat{H}t}\,|\chi(\mathbf{Q})\rangle = \sum_{\nu} e^{-iE_\nu t}\,|\nu\rangle\,\langle\nu\,|\,\chi(\mathbf{Q})\rangle\ . \tag{5.2}$$

In the second step, we projected the initial state on the eigenvectors of the Hamiltonian which spans a full basis. The time scale of the dephasing dynamics is thus approximately given by the spread of the energies ΔE_ν weighted by the overlap of the corresponding eigenstate and the spin spiral $\langle\nu\,|\,\chi(\mathbf{Q})\rangle$. The decay rate Γ of the spiral prepared with a certain wave vector $\mathbf{Q}$ should

therefore also be determined by this spread of energies ΔE_ν, which is discussed in Figure 5.4. We analyze the full many-body spectrum of the ferromagnetic Heisenberg model for spin chains consisting of either 12 or 16 spins.

The weighted spread of eigenenergies ΔE_ν on the spiral wave vector $\mathbf{Q}$ indeed increases quadratic, which supports the scaling of the decay rate with $\mathbf{Q}^2$ and thus provides a microscopic interpretation of the far-from-equilibrium dynamics in the one-dimensional Heisenberg chain.The diffusive-like behavior in the evolution of the spiral state can thus be traced back to a many-body dephasing effect, with the shortest decay time occurring for a classical Néel state $Q = \pi/a_{\mathrm{lat}}$ (see Reference [241]). The classical Néel state is very different to the highest energy eigenstate state but has overlap with states out of the whole spectrum. This calculation correctly predicts the scaling of the lifetime with the imprinted wave vector $\mathbf{Q}$ but the experimentally measured data is shifted systematically to lower values. We can reproduce this shift by considering the *t-J* model with the measured hole probability, indicating a good qualitative and quantitative understanding of the evolution. The Hilbert space in 2D is too large to perform exact diagonalization, for which reason the observations are compared to a spin-wave theory prediction assuming a hole free spin system.Again the qualitative behavior is described correctly but the experimental results are shifted systematically towards lower lifetimes. It is an open challenge to numerically simulate such 2D system taking into account the full complexity, as the underlying Hilbert space is prohibitively large.

The timescale of the diffusive behavior in 1D is set by the diffusion constant D. From dimensional analysis we find its natural units to be $\hbar/\widetilde{m}$, where $\widetilde{m} = \hbar^2/(2J_{\mathrm{ex}}a_{\mathrm{lat}}^2)$ is the effective magnon mass. The spin diffusion constant in d dimensions is estimated by $D = v\ell d$ where v is the velocity and $\ell = 1/n\sigma$ is the mean free path length which can be calculated from the density n and cross section σ [234, 235, 242]. We have demonstrated in the previous chapter, that the maximum velocity is given by the spin exchange coupling $v = J_{\mathrm{ex}}a_{\mathrm{lat}}/\hbar$. The mean free path for the strongly interacting spins is in the order of a_{lat} and thus the 1D diffusion constant is in the order of $D \sim J_{\mathrm{ex}}a_{\mathrm{lat}}^2/\hbar$. When assuming diffusive behavior to explain our data by fixing the exponent $\alpha = 2$, we extract $D = 0.22(1)\,\hbar/\widetilde{m}$. Remarkably, this is among the lowest values measured to date in a 1D many-body setting even though our measurements are carried out far from equilibrium in the highly excited regime.

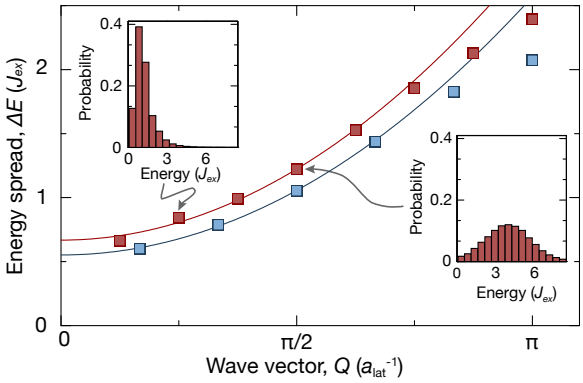

Figure 5.4: Microscopic view of the diffusion-like behavior in 1D. The energy spread of eigenstates contributing to the spin spiral decay grows quadratically with wave vector Q. This leads to the observed quadratic Q dependence of the decay rate, as expected for classical spin diffusion. The data shown for two system sizes of 12 (blue) and 16 (red) sites is obtained from full diagonalization of 1D Heisenberg chains. Insets show energy histograms weighted with the overlap of the initial spiral and the eigenstates for $Q = \pi/4a_{\mathrm{lat}}$ and $Q = \pi/2a_{\mathrm{lat}}$ for systems with 16 spins. A spin spiral with wave vector Q is a superposition of many-body eigenstates with wave vectors k that are integer multiples of Q.

5.7 Effect of hole concentration

This gives rise to the question of how the hole density influences the diffusion constant. In Fig. 5.5 we compare all 1D measurements for the lowest possible hole probability (the same data as shown in Fig. 5.3) with data obtained for larger hole probabilities. The higher hole probability is obtained by heating the initial MI state. Our data shows a clear trend towards increasing diffusion constant with increasing hole probability, consistent with numerical predictions based on the t-J model. A linear increase can be indeed expected in 1D as each hole – localized during the preparation – introduces a fixed phase defect.

5.8 Summary

In conclusion, we have studied far-from-equilibrium spin transport in the Heisenberg model using high-energy-density spin spiral states in 1D and 2D. A numerical analysis explained the observed diffusion-like behavior in integrable 1D chains on a microscopic level. We found that the main features of

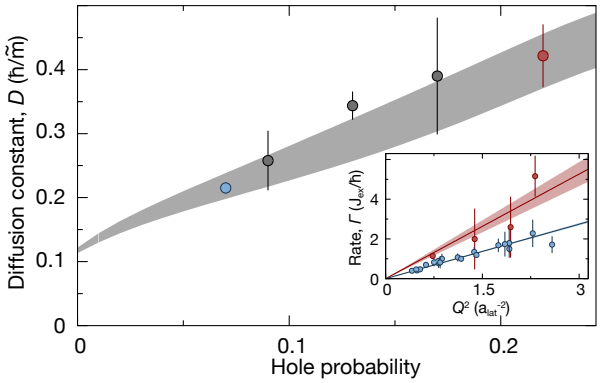

Figure 5.5: Dependence of the diffusion constant in 1D on the hole density. The diffusion constant D increases approximately linearly with hole probability. The gray area is the numerical result of the t-J model with its 95 % confidence interval. The inset shows the decay rate $1/\tau$ of the spin spiral versus the squared wave vector Q^2 for the lowest (blue) and highest (red) hole probability.

the magnetic spin transport are robust against a small number of mobile hole defects in the system. In contrast to the diffusive behavior in 1D we observed anomalous super-diffusion in 2D Heisenberg magnets where integrability is broken. For future studies it would be interesting to explore long-time behavior which in 1D might shed light on the question of a residual ballistic transport [221–233], while in 2D it could unveil a possible crossover from a super-diffusive behavior to sub-diffusive behavior [217]. Especially in 1D, it would be valuable to study spirals prepared with a wave vector close to $Q \sim \pi/a_{\mathrm{lat}}$, where a transformation to the antiferromagnetic Heisenberg Hamiltonian is possible. Thus one can expect that the dynamics can be described with a Luttinger liquid formalism and predictions of Reference [227, 228] could be tested. Furthermore, it would be interesting to study the absence of transport in interacting, many-body localized spin systems subject to quenched disorder [243] using for instance local interferometric techniques [244, 245].

In contrast to the previous ballistic experiments, the spin distribution equilibrates which is also expected for a thermalizing system and no information about the initial state is conserved. This is expected for a thermalizing system, but further studies would be needed to verify if the final state is in fact thermal.

6 Thermalization of isolated ultracold quantum gases

It is a typical textbook exercise to calculate the thermal state for closed classical systems. However it is much more difficult to understand how and under which conditions thermalization occurs for isolated quantum systems. This chapter provides a demonstrative explanation how closed quantum systems which evolve under uniform transformation can be interpreted as thermal. Thereafter, examples of non-thermalizing systems are given and many-body localization is introduced as a more generic setting where ergodicity is broken.

6.1 Closed Quantum Systems

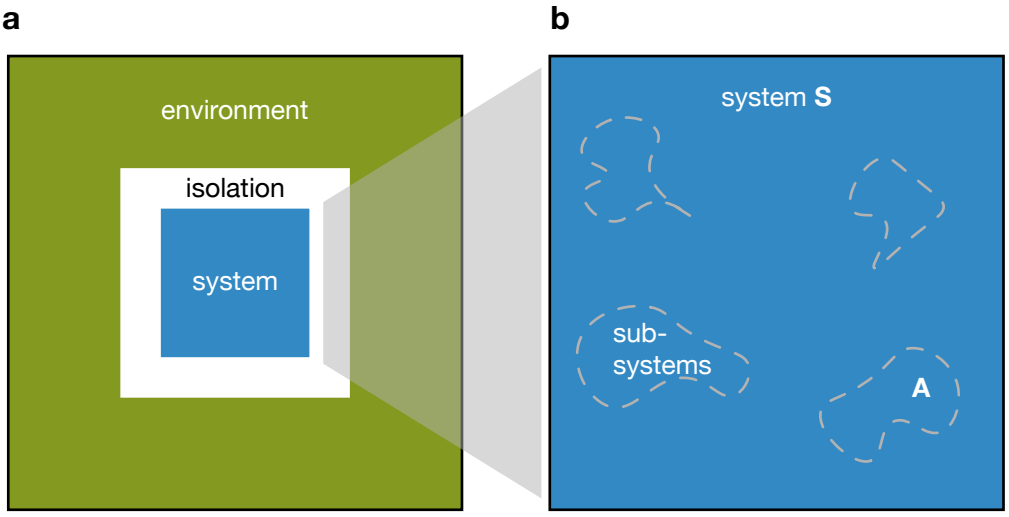

Figure 6.1: Isolated quantum system. **a**, Quantum gases in optical lattices are very well isolated from the environment and thus do not have an external heat bath. **b**, For quantum systems, local subsystems will look thermal even though the total system evolves under the unitary time evolution given by the Hamiltonian.

The evolution of a system can be strongly affected by its coupling to the environment. Identifying the properties of an uncoupled system is challenging if the connection to the outside world is not small compared to the relevant energy scales which are investigated. This is especially challenging for quantum phenomena as here the relevant energy scales are very small and the quantum nature is only visible if systems are cooled down such that the ground state acquires a macroscopic occupation. Coupling to external bath or noise source can lead to decoherence, which can qualitatively change the quantum evolution.

Additionally to classical closed systems where only the coupling to external thermal reservoirs needs to be suppressed, measurements play an important role in quantum mechanics and closed quantum systems are not allowed to have external observers. Too frequent observations of a system can even lead to complete suppression of quantum evolution [246, 247]. Hence to observe out-of-equilibrium dynamics in quantum systems, it is required that these disturbing factors are negligible. If this is fulfilled, the time evolution of a density matrix ρ in the Schrödinger representation under the Hamiltonian H is given as:

$$\begin{aligned} i\hbar\frac{d\rho}{dt} &= [\hat{H},\rho] \\ \rho(t) &= e^{-\frac{iH}{\hbar}t}\rho(t=0)e^{\frac{iH}{\hbar}t} \end{aligned} \tag{6.1}$$

The expectation value $\langle\hat{O}\rangle(t)$ for any observable $\hat{O}$ at time t is obtained by:

$$\langle\hat{O}\rangle(t) = \mathrm{Tr}\left\{\hat{O}\rho(t)\right\} \tag{6.2}$$

Note that here only the density matrix is time dependent but not the operator $\hat{O}$.

Besides many other experiments, the coherent spin propagation in Chapter 4 demonstrates that ultracold atoms are well suited to realize versatile closed quantum systems. The atom inside the vacuum chamber are well decoupled from their environment and additionally are only susceptible to certain frequencies as there energy spectrum is very discrete. Chapter 4 includes exemplary observations of coherent evolutions of quantum systems illustrating ballistic expansion of the wave function which indicates such a condition of isolation.

6.2 Thermalization

It is of fundamental importance to understand the final state of a system once it is perturbed and then allowed to evolve under unitary dynamics. The stan-

dardized concepts of statistical physics are applied to a wide range of physical problems, but often consider a coupling to an idealized bath [248]. There has been much research, experimental as well as theoretical, about how concepts of thermodynamics can also be applied to closed quantum systems. For systems in thermal equilibrium, a small number of intensive parameters (typically including temperature and chemical potential) are sufficient to describe the whole system accurately. In particular the precise initial state is unimportant and different initial states can lead to the same thermal state. It is an interesting question how these concepts can be applied to closed quantum systems as the information in a system is conserved under unitary time evolution. Since the unitary Hamiltonian can always be inverted in theory, the exact initial state can be recovered. However in experiments this information is not easily accessible anymore with local operators because it is rather hidden [39]. The basic notion of quantum thermalization arises already for a system which has no other conserved extensive quantity than energy, following the ideas of [5, 39]. Here we consider a small subsystem A within the total closed system S (See Figure 6.1). We now consider initial states $\rho(t=0)$ which thermalize to the temperature T and the expectation value of the total energy is given by $\langle H \rangle_T$. The density matrix for the system at thermal equilibrium with this temperature is given by $\rho^{(\mathrm{eq})}(T)$. A closed quantum system thermalizes if locally, in the small subsystem A, and in the long time limit t_∞ the reduced density matrix $\rho_A(t_\infty)$, calculated by tracing out the rest of the system $S \setminus A$, is the same as for the thermal equilibrium. Thus the following two equivalent equations need to be fulfilled for any choice of a small subsystem A:

$$\begin{aligned} \mathrm{Tr}_{S\setminus A}\left\{\rho(t_\infty)\right\} &\cong \mathrm{Tr}_{S\setminus A}\left\{\rho^{(\mathrm{eq})}(T)\right\} \\ \rho_A(t_\infty) &\cong \rho_A^{(\mathrm{eq})}(T)\,. \end{aligned} \tag{6.3}$$

This is strictly only valid in the thermodynamic limit for infinite systems where the fraction of degrees of freedom within the subsystem A over the total degrees of freedom goes to zero. For finite systems there exists a time, determined by the finite spectrum, where all eigenstates have again the same phase as at the beginning of the evolution and thus the system is quasiperiodic [39]. For infinite systems, however, the limit of infinite time has to be taken because any transport in finite time only reaches a finite volume. This statement can be relaxed if equation 6.3 only needs to be fulfilled at almost all times, ignoring the very special revival points, and hence also finite system can be defined as thermal. If a system thermalizes according to this definition for any initial state than this statement should even hold for eigenstates which do not evolve in time at all. The eigenstate thermalization hypothesis (ETH) explicitly claims that all eigenstates look locally thermal. There are

exact diagonalization results of small systems which strongly support that this argument is valid for almost all eigenstates but it is still a hypothesis as it is not derived from other arguments [39, 249–251]. If ETH is fulfilled it is also clear that only local observables need to look thermal and for example the non-local projection operation on eigenstates will not satisfy a thermal distribution if the system was originally close to an eigenstate. Thermalization was recently tested experimentally in a system of six lattice sites. The total system remains in a pure state while local observables follow thermal distributions. Additionally, it was demonstrated that the entanglement entropy follows a near-volume law [37]. The same experiment illustrates that local observables follow thermal distributions and at the same time the total system is in a pure and hence non-thermal states. Experiments with only 5 ions were able to realize a large Hilbert space, out of reach for state-of-the-art exact diagonalization, where local spin measurements show the emergence of quantum statistical mechanics although the system is isolated [252].

6.3 Specific non-thermalizing systems

Certain systems haven been found to not show thermalization. Two specific cases are introduced in the following.

6.3.1 Integrable systems

The failure of thermalization has been demonstrated for integrable systems where the initial state totally defines the time evolution. A striking example was shown with strongly interacting atoms in a quasi 1D system. This interacting many-body system exhibited many periodic oscillations even though the involved particles collide more than a thousand times with each other [38]. One can introduce the generalized Gibbs ensemble where thermalization occurs in different individual subspaces, defined by conserved quantities but not for the total system [85, 253–255]. The dynamics after a sudden split of a 1D system exploit this non-equilibrium phase of matter which can be described by the superposition of several thermalized subsystems. [256, 257]. However, integrability is a very special property of a quantum system and can be broken with small extra terms in the Hamiltonian. Systems where integrability is broken with strong enough perturbation are expected to behave ergodic [5].

6.3.2 Anderson localization

Redistribution of particles, momentum and energy is typical during the process of thermalization. Hence systems which lack these abilities arouse particular interest. A very general phenomenon of localization by disordered potentials was first introduced by Anderson for non-interacting electrons [40]. Even after infinite time, information about the initial state remains local because details of the starting point are localized. Hence these system cannot be ergodic and interacting systems which still localize would constitute a new class of systems which do not thermalize on their own.

In 1958 Anderson proved that the tight binding hopping Hamiltonian with variable additional disorder exhibits a phase transition from conducting to insulating behavior [40], which was awarded the Nobel prize in Physics of 1977. This insulating phase is today often called Anderson localized phase. It was shown that under a small change of the disorder strength the eigenstates of the non interacting system change from extended states to localized states. Thus the structure of the initial state can remain even after infinite time. Later on, the absence of transport was explained with waves theories [258, 259].

For a diffusively spreading wave, the intensities of the scattered waves need to be added. However for a coherent scattering process the amplitudes are essential and addition of amplitudes with different signs leads to destructive interference, which may stop the propagation of the wave [260]. The Ioffe-Regel criterion describes that this destructive interference happens near the condition where the mean free path between scattering events is below the wavelength and thus the dephasing between both scattering position is small [261]. The initial proposal was developed for non interacting electrons and hence also for single electrons in the tight binding model with quantum hopping to neighboring positions in an infinite lattice with random on-site disorder. Within this model, eigenstates are all exponentially localized for even the smallest amount of disorder in one and two dimensions. In higher dimensions the localization depends on disorder strength and the energy. At lower disorder states above a certain energy, defining the mobility edge, are not localized and only after a critical disorder strength all states are localized. For localized states in any dimension, the wave functions $|\Psi(\boldsymbol{r})\rangle$ fall off exponentially for long distance $|\Psi(\boldsymbol{r})\rangle \sim \exp(-|\boldsymbol{r}-\boldsymbol{r}_0|/\xi)$, where ξ is the localization length. This length scale can depend on disorder as well as the energy of the state. It is also influenced by the properties of the disorder.

First experimental results with ultracold atoms were measured with disorder potentials created by speckle patterns [41] and quasiperiodic dichromatic lattices [42]. Both experiments were carried out in 1D and the expansion of a non-interacting BEC was characterized as a function of disorder and for the speckle pattern a diverging localization length approaching zero dis-

order was observed [41]. Further studies hinted at a delocalization due to interaction [45] and focused at the subdiffusive expansion [262]. Additionally the Anderson localized phase has been explored in 3D [263–265], which determined the influence of temperature, disorder amplitude and disorder correlation length.

A wide range of results has been published on exploration of the influence of different experimental parameters. These experiments explored for example different dimensionality where the mobility edge became visible in 3D and directly measured the localization length in 1D systems. Two kinds of disorder pattern were used. Either quasi-disorder was created with two lattices overlapped with incommensurable wavelength or speckle patterns with a characteristic correlation length applied.

The wave formulation of the problem was directly experimentally tested with microwaves (1D) [266], ultrasound (3D) [267] and with light in one [268], two [269] and three dimensions [270, 271].

6.4 Many-body localization

Anderson localization has shown that disorder changes the dynamical behavior of a system and its characteristics significantly. Since the beginning of this topic, it was an exciting question how interactions, which transform these single-particle systems into a many-body system, affect this localization. This is especially interesting because it would define a new phase of matter which does not thermalize if the localization remains even for interacting many-body systems.

In general interaction enhances the probability of resonances as the Hilbert space is drastically increased.

Studies of the effect of electron-electron scattering with small energy transfer on Anderson localization marked the starting point of in-depth work on localization in interacting systems [272–274]. It was shown that interaction induced dephasing which can allow transport while still a localized phase exists. A second wave of theoretical studies started about 20 years later with the study of the phase transition between the insulating phase and a metallic phase [243, 275] applying perturbative arguments. Furthermore, it was shown that a many-body localized phase (MBL) exists for systems with a bounded spectrum for any interaction strength and energy density [276, 277]. This implies the breakdown of equilibrium statistical mechanics for certain generic macroscopic systems and triggered tremendous theoretical research [34, 39, 278]. Being their own heat bath, as proposed above as method for closed quantum system for thermalization, does not work for these systems. Also the previously described ETH fails for these specific systems [251].

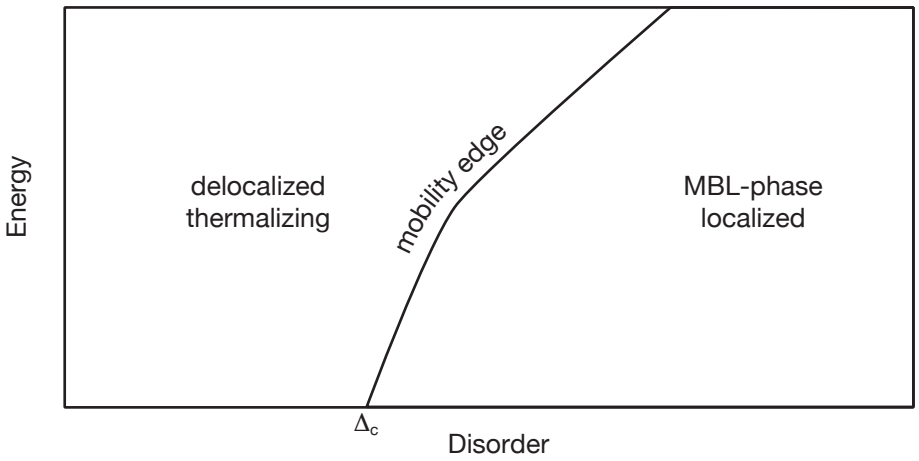

Figure 6.2: MBL phase diagram. Schematic representation with predicted mobility edge. Below the critical disorder strength Δ_c the system is ergodic and thus thermalizing. Beyond this point the system is localized and does not thermalize.

This leads to a memory of the initial state [39, 279]. Thus MBL might serve as an useful resource for quantum information technologies where information is robustly stored by disorder [245].

Within the full localized regime a complete set of quasi local integrals of motion (called l-bits) exists and all eigenstates are localized [280, 281]. These l-bits are only weakly interacting, which underlies the absence of particle transport, but allows the build up and spreading of phase correlations. The interaction of these l-bits decays exponentially with distance, which underlies the absence of particle transport, but allows a slow build up and spreading of phase correlations. This leads to a characteristic logarithmic growth of the entanglement entropy after a quantum quench, which is a key difference to Anderson localization [282–286]. It was proposed to measure this growth of entanglement with local spin echoes, so called DEER (double electron-electron resonance) interferometry [287]. For MBL even at low dimensionality a nonzero disorder strength is necessary to cross the phase transition, which is another distinction from the Anderson case [288, 289]. Further research has focused on the Bose glass phase for the ground state and predicted the phase diagram [290, 291].

The MBL transition is distinct from other phase transitions as all eigenstates change their properties and thus applies to all energies. This is visible in the energy level statistics of the eigenstates. Deep in the MBL phase, the statistics follow a Poisson distribution, whereas ergodic systems follow a Wigner Dyson distribution [287]. Thermal states maximize entropy and the

entanglement entropy scales with the volume, as it is an extensive property of a thermalized system. In contrast for MBL systems in steady state an area law scaling is predicted [292–294]. It is further predicted that mobility edges can exist even in low dimensions [243] and mobility edges where only high energy states are localized are conceivable [295].

MBL does not occur if sufficient strong coupling to a thermal bath is provided [39, 296]. This restores thermalization. Thus ions and ultracold quantum gases in optical lattices with their weak coupling to the outside world, are well suited to simulate and test MBL. So far ion experiments have been limited to short time scale and low particle number [251, 277, 297].

With an interacting Fermi gas exposed to a quasi-periodic lattice realizing the Aubry-André model, the phase diagram in 1D was mapped out [43] and it was observed that coupling of several identical 1D system introduces again thermalization [44]. At low energy densities, the Bose-glass phase was investigated, pointing out that interacting many-body systems can have zero conductivity [48, 50, 298]

After all this theoretical and experimental research, still little is known about the transition to this dynamical phase of matter itself and additional research on higher dimensions is necessary [299]. For localization, 1D systems are special as even rare localized regions can block conductivity whereas these regions can be bypassed in higher dimensions.

7 Many-body localization transition in two dimensions

In this chapter, we address the open question of the nature of a many-body localization transition in two dimensions. A theoretical introduction to this topic is found in Chapter 6.4. We observe experimentally this transition even at high mean energy per particle and provide a first characterization of the transition point. We report on the in-situ study of thermalization and transport in a 2D bosonic lattice with projected on-site disorder. By tracking the time evolution of an initially prepared density domain wall for variable disorder strengths, we reveal the sudden onset of non-thermalizating behavior above a critical value. The transition point is located at a disorder strength for which also the single-particle bandwidth, the on-site interaction and the energy density are all of comparable strength. This regime of parameters, being far from the disorder-dominated (classical) [300] and the interaction-dominated limits (hard core bosons), is highly non-trivial from the theoretical perspective. Our results are compared to a prediction for the non-interacting model including the precise knowledge of the characterized disorder potential, highlighting the dramatic differences and pointing out the key role of interactions. We obtain strong indication for a diverging length scale when approaching the transition from the localized side by comparing the density profiles after time evolution with disorder potential to a thermalized reference sample developed in a disorder-free system.

7.1 Experimental procedure

We began our experiments by preparing a two-dimensional approximately unity filled Mott insulator (See Chapter 3.1 and 3.2 for details). Thereafter, we removed the right half of the atomic population using the single-site addressing technique (See Chapter 3.5) such that approximately $N = 125(11)$ atoms remained in the lattice sites located at $x < 0$, thus preparing a sharp density domain wall oriented along the y-direction. It should be noted that the initial domain wall state is very special as due to the relative fast quench in lattice depth, the initial interaction energy is nearly zero (no double occupation) but due to the distribution in the trap, the state possesses a con-

siderable amount of potential energy compared to a state positioned symmetrically around the trap center. Additionally, the initial state occupies all momentum states because the atoms are strongly localized. The computer-generated random disorder pattern was projected onto the atoms (See Chapter 3.5.4) while the atoms were fixed. Here, no relocation of density occurs and hence there is no screening of the disorder potential in the initial state. The dynamics of the initial domain wall was then initiated by lowering the x and y lattice depth to $12\,\mathrm{E_r}$ in 5 ms, which is less than one tunneling time. We allowed the system to evolve for a variable time t in the low lattice potential with variable disorder strength after which the local parity projected density was measured (Chapter 3.3.1).

7.2 Physical system

During the dynamics, the system is described by the two-dimensional Bose-Hubbard Hamiltonian with on-site disorder as written in Formula 2.1. The harmonic trapping potential $V_i = m(a_{\mathrm{lat}}^2\omega_x^2 i_x^2 + \omega_y^2 i_y^2)/2$ was determined separately. The frequencies $(\omega_x,\omega_y) = 2\pi \times (54,60)$ Hz in x and y direction were measured for this experimental configuration by tracking the oscillation of deflected BECs.

The nearest-neighbor hopping strength at a lattice depth of $12\,E_r$ is $J/h = 24.8$ Hz (without density correction) corresponding to a tunneling time of $\tau = h/2\pi J = 6.4$ ms, and longer range hopping terms are neglected as they are exponentially suppressed (See Chapter 3.2.2). The on-site interaction strength is $U = 24.4\,J$. The amplitude of the on-site disorder potential is denoted as Δ which describes the full width at half maximum of the disorder distribution. For these parameters, in the absence of disorder, the system's ground state is in the Mott insulating phase where the total lower band is filled. This configuration is close to the phase transition where strong particle hole fluctuations are visible [13] which ensures that the interactions are not sufficient to effectively describe the system by hard core bosons.

A ultra cold quantum gas system is very well isolated from its environment but still experiences a small residual coupling to external heat sources. During our experiments we noticed that the lifetime of the atom clouds is very sensitive to a well functioning lattice intensity stabilization, which we identified as one of the major sources of heating. The heating rate of the many-body system depends on the spectral characteristics of the noise and the many-body system and is difficult to predict. To estimate the energy increase during the evolution time, we measured the heating rate at $12\,E_r$ lattice depth assuming decoupling of the lattice sites (atomic limit) [10]. The decoupling assumption might lead to a small overestimation of the mean energy

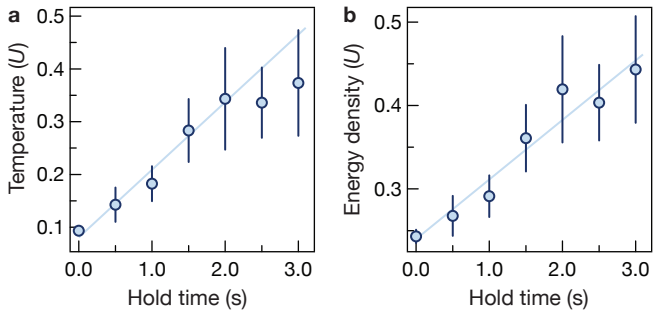

Figure 7.1: Heating of a Mott insulator. a, Temperature and **b,** corresponding energy density of an initially approximately unity filled Mott insulator for various hold times. The solid lines are linear fits to the data and the error bars are one standard deviation of the mean.

per site of up to $0.14\,U$ (half the lattice bandwidth) due to the ignored quantum mechanical particle-hole fluctuations present in the system which can be up to $2\,J$. As shown in Fig. 7.1, the temperature and energy density increased approximately linearly up to 2 s. The heating rate was obtained by a linear fit, which yielded $\dot{T} = 0.11(2)\,U/s$ and a corresponding rate for the energy density $\dot{E}/N = 0.09(3)\,U/s$. Here, $U = h \times 601\,\mathrm{Hz}$ is the on-site interaction energy for $12\,E_r$ lattice depth. This heating rate estimate was measured close to the superfluid – Mott insulator transition point, where the system is most susceptible to external noise as all three lattice lasers are in use and the low frequency excitation spectrum should have only a small gap. Thus, we expect it to be an upper bound for the coupling to external noise sources in the case of non-vanishing disorder.

7.3 Thermalization in disorder-free lattice

We started our experimental observation by tracking the evolution of the prepared domain wall without any disorder potential applied. Already the bare images shown in Figure 7.2 help to visualize that the initially prepared density step is smeared out after a few tens of tunneling times τ and after longer time no information about the initial density step remains. We checked that within the measurement uncertainty the density distribution does not change if a homogeneous box potential is applied and if the time evolution is started with different rotations of the initial domain wall state. The observed density distribution appears thermal and we extracted an upper limit of the temperature of $T < 0.54(1)\,U/k_B$, where k_B is the Boltzmann constant [10]. Here we are neglecting quantum fluctuations at $12\,E_r$, that is, assuming decoupled

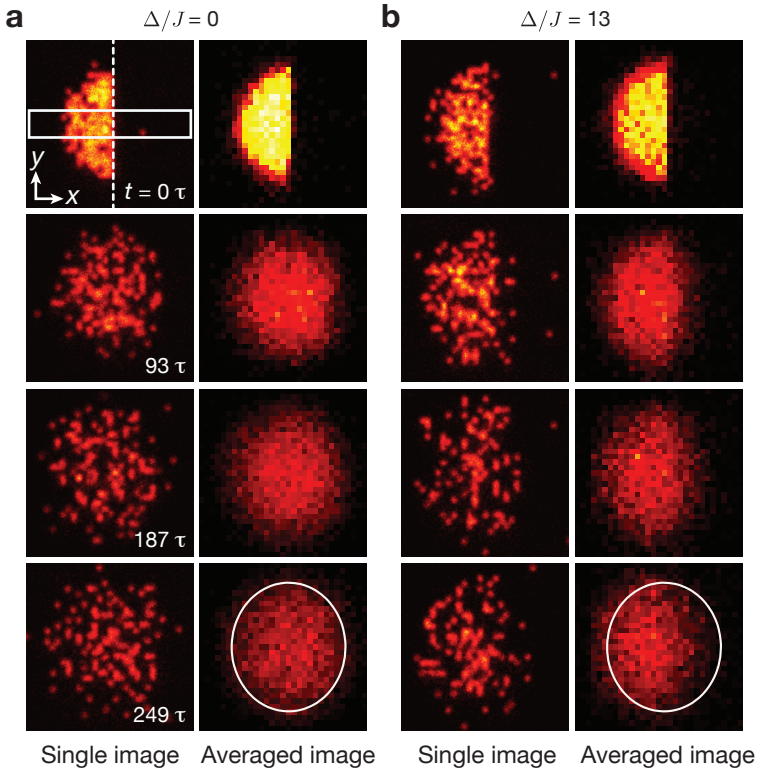

Figure 7.2: Single and averaged images. **a**, raw fluorescence images (red to yellow corresponds to increasing detected light level) showing the evolution of the initial density step without disorder. The left column shows single images (isolated red dots are individual atoms) of the parity projected atomic distribution for the indicated evolution times. The right column displays the mean density distribution averaged over 50 different disorder potentials. The top most picture is the initial state for which the analysis region ($dx \times dy = 5 \times 31$) is indicated by the white box. For the high disorder case shown in **b** the detected initial state filling is slightly lower, which is an artifact of the parity projection. Distinct to **b**, traces of the initial state remain for all times in the disordered case. The white guide lines in the averaged density profiles after $t = 249\,\tau$ highlight the difference.

sites, which is feasible as the interaction strength is the lowest involved energy scale and is negligible to first order.

The corresponding energy per particle of $E_T/N = 0.58(1)\,U$ agrees with the expectation for a thermalized state. Here, the energy density of the initial out-of-equilibrium state contributes with $E_0/N = 0.28(3)\,U$, determined by the initial thermal energy ($T \sim 0.15\,U$), the potential energy in the harmonic trap with frequency ω_x and the heating during the 2 s evolution time

($E_H/N = 0.18(6)\,U$) is considered.

7.4 Disorder induced non-thermal behavior

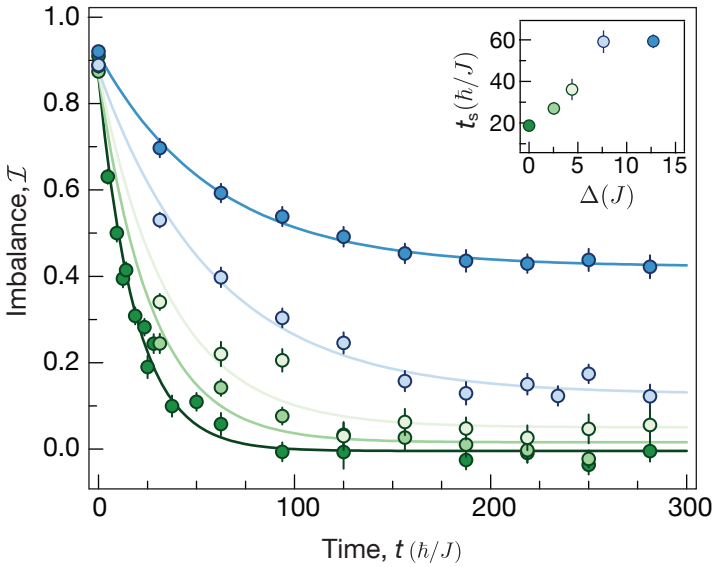

Figure 7.3: Relaxation dynamics of a density domain wall. The evolution of the imbalance $\mathcal{I}$ traced for five different disorder strengths $\Delta/J = 0$ (dark green), 3 (medium green), 4 (light green), 8 (light blue) and 13 (dark blue) displays a saturation behavior towards a quasi steady-state for all disorder strengths. For low disorders (green curves) the asymptotic value of the imbalance vanishes, while a finite imbalance remains for higher disorder (blue). The solid lines are fits to the data with $\mathcal{I} = \mathcal{I}_0 \exp(-t/t_s) + \mathcal{I}_\infty$, of which the decay time t_s is plotted versus disorder strength Δ in the inset. Error bars are one standard deviation of the mean in the main figure and 95% confidence bounds of the fit parameters in the inset.

On the contrary, repeating the measurement with strong disorder, traces of the initial shape remain and the system does not relax to a spatially symmetric density distribution expected for thermal state (see Figure 7.3). This is a direct mark of the failure of thermalization. A direct and model free quantity to identify a non-symmetric state is the density asymmetry quantified by a nonzero left (N_L) and right (N_R) atom number imbalance

$$\mathcal{I} = \frac{N_L - N_R}{N_L + N_R}, \tag{7.1}$$

which we analyze, as all other extracted quantities, in a central region of interest extending over 5 lattice sites in the y-direction. This asymmetry measurement is used to quantify the thermalization of the cloud. The zero line $x = 0$, separating left and right, is defined by the position of the initial density step. It was precisely aligned to the closest lattice site to the trap center resulting in an offset of up to ± 1 lattice sites, corresponding to $\mathcal{I} \pm 0.05$. The evolution of the imbalance, see Figure 7.3, confirms that for all disorder strengths the system reaches a quasi steady state within at most $150\,\tau$. For small disorder strengths we find a vanishing imbalance, which we consider as thermalizing regime. While for large disorder a nonzero imbalance remains even for long evolution times. We interpret this latter regime as the many-body localized phase, where the observed quasi steady-state is clearly non-thermal and transport through the system is blocked. The relaxation time t_s, extracted by an exponential fit to the data, increases with disorder strength and shows hints of saturation in the non-thermal regime (see Figure 7.3). We now turn to a series of measurements where we fix the evolution time to approximately $190\,\tau$, which is well in the quasi steady-state regime but short enough to keep the deposited energy due to laser noise and photon scattering small. On this timescale, we also expect the effects of low frequency noise on the disordered system to be small. Considering the measured heating rate in the non-disordered system as an upper bound for the energy increase, the energy per particle would change by only approximately 10% within one relaxation time t_s. Small couplings with the environment might possibly lead to relaxation of the quasi steady-state on timescales much longer than our experimental time scale [296, 301–303].

7.5 Identifying the transition point

The transition from vanishing to nonzero imbalance $\mathcal{I}_\infty$ for large disorder indicates the presence of a thermalizing phase for low disorder strengths and a clear transition to a localized phase at higher disorder. In order to locate many-body localization transition in our system, we recorded a series of measurements with fixed evolution time in the quasi steady-state regime and scanned the disorder around the critical value so that the position of many-body localization transition is narrowed down, see Figure 7.4. A fairly sharp onset of nonzero imbalance at a disorder strength $\Delta_{c,\mathcal{I}} = 5.5(4)\,J$ was extracted from a simple double linear fit

$$\mathcal{I}(\Delta) = \mathcal{I}_0 + \mathcal{I}_1 \cdot \max[(\Delta - \Delta_{c,\mathcal{I}}), 0] \tag{7.2}$$

with $\Delta/J \in [0{,}8]$. In the vicinity of the transition, slow sub-diffusive transport has been predicted [288, 289, 304–306]. This suggests that our hold time

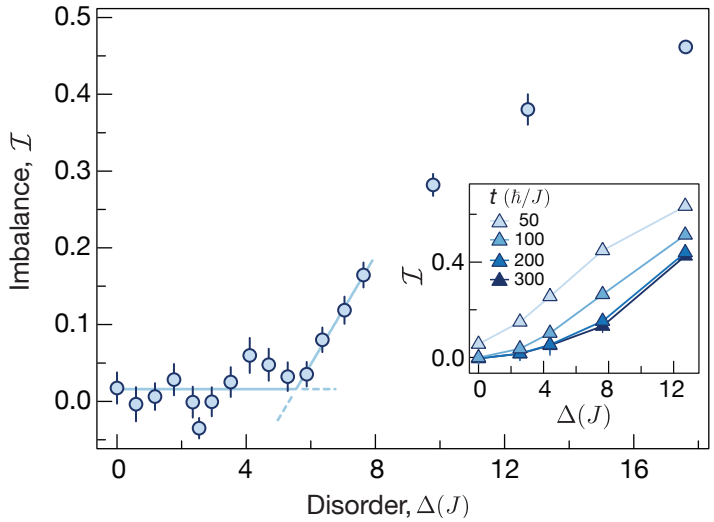

Figure 7.4: Identifying the MBL transition by the imbalance signal. Disorder dependence of the imbalance after equilibration of the dynamics.The data shows a sharp onset of nonzero quasi steady-state imbalance $\mathcal{I}$ at a disorder strength of $\Delta_{c,\mathcal{I}} = 5.5(4)\,J$ and the solid line is a double linear fit described in the text to extract the critical disorder. The inset illustrates the sharpening of the transition versus time and demonstrates the saturation of its shape by showing the imbalance extracted from the fits in Figure 7.3 at different evolution times.

is too short and the system has not reached a true steady state in this regime. It is possible that if we were able to study much longer hold times, the sharp onset might move towards stronger disorder. However, the data presented in Fig. 7.3 strongly suggests that the density distribution, to good approximation, reached its steady state, such that we only expect to slightly underestimate the transition point if no second important time scale is involved.

The imbalance indicates the symmetry of the density distribution with respect to the initial position of the domain wall which is in good agreement the trap center. An other quantitative observable determining the amount of thermalization is constructed from local comparison of the measured density profiles with the equilibrated thermal profile observed at vanishing disorder. In Figure 7.5, we use this method as a sensitive probe to detect deviations from the thermal profile by calculating the root mean square deviation

$$\delta n = \sqrt{\sum_i \left(n_i(0) - n_i(\Delta)\right)^2} \tag{7.3}$$

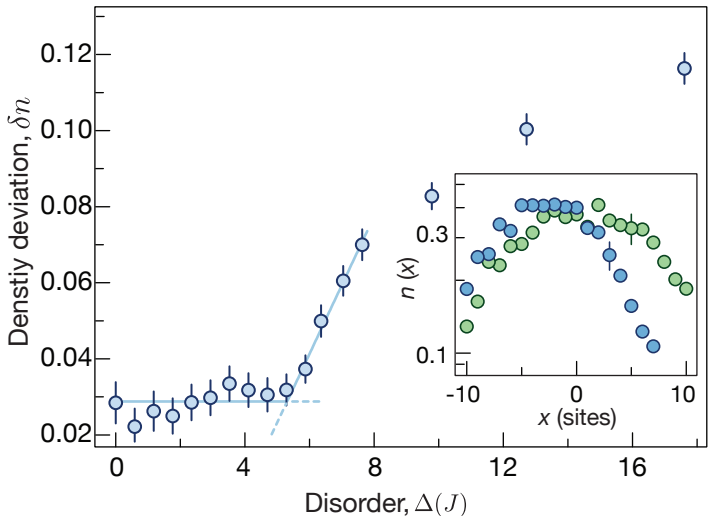

Figure 7.5: Identifying the MBL transition by the density difference signal. Deviation from the zero disorder thermal profile measured by the root-mean-square density difference δn at various disorder strengths. The relaxed density profiles differ by more than the random position induced measurement noise from the thermal profile abruptly above the critical disorder strength $\Delta_{c,\delta n} = 5.3(2)\,J$. The inset shows the averaged reference density profile for zero disorder (green) and the averaged profile at a high disorder of $\Delta = 13\,J$ (blue).

of the vertically (y-direction) averaged reference profile

$$n_i(0) = \frac{1}{5}\sum_{j=-2}^{2} n_{i,j}(0) \tag{7.4}$$

and the finite disorder profiles $n_i(\Delta)$. We observe that the profiles start to deviate significantly from the thermal profile at $\Delta_{c,\delta n} = 5.3(2)\,J$ with a fairly sharp kink signaling the transition, which is quantitatively consistent with the imbalance measurements. The transition point was determined here with the same double linear fit as for the imbalance data.

While in the non-interacting case, localization is predicted for vanishingly small disorder strength, the finite interaction U in our system promotes thermalization. This is consistent with our observation of a thermal behavior at non-zero Δ. However, as the disorder strength is increased above a critical value, the localization is restored, which is remarkable, especially from the fact that this transition takes place in the regime where the disorder Δ, the interaction U, and the single particle bandwidth $8\,J$ are comparable. The percolation limit in two dimensions is given by the number of accessible

bonds [307] and occurs if less than 50 % are accessible. Thus the mean energy per particle needs to be lower than 50 % of the next neighbor energy difference [300]. Classical localization would therefor happen at disorder strength approximately twice the mean energy per particle, much higher than the measured critical disorder strength.

7.6 Decay length

The MBL phase transition is expected to be a continuous transition [251, 288, 289, 293, 308] for which one expects a characteristic diverging length scale when approaching the transition. We determine the steady state decay length $\xi(\Delta)$ of the initially prepared density step from our single-site resolved measurements. This observable is directly related to a density-density correlation length. In order to minimize the influence of the external trap on the density profile, we reference the density profile $n_i(\Delta)$ to the thermal profile $n_i(0)$ by calculating

$$\bar{n}_i(\Delta) = n_i(\Delta)/n_i(0) \tag{7.5}$$

This division is based on the simple assumption that the density distribution of the localized phase follows the trap profile multiplied by an additional decay. Three examples are sown in Figure 7.6. The observed decay is found to be well captured by an exponential fit

$$\bar{n}_i(\Delta) \sim e^{-\lambda(\Delta)i} \tag{7.6}$$

with a disorder dependent decay constant $\lambda(\Delta) = 1/\xi(\Delta)$. In theoretical calculations on one dimensional fermionic systems, this exponential decay has been seen as well [299]. A priori, we would have expected a crossover from a interaction dominated decay behavior to a single particle localization dominated decay at low densities present at the outer edge of our sample, however, within the experimental uncertainty we cannot identify such an effect.

The decay constant $\lambda(\Delta)$ shows a very sharp kink at $\Delta_{c,\lambda} = 5.3(3)\,J$, marking the onset of the localized region. When approaching the transition from the localized side, the corresponding decay length $\xi(\Delta)$ diverges at this point, see Figure 7.6.

We empirically obtain this critical disorder $\Delta_{c,\lambda}$ using the bilinear fit function, $\lambda(\Delta) = \lambda_0 + \lambda_1 \cdot \max[(\Delta - \Delta_{c,\lambda}),0]$ with $\Delta/J \in [0,8]$. Here we limited the fit range to values not much above the visually apparent transition point because the bilinear model cannot accurately describe the system and is only seen as approximation.

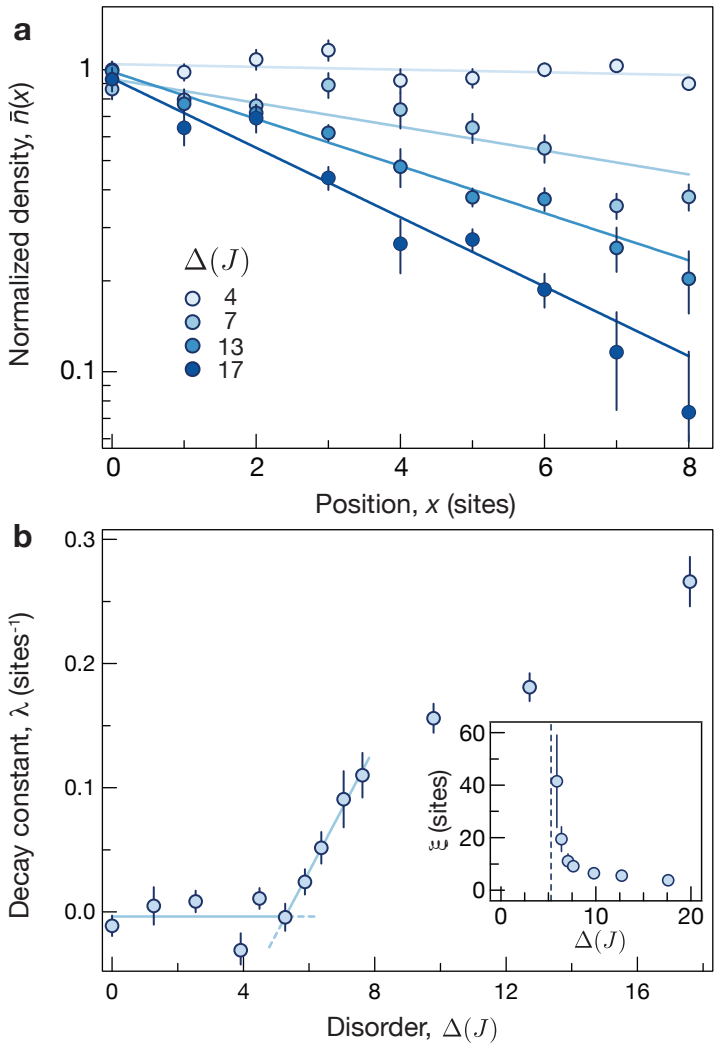

Figure 7.6: Diverging density decay length at the localization transition. a, spatial dependence of the normalized average density $n(\Delta)/n(0)$ in the initially empty region is fitted by an exponentially decaying model (solid lines). The blue brightness encodes the disorder strength increasing from light to dark: $\Delta/J = 4$, 7, 13 and 17. **b**, fitted decay constant λ as a function of disorder strength Δ. The solid light blue line is a double linear fit described in the text to locate the transition point $\Delta_{c,\lambda} = 5.3(2)J$. The inset shows the diverging decay length $\xi = 1/\lambda$ near the critical disorder strength. Error bars are one standard deviation of the mean in **a** and 95% confidence bounds of the fit parameters in **b**.

We emphasize, that all three methods to extract the critical disorder strength of the MBL transition in the experiments agree within the fit errors.

7.7 Interaction shift

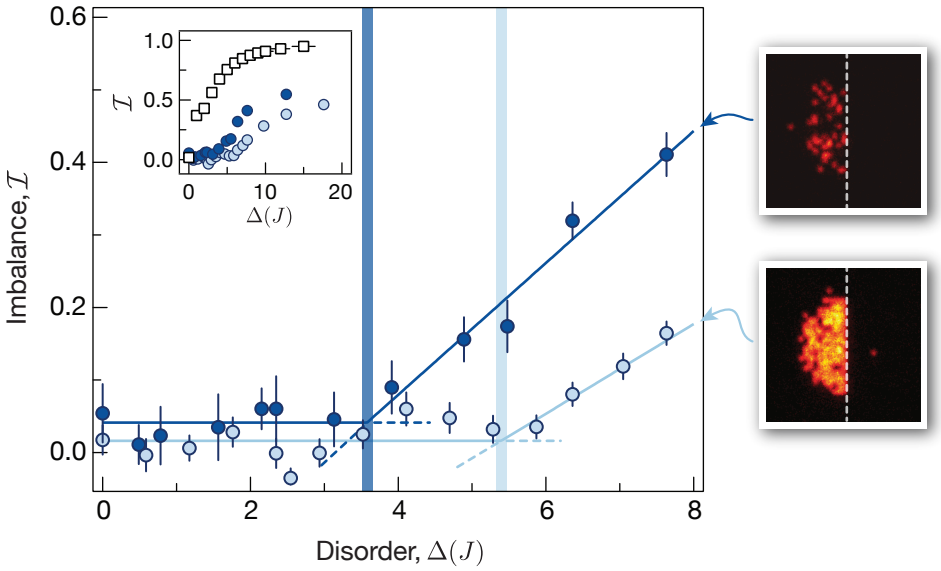

Figure 7.7: Interaction dependence of the localization transition. Quasi steady state imbalance $\mathcal{I}$ versus disorder strength Δ for different initial densities. The interaction effects are reduced by lowering the initial filling to 0.23, which is 25% of the value previously discussed in Figures 7.4 and 7.5 (light blue). The clear difference in critical disorder strengths highlights the strong influence of interactions on the localization. The right two insets show representative fluorescence images of the initial density distribution for each case. The left inset is a zoomed out view of the main figure where we added the results of exact diagonalization numerics for the non-interacting system with the same experimental conditions (black open squares). Here, the horizontal error bars denote the systematic uncertainty in the disorder strength. Vertical error bars are one standard deviation of the mean.

It is not possible to utilize a Feshbach resonance to change the interaction strength in order to experimentally verify that the observed behavior of the system is dominated by interactions. However a similar result can be obtained by reduced the initial density and therefore the effects of the interaction on the dynamics while keeping the initial energy per particle E_0/N constant. Note that the initial state has nearly no interaction energy as there is hardly any double occupation. Lower atomic densities are obtained by uniformly transferring a given fraction of the atoms by applying a microwave pulse to another hyperfine state and subsequently optically removing the transferred population. This technique removes the atoms at random positions. When reducing the density by a factor of four, we observe a clear shift

of the localization transition towards lower disorder strength as is expected, see Figure 7.7. Here, the left-right imbalance $\mathcal{I}(\Delta)$ displays a sharp transition behavior at a smaller critical disorder of $\Delta_{c,\mathcal{I}} \simeq 3.6(2)\,J$. Furthermore, the numerical prediction for a non-interacting system obtained by exact diagonalization is fully incompatible and strongly differs from both measurements, showing that the interactions facilitate thermalization for low disorder strengths.

7.8 Size scaling

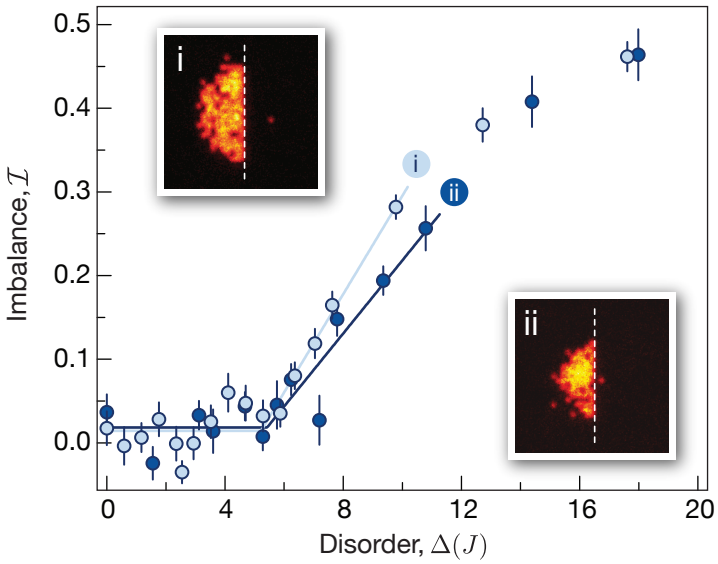

Figure 7.8: Localization transition for two system sizes. Imbalance $\mathcal{I}$ as function of disorder Δ for two different system sizes. We changed the initial radius of the Mott insulator from 9 (i, light blue) to 7 (ii, dark blue) lattice sites by tightening the external trap, but observed no change in the critical disorder strength. The insets show a representative fluorescence image of the initial density distribution for each case. Error bars are one standard deviation of the mean.

Additionally we check for finite size effects by studying the localization transition in a smaller system which did not use an extra blue detuned deconfinement beam. We reduced the initial atom number by 60% to $N = 75(10)$ and the radius of the initial Mott insulator shrunk from 9 to 7 sites. To keep the energy per particle E_0/N constant, we increased the trap frequency to $\omega_x = 2\pi \times 65\,\mathrm{Hz}$. As shown in Figure 7.8, there is no visible change in the

critical disorder extracted from the imbalance measurements. The fitted critical disorder for the small system is $\Delta_{c,\mathcal{I}} = 5.4(6)$, which is consistent with the value $\Delta_{c,\mathcal{I}} = 5.5(4)\,J$ found for the larger system. From these observations, we conclude that the nonzero critical disorder strength is due to the interactions, and that the measured critical disorder value is not strongly influenced by the small external driving due to laser fluctuations discussed above.

7.9 Summary

In conclusion, our experiments provide the first evidence for many-body localization at high energy in two dimensions by the observation of a transition from a thermalizing phase to a localized phase of interacting bosons in a disordered optical lattice. The system size analyzed in our experiment is far beyond numerically accessible scales, demonstrating a non-trivial quantum realization of the MBL system that challenges both analytical and numerical theory. Only recently, domain wall melting for fermions in 1D have been studied theoretically, pointing out that our method is indeed valid to probe the MBL transition [299]. Furthermore, we supplemented our observation of an MBL transition with the demonstration of a clear shift of the transition point for effectively smaller interaction energy. Even though it is difficult to distinguish a true phase transition from a sharp crossover within experiments, our results mark a first step in understanding many-body localization in more than one dimension, and can be extended to obtain detailed information about the nature of the MBL transition, such as its dynamical critical exponent [288, 289]. Furthermore, supplementing transport experiments with density-density correlation measurements offer a promising possibility to demonstrate ongoing phase dynamics in the localized phase while the density or charge transport is frozen [297, 309]. By detailed studies of the dynamics of transport it should also be possible to study Griffiths effects and sub-diffusive transport in the vicinity of the transition [288, 289, 304–306]. Besides dynamical properties our technique might allow to probe many-body eigenstate related properties, such as the local integrals of motion [280, 281] defined via local operators [308].

8 Conclusion and outlook

In this thesis different quantum systems have been successfully simulated with ultracold quantum gases to explore fundamental properties.

We studied out-of-equilibrium properties of ultracold Bosons confined in a single two dimensional plane of an optical lattice. Novel high resolution detection schemes allowed us to prepare and probe the many-body system at the level of a single site, with the creation of arbitrary potentials, local creation of a single impurity and the imaging of the spin resolved density.

At the beginning, we validated that the dynamics of a two-component gas described by the Bose-Hubbard model can be mapped to the Heisenberg model deep in the Mott insulating regime, where the second order exchange processes mimic next neighbor spin flips. Additionally, we extended the observations to the superfluid regime where this mapping fails and the measurements rather support an effective polaronic behavior. Starting from a Mott insulators with extremely low entropy together with local manipulations permit to tailor different initial states precisely.

We further investigated the case of two spin impurities initially located next to each other. Spin-spin interactions, which in our system are ferromagnetic, lead to the formation of magnon bound states, the basic building block of correlations in magnetism. We identified these states via in-situ measurements of spatial correlations revealing a slowing down of the bound state propagation.

A remarkable feature of such dynamics is the creation of entanglement during the ballistic propagation of the spin impurity. Thanks to the high fidelity of the initial state preparation and the use of the refined in-situ spin resolved measurements of Stern-Gerlach type, we probed two-site spin-spin correlations defining a lower bound of entanglement. We observed the propagation of an entanglement wave and demonstrated its fragility towards an increasing population of spin defects. In addition, these results demonstrate that ultracold quantum systems are well isolated from the environment and thus show coherent evolution.

We extended experiments on quantum magnetism to a higher energy range, where a well defined relative angle between neighboring spins was imprinted, resulting in an excited many-body spin state with a local twist of the spin vector. The studies on the relaxation of such an excited state towards an unpolarized gas have shown a strong dependence on the initial twist and the

dimensionality. Indeed, while the spin excitation relaxes diffusively in an one-dimensional spin chain, we found the two-dimensional analogue of this system to exhibit an anomalous superdiffusive behavior. It is revealed that these isolated quantum systems are their own heat bath leading to a relaxation to thermal states.

In a second set of experiments, we focused on the thermalization of a highly excited 2D interacting Bose gas released in a disordered potential. We investigated the nature of the many-body localization (MBL), an out-of-equilibrium state of matter breaking conventional thermodynamics as it is characterized by nonergodic time evolution. The time evolution of a half cut Mott-insulating state reveals several signatures of the transition of a thermalizing to localized system. Our different observables point to the same critical disorder strength. Utilizing the single-site resolution, the exponential decay of the density around the initial domain wall is identified which diverges at the phase transition point. We identify that the onset of the phase transition is strongly influenced by interaction as lower densities, corresponding to lower interaction energy, significantly shift the onset to lower values. For these experiments, we developed novel experimental techniques for high precision light pattern characterization which allowed us for the first time to directly measure the applied disorder potential experienced by the atoms.

We have given several examples how well controlled artificial quantum systems can be used for quantum simulation and fundamental research. Furthermore, the developed techniques of high precision single site detection and manipulation are also useful for future experiments on quantum metrology and computation.

Our studies on spin and polaron dynamics bring within experimental reach several open questions on the topic of quantum magnetism. For instance, one can explore the melting of a spin domain wall in 1D or 2D and using the same protocol as the one used in the many-body-localization experiments.

In addition, many properties of many-body localization remain to be observed and pose a serious theoretical challenge that can be tackled in our setup. Specifically, one can probe the robustness of the phase by coupling a external bath to the system. Such a bath, could simply be a laser shone on the atomic sample destroying localization and thus restores thermalization. A thermal reservoir can also be realized by a fraction of the atoms themselves, as a consequence of the local potential at their specific position, feasible with the versatile control over the spatial disorder.

Following a recent proposal [309], higher moments of local density measurements can be combined to extract additional information about the many-body localized state. The obtained information is related to the entanglement

entropy of the system, which is predicted to show an MBL specific logarithmic growth with time. The initial state preparation as well as the detection process which are proposed in this publication are feasible for the existing setup.

Furthermore, a quantum Griffiths phase is predicted in the vicinity of the many-body localization transition, which leads to slow subdiffusive transport [305]. As mentioned in the publication, it is unclear if this phase exists only in one dimension where transport can be stopped by any insulating region. Experiments can first validate the existence of this phase in 1D and extend thereafter the experiments to 2D systems to either show the existence of this phase or characterize its fragility.

The precise control over the disorder potential can also be used to spatially connect MBL and thermal regions and study the emerging properties. This realization and similar experiments like local photon scattering provide interesting tools to investigate the robustness of the MBL phase.

The combination of the on-site interaction with the long-range Rydberg interaction will be a long term goal and can lead to interesting research for both topics, quantum magnetism and the breakdown of thermalization currently only investigated for short range interaction.

The large flexibility of the experimental system allows to largely extend the capabilities with only small additional changes. The system size of the 2D clouds is limited by the confinement created by the tightly focused lattice laser beam needed to reach the necessary deep lattice potentials for the fluorescence imaging. Recent experiments have demonstrated single-site resolved imaging with Raman side-band cooling [23, 24, 310, 311]. This technology allows the use of shallower lattices during imaging which permits to increase the beam sizes and hence the confinement will be lower for the same lattice depth. Larger systems will avoid results limited by finite size or can be measured for different system sizes to extract the finite size scaling. As an example, the many body decay length can be measured over a large distance, which can show deviations from a pure exponential decay as the density decreases and at the same time reduces the interaction strength. In general, observables will be less distorted by the trap as a more homogeneous chemical potential is present. Especially the investigation of 1D systems will benefit from larger systems, because on the one hand the system size was small in the previous 1D experiments and on the other hand this increases the number of parallel 1D systems under investigation, increasing the data rate. The limit of strong interaction in 1D, the Tonks-Girardeau gas, is reachable with a weaker confinement because the density is decreased for the same number of particles which increases the effective interactions in 1D.

Another significant improvement can be achieved by extending the Stern-Gerlach type spin detection to the third direction. Indeed, the knowledge

of the full statistics of empty sites and atoms of both spin states is essential to study spin correlations. This is relevant for many of the aforementioned topics, from the polaronic case, where an impurity is coupled to bath, to the meltdown of a magnetic domain wall and the self formation of ferromagnetic domains.

Further research of quantum magnetism would benefit from an additional superlattice, which allows to create ladder systems with an effective dimensionality between 1D and 2D or effective larger spin states. A superlattice is furthermore an additional tool to prepare initial states and to implement detection methods suited for the measurement of challenging observables such as entanglement entropy [125].

Bibliography

1. Lewenstein, M. *et al. Ultracold atomic gases in optical lattices: mimicking condensed matter physics and beyond*. Adv. Phys. **56,** 243–379 (2007).
2. Bloch, I., Dalibard, J. & Nascimbène, S. *Quantum simulations with ultracold quantum gases*. Nat. Phys. **8,** 267–276 (2012).
3. Georgescu, I. M., Ashhab, S. & Nori, F. *Quantum simulation*. Rev. Mod. Phys. **86,** 153–185 (2014).
4. Feynman, R. P. *Simulating physics with computers*. Int J Theor Phys **21,** 467–488 (1982).
5. Polkovnikov, A., Sengupta, K., Silva, A. & Vengalattore, M. *Colloquium : Nonequilibrium dynamics of closed interacting quantum systems*. Rev. Mod. Phys. **83,** 863–883 (2011).
6. Bethe, H. *Zur Theorie der Metalle*. Z. Physik **71,** 205–226 (1931).
7. Anderson, M. H., Ensher, J. R., Matthews, M. R., Wieman, C. E. & Cornell, E. A. *Observation of Bose-Einstein Condensation in a Dilute Atomic Vapor*. *Science* **269,** 198–201 (1995).
8. Davis, K. B. *et al. Bose-Einstein Condensation in a Gas of Sodium Atoms*. Phys. Rev. Lett. **75,** 3969–3973 (1995).
9. Greiner, M., Mandel, O., Esslinger, T., Hänsch, T. W. & Bloch, I. *Quantum phase transition from a superfluid to a Mott insulator in a gas of ultracold atoms*. *Nature* **415,** 39–44 (2002).
10. Sherson, J. F. *et al. Single-atom-resolved fluorescence imaging of an atomic Mott insulator*. *Nature* **467,** 68–72 (2010).
11. Bakr, W. S., Gillen, J. I., Peng, A., Fölling, S. & Greiner, M. *A quantum gas microscope for detecting single atoms in a Hubbard-regime optical lattice*. *Nature* **462,** 74–77 (2009).
12. Bakr, W. S. *et al. Probing the Superfluid–to–Mott Insulator Transition at the Single-Atom Level*. *Science* **329,** 547–550 (2010).
13. Endres, M. *et al. Observation of Correlated Particle-Hole Pairs and String Order in Low-Dimensional Mott Insulators*. *Science* **334,** 200–203 (2011).
14. Cheneau, M. *et al. Light-cone-like spreading of correlations in a quantum many-body system*. *Nature* **481,** 484 (2012).

15. Weitenberg, C. *et al. Single-spin addressing in an atomic Mott insulator*. *Nature* **471,** 319–324 (2011).

16. Simon, J. *et al. Quantum simulation of antiferromagnetic spin chains in an optical lattice*. *Nature* **472,** 307–312 (2011).

17. Preiss, P. M. *et al. Strongly correlated quantum walks in optical lattices*. *Science* **347,** 1229–1233 (2015).

18. Bakr, W. S. *et al. Orbital excitation blockade and algorithmic cooling in quantum gases*. *Nature* **480,** 500–503 (2011).

19. Preiss, P. M., Ma, R., Tai, M. E., Simon, J. & Greiner, M. *Quantum gas microscopy with spin, atom-number, and multilayer readout*. Phys. Rev. A **91,** 041602 (2015).

20. Miranda, M., Inoue, R., Okuyama, Y., Nakamoto, A. & Kozuma, M. *Site-resolved imaging of ytterbium atoms in a two-dimensional optical lattice*. Phys. Rev. A **91,** 063414 (2015).

21. Yamamoto, R., Kobayashi, J., Kuno, T., Kato, K. & Takahashi, Y. *An ytterbium quantum gas microscope with narrow-line laser cooling*. New J. Phys. **18,** 023016 (2016).

22. Omran, A. *et al. Microscopic Observation of Pauli Blocking in Degenerate Fermionic Lattice Gases*. Phys. Rev. Lett. **115,** 263001 (2015).

23. Cheuk, L. W. *et al. Quantum-Gas Microscope for Fermionic Atoms*. Phys. Rev. Lett. **114,** 193001 (2015).

24. Parsons, M. F. *et al. Site-Resolved Imaging of Fermionic* ^{6}Li *in an Optical Lattice*. Phys. Rev. Lett. **114,** 213002 (2015).

25. Haller, E. *et al. Single-atom imaging of fermions in a quantum-gas microscope*. Nat Phys **11,** 738–742 (2015).

26. Edge, G. J. A. *et al. Imaging and Addressing of Individual Fermionic Atoms in an Optical Lattice*. Phys. Rev. A **92** (2015).

27. Boll, M. *et al. Spin- and Density-Resolved Microscopy of Antiferromagnetic Correlations in Fermi-Hubbard Chains*. **353,** 1257–1260 (2016).

28. Parsons, M. F. *et al. Site-Resolved Measurement of the Spin-Correlation Function in the Fermi-Hubbard Model*. **353,** 1253–1256 (2016).

29. Cheuk, L. W. *et al. Observation of Spatial Charge and Spin Correlations in the 2D Fermi-Hubbard Model* (2016).

30. Mitra, D., Brown, P. T., Schauß, P., Kondov, S. S. & Bakr, W. S. *Phase Separation and Pair Condensation in a Spin-Imbalanced 2D Fermi Gas*. Phys. Rev. Lett. **117,** 093601 (2016).

31. *Quantum Magnetism* (eds Schollwöck, U., Richter, J., Farnell, D. J. J. & Bishop, R. F.) (Springer Berlin Heidelberg, Berlin, Heidelberg, 2004).
32. Trotzky, S. *et al. Time-Resolved Observation and Control of Superexchange Interactions with Ultracold Atoms in Optical Lattices*. *Science* **319,** 295–299 (2008).
33. Kim, K. *et al. Entanglement and Tunable Spin-Spin Couplings between Trapped Ions Using Multiple Transverse Modes*. Phys. Rev. Lett. **103,** 120502 (2009).
34. Eisert, J., Friesdorf, M. & Gogolin, C. *Quantum many-body systems out of equilibrium*. Nat Phys **11,** 124–130 (2015).
35. Trotzky, S. *et al. Probing the relaxation towards equilibrium in an isolated strongly correlated one-dimensional Bose gas*. Nat. Phys. **8,** 325–330 (2012).
36. Langen, T., Geiger, R., Kuhnert, M., Rauer, B. & Schmiedmayer, J. *Local emergence of thermal correlations in an isolated quantum many-body system*. Nat Phys **9,** 640–643 (2013).
37. Kaufman, A. M. *et al. Quantum Thermalization through Entanglement in an Isolated Many-Body System*. **353,** 794–800 (2016).
38. Kinoshita, T., Wenger, T. & Weiss, D. S. *A quantum Newton's cradle*. *Nature* **440,** 900–903 (2006).
39. Nandkishore, R. & Huse, D. A. *Many-Body Localization and Thermalization in Quantum Statistical Mechanics*. Annu. Rev. Condens. Matter Phys. **6,** 15–38 (2015).
40. Anderson, P. W. *Absence of Diffusion in Certain Random Lattices*. Phys. Rev. **109,** 1492–1505 (1958).
41. Billy, J. *et al. Direct observation of Anderson localization of matter waves in a controlled disorder*. *Nature* **453,** 891–894 (2008).
42. Roati, G. *et al. Anderson localization of a non-interacting Bose–Einstein condensate*. *Nature* **453,** 895–898 (2008).
43. Schreiber, M. *et al. Observation of many-body localization of interacting fermions in a quasirandom optical lattice*. *Science* **349,** 842–845 (2015).
44. Bordia, P. *et al. Coupling Identical one-dimensional Many-Body Localized Systems*. Phys. Rev. Lett. **116,** 140401 (2016).
45. Deissler, B. *et al. Delocalization of a disordered bosonic system by repulsive interactions*. Nat Phys **6,** 354–358 (2010).
46. Pasienski, M., McKay, D., White, M. & DeMarco, B. *A disordered insulator in an optical lattice*. Nat Phys **6,** 677–680 (2010).
47. Gadway, B., Pertot, D., Reeves, J., Vogt, M. & Schneble, D. *Glassy Behavior in a Binary Atomic Mixture*. Phys. Rev. Lett. **107,** 145306 (2011).

48. Tanzi, L. *et al. Transport of a Bose Gas in 1D Disordered Lattices at the Fluid-Insulator Transition*. Phys. Rev. Lett. **111,** 115301 (2013).

49. D'Errico, C. *et al. Observation of a Disordered Bosonic Insulator from Weak to Strong Interactions*. Phys. Rev. Lett. **113,** 095301 (2014).

50. Meldgin, C. *et al. Probing the Bose glass-superfluid transition using quantum quenches of disorder*. Nat Phys **advance online publication** (2016).

51. Bloch, I. *Ultracold quantum gases in optical lattices*. Nat Phys **1,** 23–30 (2005).

52. Verkerk, P. *et al. Dynamics and spatial order of cold cesium atoms in a periodic optical potential*. Phys. Rev. Lett. **68,** 3861–3864 (1992).

53. Weidemüller, M., Hemmerich, A., Görlitz, A., Esslinger, T. & Hänsch, T. W. *Bragg Diffraction in an Atomic Lattice Bound by Light*. Phys. Rev. Lett. **75,** 4583–4586 (1995).

54. Hemmerich, A., Weidemüller, M., Esslinger, T., Zimmermann, C. & Hänsch, T. *Trapping Atoms in a Dark Optical Lattice*. Phys. Rev. Lett. **75,** 37–40 (1995).

55. Raithel, G., Birkl, G., Kastberg, A., Phillips, W. D. & Rolston, S. L. *Cooling and Localization Dynamics in Optical Lattices*. Phys. Rev. Lett. **78,** 630–633 (1997).

56. Müller-Seydlitz, T. *et al. Atoms in the Lowest Motional Band of a Three-Dimensional Optical Lattice*. Phys. Rev. Lett. **78,** 1038–1041 (1997).

57. Hamann, S. E. *et al. Resolved-Sideband Raman Cooling to the Ground State of an Optical Lattice*. Phys. Rev. Lett. **80,** 4149–4152 (1998).

58. Auerbach, A. *Interacting Electrons and Quantum Magnetism* 249 pp. (Springer Science & Business Media, 2012).

59. Jaksch, D., Bruder, C., Cirac, J. I., Gardiner, C. W. & Zoller, P. *Cold Bosonic Atoms in Optical Lattices*. Phys. Rev. Lett. **81,** 3108–3111 (1998).

60. Capogrosso-Sansone, B., Kozik, E., Prokof'ev, N. & Svistunov, B. *On-site number statistics of ultracold lattice bosons*. Phys. Rev. A **75,** 013619 (2007).

61. Altman, E., Hofstetter, W., Demler, E. & Lukin, M. D. *Phase diagram of two-component bosons on an optical lattice*. New J. Phys. **5,** 113 (2003).

62. Kuklov, A. B. & Svistunov, B. V. *Counterflow Superfluidity of Two-Species Ultracold Atoms in a Commensurate Optical Lattice*. Phys. Rev. Lett. **90,** 100401 (2003).

63. Duan, L.-M., Demler, E. & Lukin, M. D. *Controlling Spin Exchange Interactions of Ultracold Atoms in Optical Lattices*. Phys. Rev. Lett. **91,** 090402 (2003).
64. Auerbach, A. *Interacting Electrons and Quantum Magnetism* red. by Birman, J. L., Lynn, J. W., Silverman, M. P., Stanley, H. E. & Voloshin, M. (Springer New York, New York, NY, 1994).
65. Parkinson, J. B. & Farnell, D. J. J. *An Introduction to Quantum Spin Systems* 159 pp. (Springer Science & Business Media, 2010).
66. Heidrich-Meisner, F., Honecker, A. & Brenig, W. *Transport in quasi one-dimensional spin-1/2 systems*. Eur. Phys. J. Spec. Top. **151,** 135–145 (2007).
67. Sologubenko, A. V., Lorenz, T., Ott, H. R. & Freimuth, A. *Thermal Conductivity via Magnetic Excitations in Spin-Chain Materials*. J Low Temp Phys **147,** 387–403 (2007).
68. Chen, Y.-A. *et al. Controlling Correlated Tunneling and Superexchange Interactions with ac-Driven Optical Lattices*. Phys. Rev. Lett. **107,** 210405 (2011).
69. Porras, D. & Cirac, J. I. *Effective Quantum Spin Systems with Trapped Ions*. Phys. Rev. Lett. **92,** 207901 (2004).
70. Friedenauer, A., Schmitz, H., Glueckert, J. T., Porras, D. & Schaetz, T. *Simulating a quantum magnet with trapped ions*. Nat Phys **4,** 757–761 (2008).
71. Blatt, R. & Roos, C. F. *Quantum simulations with trapped ions*. Nat Phys **8,** 277–284 (2012).
72. Schneider, C., Porras, D. & Schaetz, T. *Experimental quantum simulations of many-body physics with trapped ions*. Rep. Prog. Phys. **75,** 024401 (2012).
73. Jurcevic, P. *et al. Quasiparticle engineering and entanglement propagation in a quantum many-body system*. *Nature* **511,** 202–205 (2014).
74. Richerme, P. *et al. Non-local propagation of correlations in quantum systems with long-range interactions*. *Nature* **511,** 198–201 (2014).
75. Gorshkov, A. V. *et al. Two-orbital SU(N) magnetism with ultracold alkaline-earth atoms*. Nat Phys **6,** 289–295 (2010).
76. Cazalilla, M. A. & Rey, A. M. *Ultracold Fermi gases with emergent SU(N) symmetry*. Rep. Prog. Phys. **77,** 124401 (2014).
77. Scazza, F. *et al. Observation of two-orbital spin-exchange interactions with ultracold SU(N)-symmetric fermions*. Nat Phys **10,** 779–784 (2014).
78. Zhang, X. *et al. Spectroscopic observation of SU(N)-symmetric interactions in Sr orbital magnetism*. *Science* **345,** 1467–1473 (2014).

79. Childs, A. M. *et al. Exponential algorithmic speedup by quantum walk*, 59 (2003).
80. Karski, M. *et al. Quantum Walk in Position Space with Single Optically Trapped Atoms*. *Science* **325,** 174–177 (2009).
81. Lieb, E., Schultz, T. & Mattis, D. *Two soluble models of an antiferromagnetic chain*. Ann. Phys. **16,** 407–466 (1961).
82. Lee, P. A., Nagaosa, N. & Wen, X.-G. *Doping a Mott insulator: Physics of high-temperature superconductivity*. Rev. Mod. Phys. **78,** 17–85 (2006).
83. Essler, F. H. L. & Korepin, V. E. *Higher conservation laws and algebraic Bethe Ansätze for the supersymmetric t - J model*. Phys. Rev. B **46,** 9147–9162 (1992).
84. Foerster, A. & Karowski, M. *The supersymmetric t-J model with quantum group invariance*. Nuclear Physics B **408,** 512–534 (1993).
85. Cazalilla, M. A., Citro, R., Giamarchi, T., Orignac, E. & Rigol, M. *One dimensional bosons: From condensed matter systems to ultracold gases*. Rev. Mod. Phys. **83,** 1405–1466 (2011).
86. Lieb, E. H. & Liniger, W. *Exact Analysis of an Interacting Bose Gas. I. The General Solution and the Ground State*. Phys. Rev. **130,** 1605–1616 (1963).
87. Caux, J.-S. & Calabrese, P. *Dynamical density-density correlations in the one-dimensional Bose gas*. Phys. Rev. A **74,** 031605 (2006).
88. Fabbri, N. *et al. Dynamical structure factor of one-dimensional Bose gases: Experimental signatures of beyond-Luttinger-liquid physics*. Phys. Rev. A **91,** 043617 (2015).
89. Girardeau, M. *Relationship between Systems of Impenetrable Bosons and Fermions in One Dimension*. J. Math. Phys. **1,** 516–523 (1960).
90. Paredes, B. *et al. Tonks–Girardeau gas of ultracold atoms in an optical lattice*. *Nature* **429,** 277–281 (2004).
91. Yan, B. *et al. Observation of dipolar spin-exchange interactions with lattice-confined polar molecules*. *Nature* **501,** 521–525 (2013).
92. Ni, K.-K. *et al. A High Phase-Space-Density Gas of Polar Molecules*. *Science* **322,** 231–235 (2008).
93. Baranov, M. A. *Theoretical progress in many-body physics with ultracold dipolar gases*. Physics Reports **464,** 71–111 (2008).
94. Kadau, H. *et al. Observing the Rosensweig instability of a quantum ferrofluid*. *Nature* **530,** 194–197 (2016).
95. Baier, S. *et al. Extended Bose-Hubbard models with ultracold magnetic atoms*. *Science* **352,** 201–205 (2016).

96. Zeiher, J. *et al. Many-Body Interferometry of a Rydberg-Dressed Spin Lattice*. Nat Phys **advance online publication.**
97. Schauß, P. *et al. Observation of spatially ordered structures in a two-dimensional Rydberg gas*. *Nature* **491,** 87–91 (2012).
98. Schauß, P. *et al. Crystallization in Ising quantum magnets*. *Science* **347,** 1455–1458 (2015).
99. Zeiher, J. *et al. Microscopic Characterization of Scalable Coherent Rydberg Superatoms*. Phys. Rev. X **5,** 031015 (2015).
100. Weitenberg, C. *Single-Atom Resolved Imaging and Manipulation in an Atomic Mott Insulator* PhD Thesis (Ludwig-Maximilians-Universität München, 2011).
101. Endres, M. *Probing correlated quantum many-body systems at the single-particle level* PhD Thesis (Ludwig-Maximilians-Universität München, 2013).
102. Schauss, P. *High-resolution imaging of ordering in Rydberg many-body systems* PhD Thesis (Ludwig-Maximilians-Universität München, 2015).
103. Clément, J.-F. *et al. All-optical runaway evaporation to Bose-Einstein condensation*. Phys. Rev. A **79,** 061406 (2009).
104. Barrett, M. D., Sauer, J. A. & Chapman, M. S. *All-Optical Formation of an Atomic Bose-Einstein Condensate*. Phys. Rev. Lett. **87,** 010404 (2001).
105. Stellmer, S., Pasquiou, B., Grimm, R. & Schreck, F. *Laser Cooling to Quantum Degeneracy*. Phys. Rev. Lett. **110,** 263003 (2013).
106. Caneva, T., Calarco, T. & Montangero, S. *Chopped random-basis quantum optimization*. Phys. Rev. A **84,** 022326 (2011).
107. Doria, P., Calarco, T. & Montangero, S. *Optimal Control Technique for Many-Body Quantum Dynamics*. Phys. Rev. Lett. **106,** 190501 (2011).
108. Grimm, R., Weidemüller, M. & Ovchinnikov, Y. B. in *Advances In Atomic, Molecular, and Optical Physics* (ed Walther, B. B. H.) 95–170 (Academic Press, 2000).
109. Jürgensen, O., Meinert, F., Mark, M. J., Nägerl, H.-C. & Lühmann, D.-S. *Observation of Density-Induced Tunneling*. Phys. Rev. Lett. **113,** 193003 (2014).
110. Marte, A. *et al. Feshbach Resonances in Rubidium 87: Precision Measurement and Analysis*. Phys. Rev. Lett. **89,** 283202 (2002).
111. Widera, A. *et al. Entanglement Interferometry for Precision Measurement of Atomic Scattering Properties*. Phys. Rev. Lett. **92,** 160406 (2004).

112. Erhard, M., Schmaljohann, H., Kronjäger, J., Bongs, K. & Sengstock, K. *Measurement of a mixed-spin-channel Feshbach resonance in* ^{87}Rb. Phys. Rev. A **69,** 032705 (2004).

113. Egorov, M. *et al. Measurement of s-wave scattering lengths in a two-component Bose-Einstein condensate*. Phys. Rev. A **87,** 053614 (2013).

114. Pertot, D., Gadway, B. & Schneble, D. *Collinear Four-Wave Mixing of Two-Component Matter Waves*. Phys. Rev. Lett. **104,** 200402 (2010).

115. Morsch, O. & Oberthaler, M. *Dynamics of Bose-Einstein condensates in optical lattices*. Rev. Mod. Phys. **78,** 179–215 (2006).

116. Gould, P. L., Ruff, G. A. & Pritchard, D. E. *Diffraction of atoms by light: The near-resonant Kapitza-Dirac effect*. Phys. Rev. Lett. **56,** 827–830 (1986).

117. Cahn, S. B. *et al. Time-Domain de Broglie Wave Interferometry*. Phys. Rev. Lett. **79,** 784–787 (1997).

118. Ovchinnikov, Y. B. *et al. Diffraction of a Released Bose-Einstein Condensate by a Pulsed Standing Light Wave*. Phys. Rev. Lett. **83,** 284–287 (1999).

119. Cristiani, M., Morsch, O., Müller, J. H., Ciampini, D. & Arimondo, E. *Experimental properties of Bose-Einstein condensates in one-dimensional optical lattices: Bloch oscillations, Landau-Zener tunneling, and mean-field effects*. Phys. Rev. A **65,** 063612 (2002).

120. Friebel, S., D'Andrea, C., Walz, J., Weitz, M. & Hänsch, T. W. CO_2*-laser optical lattice with cold rubidium atoms*. Phys. Rev. A **57,** R20–R23 (1998).

121. Ashcroft, N. W. & Mermin, N. D. *Solid state physics* (Holt, Rinehart and Winston, New York, 1976).

122. Ben Dahan, M., Peik, E., Reichel, J., Castin, Y. & Salomon, C. *Bloch Oscillations of Atoms in an Optical Potential*. Phys. Rev. Lett. **76,** 4508–4511 (1996).

123. Niu, Q., Zhao, X.-G., Georgakis, G. A. & Raizen, M. G. *Atomic Landau-Zener Tunneling and Wannier-Stark Ladders in Optical Potentials*. Phys. Rev. Lett. **76,** 4504–4507 (1996).

124. Anderson, B. P. & Kasevich, M. A. *Macroscopic Quantum Interference from Atomic Tunnel Arrays*. *Science* **282,** 1686–1689 (1998).

125. Islam, R. *et al. Measuring entanglement entropy in a quantum many-body system*. *Nature* **528,** 77–83 (2015).

126. DePue, M. T., McCormick, C., Winoto, S. L., Oliver, S. & Weiss, D. S. *Unity Occupation of Sites in a 3D Optical Lattice*. Phys. Rev. Lett. **82,** 2262–2265 (1999).

127. Endres, M. *et al. The 'Higgs' amplitude mode at the two-dimensional superfluid/Mott insulator transition*. *Nature* **487,** 454–458 (2012).

128. Gerlach, W. & Stern, O. *Der experimentelle Nachweis der Richtungsquantelung im Magnetfeld*. Z. Physik **9,** 349–352 (1922).

129. Gerlach, W. & Stern, O. *Der experimentelle Nachweis des magnetischen Moments des Silberatoms*. Z. Physik **8,** 110–111 (1922).

130. Gerlach, W. & Stern, O. *Das magnetische Moment des Silberatoms*. Z. Physik **9,** 353–355 (1922).

131. Heisenberg, W. *Über den anschaulichen Inhalt der quantentheoretischen Kinematik und Mechanik*. Z. Physik **43,** 172–198 (1927).

132. Amico, L., Fazio, R., Osterloh, A. & Vedral, V. *Entanglement in many-body systems*. Rev. Mod. Phys. **80,** 517–576 (2008).

133. Eisert, J., Cramer, M. & Plenio, M. B. *Colloquium : Area laws for the entanglement entropy*. Rev. Mod. Phys. **82,** 277–306 (2010).

134. Osterloh, A., Amico, L., Falci, G. & Fazio, R. *Scaling of entanglement close to a quantum phase transition*. *Nature* **416,** 608–610 (2002).

135. Calabrese, P., Cardy, J. & Doyon, B. *Entanglement entropy in extended quantum systems*. J. Phys. A: Math. Theor. **42,** 500301 (2009).

136. Bennett, C. H. & DiVincenzo, D. P. *Quantum information and computation*. *Nature* **404,** 247–255 (2000).

137. Roos, C. F. *et al. Bell States of Atoms with Ultralong Lifetimes and Their Tomographic State Analysis*. Phys. Rev. Lett. **92,** 220402 (2004).

138. Häffner, H., Roos, C. F. & Blatt, R. *Quantum computing with trapped ions*. Physics Reports **469,** 155–203 (2008).

139. Gühne, O. & Tóth, G. *Entanglement detection*. Physics Reports **474,** 1–75 (2009).

140. Brukner, Č., Vedral, V. & Zeilinger, A. *Crucial role of quantum entanglement in bulk properties of solids*. Phys. Rev. A **73,** 012110 (2006).

141. Estève, J., Gross, C., Weller, A., Giovanazzi, S. & Oberthaler, M. K. *Squeezing and entanglement in a Bose–Einstein condensate*. *Nature* **455,** 1216–1219 (2008).

142. Schleier-Smith, M. H., Leroux, I. D. & Vuletić, V. *States of an Ensemble of Two-Level Atoms with Reduced Quantum Uncertainty*. Phys. Rev. Lett. **104,** 073604 (2010).

143. Gross, C., Zibold, T., Nicklas, E., Estève, J. & Oberthaler, M. K. *Nonlinear atom interferometer surpasses classical precision limit*. *Nature* **464,** 1165–1169 (2010).

144. Riedel, M. F. *et al. Atom-chip-based generation of entanglement for quantum metrology*. *Nature* **464,** 1170–1173 (2010).

145. Gross, C. *et al. Atomic homodyne detection of continuous-variable entangled twin-atom states*. *Nature* **480,** 219–223 (2011).

146. Haas, F., Volz, J., Gehr, R., Reichel, J. & Estève, J. *Entangled States of More Than 40 Atoms in an Optical Fiber Cavity*. *Science* **344,** 180–183 (2014).

147. Lanting, T. *et al. Entanglement in a Quantum Annealing Processor*. Phys. Rev. X **4,** 021041 (2014).

148. Hensen, B. *et al. Loophole-free Bell inequality violation using electron spins separated by 1.3 kilometres*. *Nature* **526,** 682–686 (2015).

149. Lettner, M. *et al. Remote Entanglement between a Single Atom and a Bose-Einstein Condensate*. Phys. Rev. Lett. **106,** 210503 (2011).

150. Reiserer, A. & Rempe, G. *Cavity-based quantum networks with single atoms and optical photons*. Rev. Mod. Phys. **87,** 1379–1418 (2015).

151. Häffner, H. *et al. Scalable multiparticle entanglement of trapped ions*. *Nature* **438,** 643–646 (2005).

152. Cianciaruso, M., Bromley, T. R. & Adesso, G. *Accessible quantification of multiparticle entanglement*. arXiv: 1507.01600 (2015).

153. Mazza, L., Rossini, D., Fazio, R. & Endres, M. *Detecting two-site spin-entanglement in many-body systems with local particle-number fluctuations*. New J. Phys. **17,** 013015 (2015).

154. Harber, D. M., Lewandowski, H. J., McGuirk, J. M. & Cornell, E. A. *Effect of cold collisions on spin coherence and resonance shifts in a magnetically trapped ultracold gas*. Phys. Rev. A **66,** 053616 (2002).

155. Fukuhara, T. *et al. Quantum dynamics of a mobile spin impurity*. Nat Phys **9,** 235–241 (2013).

156. Fukuhara, T. *et al. Microscopic observation of magnon bound states and their dynamics*. *Nature* **502,** 76–79 (2013).

157. Fukuhara, T. *et al. Spatially Resolved Detection of a Spin-Entanglement Wave in a Bose-Hubbard Chain*. Phys. Rev. Lett. **115,** 035302 (2015).

158. Bellem, D. *Generation of Spatially and Temporally Varying Light Potentials in Optical Lattices* Diplomarbeit (Ludwig-Maximilians-Universität München, 2011).

159. Melville, H. *et al. Optical trapping of three-dimensional structures using dynamic holograms*. Opt. Express **11,** 3562 (2003).

160. Bergamini, S. *et al. Holographic generation of microtrap arrays for single atoms by use of a programmable phase modulator*. J. Opt. Soc. Am. B **21,** 1889 (2004).

161. Dorrer, C. & Zuegel, J. D. *Design and analysis of binary beam shapers using error diffusion*. J. Opt. Soc. Am. B **24,** 1268 (2007).

162. Gauthier, G. *et al. Configurable microscopic optical potentials for Bose-Einstein condensates using a digital-micromirror device*. arXiv: 1605.04928 (2016).

163. Zupancic, P. *et al. Ultra-precise holographic beam shaping for microscopic quantum control*. Opt. Express **24,** 13881 (2016).

164. Ha, L.-C., Clark, L. W., Parker, C. V., Anderson, B. M. & Chin, C. *Roton-Maxon Excitation Spectrum of Bose Condensates in a Shaken Optical Lattice*. Phys. Rev. Lett. **114,** 055301 (2015).

165. Vidal, G. *Efficient Simulation of One-Dimensional Quantum Many-Body Systems*. Phys. Rev. Lett. **93,** 040502 (2004).

166. Daley, A. J., Kollath, C., Schollwöck, U. & Vidal, G. *Time-dependent density-matrix renormalization-group using adaptive effective Hilbert spaces*. J. Stat. Mech. **2004,** P04005 (2004).

167. White, S. R. & Feiguin, A. E. *Real-Time Evolution Using the Density Matrix Renormalization Group*. Phys. Rev. Lett. **93,** 076401 (2004).

168. Verstraete, F., García-Ripoll, J. J. & Cirac, J. I. *Matrix Product Density Operators: Simulation of Finite-Temperature and Dissipative Systems*. Phys. Rev. Lett. **93,** 207204 (2004).

169. Schollwöck, U. *The density-matrix renormalization group*. Rev. Mod. Phys. **77,** 259–315 (2005).

170. Cramer, M., Plenio, M. B. & Wunderlich, H. *Measuring Entanglement in Condensed Matter Systems*. Phys. Rev. Lett. **106,** 020401 (2011).

171. Cramer, M. *et al. Spatial entanglement of bosons in optical lattices*. Nat Commun **4,** 2161 (2013).

172. Daley, A. J., Pichler, H., Schachenmayer, J. & Zoller, P. *Measuring Entanglement Growth in Quench Dynamics of Bosons in an Optical Lattice*. Phys. Rev. Lett. **109,** 020505 (2012).

173. Abanin, D. A. & Demler, E. *Measuring Entanglement Entropy of a Generic Many-Body System with a Quantum Switch*. Phys. Rev. Lett. **109,** 020504 (2012).

174. Wiseman, H. M. & Vaccaro, J. A. *Entanglement of Indistinguishable Particles Shared between Two Parties*. Phys. Rev. Lett. **91,** 097902 (2003).

175. Dowling, M. R., Doherty, A. C. & Wiseman, H. M. *Entanglement of indistinguishable particles in condensed-matter physics*. Phys. Rev. A **73,** 052323 (2006).

176. Trotzky, S., Chen, Y.-A., Schnorrberger, U., Cheinet, P. & Bloch, I. *Controlling and Detecting Spin Correlations of Ultracold Atoms in Optical Lattices*. Phys. Rev. Lett. **105,** 265303 (2010).

177. Nascimbène, S. *et al. Experimental Realization of Plaquette Resonating Valence-Bond States with Ultracold Atoms in Optical Superlattices*. Phys. Rev. Lett. **108,** 205301 (2012).

178. Greif, D., Uehlinger, T., Jotzu, G., Tarruell, L. & Esslinger, T. *Short-Range Quantum Magnetism of Ultracold Fermions in an Optical Lattice*. *Science* **340,** 1307–1310 (2013).

179. Jaksch, D., Briegel, H.-J., Cirac, J. I., Gardiner, C. W. & Zoller, P. *Entanglement of Atoms via Cold Controlled Collisions*. Phys. Rev. Lett. **82,** 1975–1978 (1999).

180. Mandel, O. *et al. Controlled collisions for multi-particle entanglement of optically trapped atoms*. *Nature* **425,** 937–940 (2003).

181. Anderlini, M. *et al. Controlled exchange interaction between pairs of neutral atoms in an optical lattice*. *Nature* **448,** 452–456 (2007).

182. Wootters, W. K. *Entanglement of Formation of an Arbitrary State of Two Qubits*. Phys. Rev. Lett. **80,** 2245–2248 (1998).

183. Mintert, F., Kuś, M. & Buchleitner, A. *Concurrence of Mixed Bipartite Quantum States in Arbitrary Dimensions*. Phys. Rev. Lett. **92,** 167902 (2004).

184. Schuch, N., Verstraete, F. & Cirac, J. I. *Quantum entanglement theory in the presence of superselection rules*. Phys. Rev. A **70,** 042310 (2004).

185. Wortis, M. *Bound States of Two Spin Waves in the Heisenberg Ferromagnet*. Phys. Rev. **132,** 85–97 (1963).

186. Takahashi, M. *One-Dimensional Heisenberg Model at Finite Temperature*. Prog. Theor. Phys. **46,** 401–415 (1971).

187. Hanus, J. *Bound States in the Heisenberg Ferromagnet*. Phys Rev Lett **11,** 336–338 (1963).

188. Fogedby, H. C. *The spectrum of the continuous isotropic quantum Heisenberg chain: quantum solitons as magnon bound states*. J Phys C Solid State Phys **13,** L195 (1980).

189. Schneider, T. *Solitons and magnon bound states in ferromagnetic Heisenberg chains*. Phys Rev B **24,** 5327–5339 (1981).

190. Schreiber, A. *et al. A 2D Quantum Walk Simulation of Two-Particle Dynamics*. *Science* **336,** 55–58 (2012).

191. Lahini, Y. *et al. Quantum walk of two interacting bosons*. Phys Rev A **86,** 011603(R) (2012).

192. Venegas-Andraca, S. E. *Quantum walks: a comprehensive review*. Quant Inf Proc **11,** 1015–1116 (2012).

193. Bose, S. *Quantum communication through spin chain dynamics: an introductory overview*. Contemp. Phys. **48,** 13–30 (2007).

194. Date, M. & Motokawa, M. *Spin-Cluster Resonance in* $Co Cl_2 \cdot 2H_2O$. Phys Rev Lett **16,** 1111–1114 (1966).

195. Torrance, J. B. & Tinkham, M. *Excitation of Multiple-Magnon Bound States in* $Co Cl_2 \cdot 2H_2O$. Phys. Rev. **187,** 595–606 (1969).

196. Hoogerbeets, R., van Duyneveldt, A. J., Phaff, A. C., Swuste, C. H. W. & de Jonge, W. J. M. *Evidence for magnon bound-state excitations in the quantum chain system (C 6 H 11 N 3)CuCl 3*. J. Phys. C: Solid State Phys. **17,** 2595 (1984).

197. Winkler, K. *et al. Repulsively bound atom pairs in an optical lattice*. *Nature* **441,** 853–856 (2006).

198. Fölling, S. *et al. Direct observation of second-order atom tunnelling*. *Nature* **448,** 1029–1032 (2007).

199. Karbach, M. & Muller, G. *Introduction to the Bethe ansatz I*. arXiv: `cond-mat/9809162` (1998).

200. Zvonarev, M. B., Cheianov, V. V. & Giamarchi, T. *Dynamical Properties of the One-Dimensional Spin-*1/2 *Bose-Hubbard Model near a Mott-Insulator to Ferromagnetic-Liquid Transition*. Phys. Rev. Lett. **103,** 110401 (2009).

201. Bose, S. *Quantum Communication through an Unmodulated Spin Chain*. Phys. Rev. Lett. **91,** 207901 (2003).

202. Subrahmanyam, V. *Entanglement dynamics and quantum-state transport in spin chains*. Phys. Rev. A **69,** 034304 (2004).

203. Zvonarev, M. B., Cheianov, V. V. & Giamarchi, T. *Spin Dynamics in a One-Dimensional Ferromagnetic Bose Gas*. Phys. Rev. Lett. **99,** 240404 (2007).

204. Ganahl, M., Rabel, E., Essler, F. H. L. & Evertz, H. G. *Observation of Complex Bound States in the Spin-*1/2 *Heisenberg XXZ Chain Using Local Quantum Quenches*. Phys. Rev. Lett. **108,** 077206 (2012).

205. Gobert, D., Kollath, C., Schollwöck, U. & Schütz, G. *Real-time dynamics in spin-*$\frac{1}{2}$ *chains with adaptive time-dependent density matrix renormalization group*. Phys. Rev. E **71,** 036102 (2005).

206. Giamarchi, T. *Quantum Physics in One Dimension* 440 pp. (Clarendon Press, 2003).

207. Nishida, Y., Kato, Y. & Batista, C. D. *Efimov effect in quantum magnets*. Nat Phys **9,** 93–97 (2013).

208. Bloembergen, N. *On the interaction of nuclear spins in a crystalline lattice*. **15,** 386–426 (1949).

209. Van Hove, L. *Time-Dependent Correlations between Spins and Neutron Scattering in Ferromagnetic Crystals*. Phys. Rev. **95,** 1374–1384 (1954).

210. De Gennes, P. G. *Inelastic magnetic scattering of neutrons at high temperatures*. Journal of Physics and Chemistry of Solids **4,** 223–226 (1958).

211. Hone, D., Scherer, C. & Borsa, F. *Proton spin-lattice relaxation in TMMC* $[(CH_3)_4\ NMnCl_3]$. Phys. Rev. B **9,** 965–974 (1974).

212. Boucher, J. P. *et al. High-temperature spin dynamics in the one-dimensional Heisenberg system* $(CH_3)_4NMnCl_3$ *(TMMC): Spin diffusion, intra- and interchain cutoff effects*. Phys. Rev. B **13,** 4098–4118 (1976).

213. Benner, H. *Experimental evidence for spin diffusion in the quasi-two-dimensional Heisenberg paramagnet* $(C_2H_5NH_3)_2MnCl_4$. Phys. Rev. B **18,** 319–325 (1978).

214. Takigawa, M., Motoyama, N., Eisaki, H. & Uchida, S. *Dynamics in the S=1/2 One-Dimensional Antiferromagnet Sr2CuO3 via 63Cu NMR*. Phys Rev Lett **76,** 4612–4615 (1996).

215. Thurber, K. R., Hunt, A. W., Imai, T. & Chou, F. C. ^{17}*O NMR Study of* $q = 0$ *Spin Excitations in a Nearly Ideal* $S = \frac{1}{2}$ *1D Heisenberg Antiferromagnet,* Sr_2CuO_3*, up to 800 K*. Phys Rev Lett **87,** 247202 (2001).

216. Chertkov, M. & Kolokolov, I. *Long-time dynamics of the infinite-temperature Heisenberg magnet*. Phys. Rev. B **49,** 3592–3595 (1994).

217. Lovesey, S. W., Engdahl, E., Cuccoli, A., Tognetti, V. & Balcar, E. *Time-dependent spin correlations in the Heisenberg magnet at infinite temperature*. J. Phys.: Condens. Matter **6,** L521 (1994).

218. Müller, G. *Anomalous Spin Diffusion in Classical Heisenberg Magnets*. Phys. Rev. Lett. **60,** 2785–2788 (1988).

219. De Alcantara Bonfim, O. F. & Reiter, G. *Breakdown of hydrodynamics in the classical 1D Heisenberg model*. Phys. Rev. Lett. **69,** 367–370 (1992).

220. Shastry, B. S. & Sutherland, B. *Twisted boundary conditions and effective mass in Heisenberg-Ising and Hubbard rings*. Phys. Rev. Lett. **65,** 243–246 (1990).

221. Castella, H., Zotos, X. & Prelovšek, P. *Integrability and Ideal Conductance at Finite Temperatures*. Phys. Rev. Lett. **74,** 972–975 (1995).

222. Zotos, X., Naef, F. & Prelovsek, P. *Transport and conservation laws*. Phys. Rev. B **55,** 11029–11032 (1997).

223. Zotos, X. *Finite Temperature Drude Weight of the One-Dimensional Spin-1/2 Heisenberg Model*. Phys. Rev. Lett. **82,** 1764–1767 (1999).

224. Narozhny, B. N., Millis, A. J. & Andrei, N. *Transport in the* XXZ *model*. Phys. Rev. B **58,** R2921–R2924 (1998).

225. Alvarez, J. V. & Gros, C. *Low-Temperature Transport in Heisenberg Chains*. Phys Rev Lett **88,** 077203 (2002).

226. Heidrich-Meisner, F., Honecker, A., Cabra, D. C. & Brenig, W. *Zero-frequency transport properties of one-dimensional spin-12 systems*. Phys Rev B **68,** 134436 (2003).

227. Sirker, J., Pereira, R. G. & Affleck, I. *Diffusion and Ballistic Transport in One-Dimensional Quantum Systems*. Phys. Rev. Lett. **103,** 216602 (2009).

228. Sirker, J., Pereira, R. G. & Affleck, I. *Conservation laws, integrability, and transport in one-dimensional quantum systems*. Phys. Rev. B **83,** 035115 (2011).

229. Prosen, T. *Open XXZ Spin Chain: Nonequilibrium Steady State and a Strict Bound on Ballistic Transport*. Phys. Rev. Lett. **106,** 217206 (2011).

230. Žnidarič, M. *Spin Transport in a One-Dimensional Anisotropic Heisenberg Model*. Phys. Rev. Lett. **106,** 220601 (2011).

231. Steinigeweg, R. & Brenig, W. *Spin Transport in the XXZ Chain at Finite Temperature and Momentum*. Phys. Rev. Lett. **107,** 250602 (2011).

232. Karrasch, C., Bardarson, J. H. & Moore, J. E. *Finite-Temperature Dynamical Density Matrix Renormalization Group and the Drude Weight of Spin-1/2 Chains*. Phys. Rev. Lett. **108,** 227206 (2012).

233. Žnidarič, M. *Anomalous Nonequilibrium Current Fluctuations in the Heisenberg Model*. Phys. Rev. B **90,** 115156 (2014).

234. Sommer, A., Ku, M., Roati, G. & Zwierlein, M. W. *Universal spin transport in a strongly interacting Fermi gas*. *Nature* **472,** 201–204 (2011).

235. Koschorreck, M., Pertot, D., Vogt, E. & Köhl, M. *Universal spin dynamics in two-dimensional Fermi gases*. Nat Phys **9,** 405–409 (2013).

236. Bardon, A. B. *et al. Transverse Demagnetization Dynamics of a Unitary Fermi Gas*. *Science* **344,** 722–724 (2014).

237. Cameron, A. R., Riblet, P. & Miller, A. *Spin Gratings and the Measurement of Electron Drift Mobility in Multiple Quantum Well Semiconductors*. Phys. Rev. Lett. **76,** 4793–4796 (1996).

238. Zhang, W. & Cory, D. G. *First Direct Measurement of the Spin Diffusion Rate in a Homogenous Solid*. Phys. Rev. Lett. **80,** 1324–1327 (1998).

239. Wang, G. *et al. Gate control of the electron spin-diffusion length in semiconductor quantum wells*. Nat Commun **4,** 2372 (2013).

240. Choi, J.-y., Kwon, W. J. & Shin, Y.-i. *Observation of Topologically Stable 2D Skyrmions in an Antiferromagnetic Spinor Bose-Einstein Condensate*. Phys. Rev. Lett. **108,** 035301 (2012).

241. Barmettler, P., Punk, M., Gritsev, V., Demler, E. & Altman, E. *Relaxation of Antiferromagnetic Order in Spin-1/2 Chains Following a Quantum Quench*. Phys. Rev. Lett. **102,** 130603 (2009).

242. Sommer, A., Ku, M. & Zwierlein, M. W. *Spin transport in polaronic and superfluid Fermi gases*. New J. Phys. **13,** 055009 (2011).

243. Basko, D. M., Aleiner, I. L. & Altshuler, B. L. *Metal–insulator transition in a weakly interacting many-electron system with localized single-particle states*. Annals of Physics **321,** 1126–1205 (2006).

244. Knap, M. *et al. Probing Real-Space and Time-Resolved Correlation Functions with Many-Body Ramsey Interferometry*. Phys. Rev. Lett. **111,** 147205 (2013).

245. Serbyn, M. *et al. Interferometric Probes of Many-Body Localization*. Phys. Rev. Lett. **113,** 147204 (2014).

246. Fischer, M. C., Gutiérrez-Medina, B. & Raizen, M. G. *Observation of the Quantum Zeno and Anti-Zeno Effects in an Unstable System*. Phys. Rev. Lett. **87,** 040402 (2001).

247. Maniscalco, S., Francica, F., Zaffino, R. L., Lo Gullo, N. & Plastina, F. *Protecting Entanglement via the Quantum Zeno Effect*. Phys. Rev. Lett. **100,** 090503 (2008).

248. Kardar, M. *Statistical physics of particles* (Cambridge University Press, 2007).

249. Rigol, M., Dunjko, V. & Olshanii, M. *Thermalization and its mechanism for generic isolated quantum systems*. *Nature* **452,** 854–858 (2008).

250. Rigol, M. *Breakdown of Thermalization in Finite One-Dimensional Systems*. Phys. Rev. Lett. **103,** 100403 (2009).

251. Pal, A. & Huse, D. A. *Many-body localization phase transition*. Phys. Rev. B **82,** 174411 (2010).

252. Clos, G., Porras, D., Warring, U. & Schaetz, T. *Time-resolved observation of thermalization in an isolated quantum system*. arXiv: 1509.07712 (2015).

253. Jaynes, E. T. *Information Theory and Statistical Mechanics. II*. Phys. Rev. **108,** 171–190 (1957).

254. Rigol, M., Dunjko, V., Yurovsky, V. & Olshanii, M. *Relaxation in a Completely Integrable Many-Body Quantum System: An Ab Initio Study of the Dynamics of the Highly Excited States of 1D Lattice Hard-Core Bosons*. Phys. Rev. Lett. **98,** 050405 (2007).

255. Caux, J.-S. & Konik, R. M. *Constructing the Generalized Gibbs Ensemble after a Quantum Quench*. Phys. Rev. Lett. **109,** 175301 (2012).

256. Langen, T. *et al. Experimental observation of a generalized Gibbs ensemble*. *Science* **348,** 207–211 (2015).

257. Vidmar, L. & Rigol, M. *Generalized Gibbs Ensemble in Integrable Lattice Models*. J. Stat. Mech. **2016,** 064007 (2016).

258. John, S. & Stephen, M. J. *Wave propagation and localization in a long-range correlated random potential*. Phys. Rev. B **28,** 6358–6368 (1983).

259. *Diffuse Waves in Complex Media* (ed Fouque, J.-P.) (Springer Netherlands, Dordrecht, 1999).

260. Aspect, A. & Inguscio, M. *Anderson localization of ultracold atoms*. Phys. Today **62,** 30–35 (2009).

261. Mott, N. F. *Electrons in disordered structures*. Adv. Phys. **16,** 49–144 (1967).

262. Lucioni, E. *et al. Observation of Subdiffusion in a Disordered Interacting System*. Phys. Rev. Lett. **106,** 230403 (2011).

263. Kondov, S. S., McGehee, W. R., Zirbel, J. J. & DeMarco, B. *Three-Dimensional Anderson Localization of Ultracold Matter*. *Science* **334,** 66–68 (2011).

264. Jendrzejewski, F. *et al. Three-dimensional localization of ultracold atoms in an optical disordered potential*. Nat Phys **8,** 398–403 (2012).

265. McGehee, W. R., Kondov, S. S., Xu, W., Zirbel, J. J. & DeMarco, B. *Three-Dimensional Anderson Localization in Variable Scale Disorder*. Phys. Rev. Lett. **111,** 145303 (2013).

266. Chabanov, A. A., Stoytchev, M. & Genack, A. Z. *Statistical signatures of photon localization*. *Nature* **404,** 850–853 (2000).

267. Hu, H., Strybulevych, A., Page, J. H., Skipetrov, S. E. & van Tiggelen, B. A. *Localization of ultrasound in a three-dimensional elastic network*. Nat Phys **4,** 945–948 (2008).

268. Lahini, Y. *et al. Anderson Localization and Nonlinearity in One-Dimensional Disordered Photonic Lattices*. Phys. Rev. Lett. **100,** 013906 (2008).

269. Schwartz, T., Bartal, G., Fishman, S. & Segev, M. *Transport and Anderson localization in disordered two-dimensional photonic lattices*. *Nature* **446,** 52–55 (2007).

270. Wiersma, D. S., Bartolini, P., Lagendijk, A. & Righini, R. *Localization of light in a disordered medium*. *Nature* **390,** 671–673 (1997).

271. Störzer, M., Gross, P., Aegerter, C. M. & Maret, G. *Observation of the Critical Regime Near Anderson Localization of Light*. Phys. Rev. Lett. **96,** 063904 (2006).

272. Fleishman, L. & Anderson, P. W. *Interactions and the Anderson transition*. Phys. Rev. B **21,** 2366–2377 (1980).

273. Altshuler, B. L., Aronov, A. G. & Khmelnitsky, D. E. *Effects of electron-electron collisions with small energy transfers on quantum localisation*. J. Phys. C: Solid State Phys. **15,** 7367 (1982).

274. Ting, C. S., Houghton, A. & Senna, J. R. *Thermoelectric power in a disordered two-dimensional electron system*. Phys. Rev. B **25,** 1439–1442 (1982).

275. Gornyi, I. V., Mirlin, A. D. & Polyakov, D. G. *Interacting Electrons in Disordered Wires: Anderson Localization and Low-T Transport*. *Phys. Rev. Lett.* **95,** 206603 (20 2005).

276. Aleiner, I. L., Altshuler, B. L. & Shlyapnikov, G. V. *A finite-temperature phase transition for disordered weakly interacting bosons in one dimension*. Nat Phys **6,** 900–904 (2010).

277. Oganesyan, V. & Huse, D. A. *Localization of interacting fermions at high temperature*. Phys. Rev. B **75,** 155111 (2007).

278. Altman, E. *Non equilibrium quantum dynamics in ultra-cold quantum gases*. arXiv: 1512.00870 (2015).

279. Altman, E. & Vosk, R. *Universal Dynamics and Renormalization in Many-Body-Localized Systems*. Annu. Rev. Condens. Matter Phys. **6,** 383–409 (2015).

280. Serbyn, M., Papić, Z. & Abanin, D. A. *Local Conservation Laws and the Structure of the Many-Body Localized States*. Phys. Rev. Lett. **111,** 127201 (2013).

281. Huse, D. A., Nandkishore, R. & Oganesyan, V. *Phenomenology of fully many-body-localized systems*. Phys. Rev. B **90,** 174202 (2014).

282. Žnidarič, M., Prosen, T. & Prelovšek, P. *Many-body localization in the Heisenberg XXZ magnet in a random field*. Phys. Rev. B **77,** 064426 (2008).

283. Bardarson, J. H., Pollmann, F. & Moore, J. E. *Unbounded Growth of Entanglement in Models of Many-Body Localization*. Phys. Rev. Lett. **109,** 017202 (2012).

284. Vosk, R. & Altman, E. *Many-Body Localization in One Dimension as a Dynamical Renormalization Group Fixed Point*. Phys. Rev. Lett. **110,** 067204 (2013).

285. Serbyn, M., Papić, Z. & Abanin, D. A. *Universal Slow Growth of Entanglement in Interacting Strongly Disordered Systems*. Phys. Rev. Lett. **110,** 260601 (2013).

286. Nanduri, A., Kim, H. & Huse, D. A. *Entanglement spreading in a many-body localized system*. Phys. Rev. B **90,** 064201 (2014).

287. Serbyn, M. & Moore, J. E. *Spectral statistics across the many-body localization transition*. Phys. Rev. B **93,** 041424 (2016).

288. Potter, A. C., Vasseur, R. & Parameswaran, S. A. *Universal Properties of Many-Body Delocalization Transitions*. Phys. Rev. X **5,** 031033 (2015).

289. Vosk, R., Huse, D. A. & Altman, E. *Theory of the Many-Body Localization Transition in One-Dimensional Systems*. Phys. Rev. X **5,** 031032 (2015).

290. Damski, B., Zakrzewski, J., Santos, L., Zoller, P. & Lewenstein, M. *Atomic Bose and Anderson Glasses in Optical Lattices*. Phys. Rev. Lett. **91,** 080403 (2003).

291. Söyler, Ş. G., Kiselev, M., Prokof'ev, N. V. & Svistunov, B. V. *Phase Diagram of the Commensurate Two-Dimensional Disordered Bose-Hubbard Model*. Phys. Rev. Lett. **107,** 185301 (2011).

292. Bauer, B. & Nayak, C. *Area laws in a many-body localized state and its implications for topological order*. J. Stat. Mech. **2013,** P09005 (2013).

293. Kjäll, J. A., Bardarson, J. H. & Pollmann, F. *Many-Body Localization in a Disordered Quantum Ising Chain*. Phys. Rev. Lett. **113,** 107204 (2014).

294. Luitz, D. J., Laflorencie, N. & Alet, F. *Many-body localization edge in the random-field Heisenberg chain*. Phys. Rev. B **91,** 081103 (2015).

295. Michal, V. P., Altshuler, B. L. & G. V. Shlyapnikov. *Delocalization of Weakly Interacting Bosons in a 1D Quasiperiodic Potential*. Phys. Rev. Lett. **113,** 045304 (2014).

296. Johri, S., Nandkishore, R. & Bhatt, R. N. *Many-Body Localization in Imperfectly Isolated Quantum Systems*. Phys. Rev. Lett. **114,** 117401 (2015).

297. Smith, J. *et al. Many-Body Localization in a Quantum Simulator with Programmable Random Disorder*. Nat Phys **12,** 907–911 (2016).

298. Kondov, S. S., McGehee, W. R., Xu, W. & DeMarco, B. *Disorder-Induced Localization in a Strongly Correlated Atomic Hubbard Gas*. Phys. Rev. Lett. **114,** 083002 (2015).

299. Hauschild, J., Heidrich-Meisner, F. & Pollmann, F. *Domain-Wall Melting as a Probe of Many-Body Localization*. Phys. Rev. B **94,** 161109 (2016).

300. Pezzé, L. *et al. Regimes of classical transport of cold gases in a two-dimensional anisotropic disorder*. New J. Phys. **13,** 095015 (2011).

301. Nandkishore, R., Gopalakrishnan, S. & Huse, D. A. *Spectral features of a many-body-localized system weakly coupled to a bath*. Phys. Rev. B **90,** 064203 (2014).

302. Fischer, M. H., Maksymenko, M. & Altman, E. *Dynamics of a Many-Body-Localized System Coupled to a Bath*. Phys. Rev. Lett. **116,** 160401 (2016).

303. Levi, E., Heyl, M., Lesanovsky, I. & Garrahan, J. P. *Robustness of Many-Body Localization in the Presence of Dissipation*. Phys. Rev. Lett. **116,** 237203 (2016).

304. Bar Lev, Y., Cohen, G. & Reichman, D. R. *Absence of Diffusion in an Interacting System of Spinless Fermions on a One-Dimensional Disordered Lattice*. Phys. Rev. Lett. **114,** 100601 (2015).

305. Agarwal, K., Gopalakrishnan, S., Knap, M., Müller, M. & Demler, E. *Anomalous Diffusion and Griffiths Effects Near the Many-Body Localization Transition*. Phys. Rev. Lett. **114,** 160401 (2015).

306. Lev, Y. B. & Reichman, D. R. *Slow dynamics in a two-dimensional Anderson-Hubbard model*. *EPL (Europhysics Letters)* **113,** 46001 (2016).

307. Kirkpatrick, S. *Percolation and Conduction*. Rev. Mod. Phys. **45,** 574–588 (1973).

308. Chandran, A., Kim, I. H., Vidal, G. & Abanin, D. A. *Constructing local integrals of motion in the many-body localized phase*. Phys. Rev. B **91,** 085425 (2015).

309. Goihl, M., Friesdorf, M., Werner, A. H., Brown, W. & Eisert, J. *Experimentally accessible witnesses of many-body localisation*. arXiv: 1601.02666 (2016).

310. Lester, B. J., Kaufman, A. M. & Regal, C. A. *Raman cooling imaging: Detecting single atoms near their ground state of motion*. Phys. Rev. A **90,** 011804 (2014).

311. Patil, Y. S., Chakram, S., Aycock, L. M. & Vengalattore, M. *Nondestructive imaging of an ultracold lattice gas*. Phys. Rev. A **90,** 033422 (2014).

List of Figures

Danksagung

Zum Gelingen meiner Promotion haben viele Personen beigetragen, bei denen ich mich hiermit recht herzlich bedanken möchte. Ich habe etwas mehr als vier ereignisreiche Jahre am Max-Planck-Institut für Quantenoptik verbracht. In dieser Zeit habe ich sehr viel von meinem Umfeld gelernt.

Ein besonderer Dank gilt meinem betreuenden Professor Immanuel Bloch für die großartige Unterstützung in jeglicher Hinsicht. Mir wurden hervorragende Bedingungen für die Realisierung der komplizierten Experimente geschaffen. Durch zahlreiche Besprechungen wurden mir die Details der Physik näher gebracht.

Vor allem möchte ich mich bei meinem Betreuer, Christian Groß, für die Unterstützung und Koordination der Forschung bedanken, während der mir sehr viele Freiheiten gewährt wurden. In einer sehr angenehmen offenen Atmosphäre hat er immer alles versucht, um die experimentellen und physikalischen Herausforderungen mit meinem Team zu lösen.

Durch die Zusammenarbeit mit Marc Cheneau habe ich sehr viel über das Experiment und die damit verbundene Physik gelernt. Diese Unterstützung war besonders in der Anfangszeit ausgesprochen hilfreich.

Bei der Durchführung meiner Experimente waren besonders Takeshi Fukuhara und Jae-yoon Choi involviert. Ich bedanke mich für die sehr erfolgreiche Zusammenarbeit, während der ich mit viel Spaß und Freude neue Erkenntnisse über ultrakalte Quantengase gewonnen habe.

Manuel Endres und Christoph Weitenberg haben mit ihren Promotionsarbeiten die Grundlage für meine Experimente geschaffen. Vielen Dank für den wartungsarmen Experimentaufbau, die vielen guten Diskussionen und hilfreichen Tipps.

Für das eigentliche Experiment selber möchte ich mich bei Peter Schauß und Johannes Zeiher bedanken. Zusammen haben wir jede mögliche Störung am Experiment schnell behoben und exzellente Resultate erzielt.

Bei Tarik Yefsah und Antonio Rubio Abadal bedanke ich mich für die vielfältigen Diskussionen und die Entwicklung von neuen Ideen für weitere Experimente und die gute Zusammenarbeit im letzten Jahr meiner Promotion.

Bei den vielen Mitgliedern der Arbeitsgruppe möchte ich mich für die Hilfe in den verschiedensten Bereichen der Physik als auch für deren Expertise zur Realisierung der Experimente bedanken. Sowohl die interessanten Journal Club Treffen als auch die vielen weiteren Gespräche über Physik, Elektronik und Realisierung von komplexen Messungen haben mich weiter gebracht.

Ein so komplexes Experiment umsetzen und zu erweitern ist nicht möglich ohne die technische Unterstützung. Es war ausgesprochen hilfreich stets auf die volle Unterstützung von Karsten Förster, Oliver Mödl, Bodo Hecker und Anton Mayer zu haben. Zusätzlich bedanke ich mich bei den Mitarbeitern der institutseigenen Werkstatt, die uns immer wieder exzellente Aufbauten in kürzester Zeit geliefert haben. Auf der administrativen Seite bedanke ich mich für die gute Unterstützung bei Marianne Kargl, Ildiko Kecskesi und Kristina Schuldt.

Darüber hinaus habe ich in vielen Arbeitskollegen auch gute Freunde gefunden. So wurden viele Wochenenden in den Bergen verbracht, an denen es neben der Diskussion über die Physik in den unterschiedlichen Laboren auch viele andere spannende Themen gab. Ich habe mit viel Freude an den Fußballspielen, Fahrradtouren und gemeinsamen Kochveranstaltungen teilgenommen.

Abschließend möchte ich mich bei meiner Familie für die fortwährende Unterstützung und den Rückhalt bedanken.

Ich hatte eine wunderbare Zeit in einer Gruppe von sehr motivierten Personen, in der ich viele besondere Erfahrungen gemacht und viel gelernt habe.